Superconducting flip-chip microwave resonators on materials with high dielectric constant

Bachelor Thesis verfasst von
Cenk Beydeda

1. Physikalisches Institut
Universität Stuttgart

Hauptberichter **Prof. Dr. Martin Dressel**

Betreuer **Dr. Marc Scheffler**
M.Sc. Nikolaj Ebensperger

30. September 2020

Contents

1 Motivation

Coplanar waveguides were first proposed by Wen [1] in order to simplify microwave circuits. One of the great advantages of the coplanar waveguide is their easy manufacturing process as the conducting elements are deposited on one side of a dielectric substrate. Wen proposed the coplanar waveguide because he intended to design nonreciprocal gyromagnetic microwave devices.

Coplanar waveguides are also the favoured waveguide structure when it comes to the design of quantum processing devices. The field strength of the transmitted microwave can be increased by altering the dimensions of the coplanar waveguide with only slight disturbances of the impedance of the waveguide [2]. Coplanar microwave resonators with high quality factors that exceed $Q > 10^6$ could be fabricated [3] and quality factors with $Q > 10^5$ can be routinely fabricated [4]. Also single photon detectors were designed which allow further investigations on quantum processing devices [3][5]. The research area that focuses on the design of these superconducting microwave circuits for quantum computing is called circuit quantum electrodynamics [2].

Superconducting microwave resonators would not only allow to investigate the superconducting behaviour of interesting materials [6][7][8] but they could also be used to measure the dielectric constant ϵ of insulating solid dielectrics. This is especially appealing because superconducting coplanar resonators were already optimized to high quality factors and therefore precise measurements would be possible. In fact many measurement techniques were already developed. A coplanar resonator capacitively coupled to the feedline and deposited on a dielectric allows to measure it's dielectric constant ϵ [6]. More complex configurations where a disordered dielectric of interest is deposited as a thin film on a inductively coupled resonator [9] or where distant flip-chip resonators on dielectrics are coupled inductively to the feedline [10][11] were also demonstrated.

Especially the distant flip-chip resonator is appealing as it allows to measure extraordinary high dielectric constants ϵ of solid insulators. Dielectrics that could be successfully probed this way were $LaAlO_2$, MgO, TiO_2 and $SrTiO_3$ [10][11]. However open questions remain concerning the mode identification.

When investigating multi-mode superconducting flip-chip resonators it could be seen that the resonances are not exactly n multiples of the fundamental mode but slightly differ. Already heating to room temperature and cooling to cryogenic temperatures can result in slightly different resonance frequencies [12]. This is not necessarily a problem as these effects can be explained when considering the strong dependence of the resonance frequency on the distance between the flip-chip and the feedline. However it becomes a problem when the fundamental mode is suppressed and parasitic modes are present. Parasitic modes are a common feature when working with superconducting microwave resonators, but when using superconducting microwave devices for spectroscopy, the parasitic modes were also affected by the dielectric

of interest which makes it further difficult to separate them.
This thesis aims at developing additional measurement techniques that would allow in the best case to clearly separate parasitic modes and resonator modes. Therefore a superconducting resonator on the already well-known substrate TiO_2 is investigated again with regard to the numerous harmonics and parasitic modes. The dependence of the resonance frequency f and the quality factor Q of all modes is observed and evaluated in order to develop techniques that can be routinely applied to distinguish resonator modes and parasitic modes.

2 Theoretical principles

2.1 Maxwell's equations

Maxwell's equations were first given by James Clerk Maxwell [13] and later rewritten by Oliver Heaviside into their today known form. In the presence of matter Maxwell's equation are given by [14]

$$\begin{aligned}
\nabla \cdot \mathbf{D}(\mathbf{r}, t) &= 4\pi\rho(\mathbf{r}, t) \\
\nabla \cdot \mathbf{B}(\mathbf{r}, t) &= 0 \\
\nabla \times \mathbf{E}(\mathbf{r}, t) &= -\frac{1}{c}\partial_t \mathbf{B}(\mathbf{r}, t) \\
\nabla \times \mathbf{H}(\mathbf{r}, t) &= \frac{4\pi}{c}\mathbf{J}(\mathbf{r}, t) + \frac{1}{c}\partial_t \mathbf{D}(\mathbf{r}, t)
\end{aligned} \tag{2.1}$$

where $\mathbf{D} = \epsilon\mathbf{E}$ is the electric displacement field, $\mathbf{B} = \mu\mathbf{H}$ is the magnetic flux density, $\mathbf{H}$ is the magnetic field and $\mathbf{E}$ is the electric field with the dielectric constant ϵ and the magnetic permeability $\mu = \mu_0 = 1.2566 \cdot 10^{-6}\,\frac{\mathrm{Vs}}{\mathrm{Am}}$ which can be set to the magnetic permeability of vacuum if non-magnetic materials are investigated. ρ is the charge density, $\mathbf{J}$ is the current density and $c = 299\,792\,458\,\frac{\mathrm{m}}{\mathrm{s}}$ is the speed of light.
Under the assumption of Ohm's law $\mathbf{J} = \sigma\mathbf{E}$ where σ is the conductivity and a harmonic time dependence $\partial_t \mathbf{D} = -i\omega\mathbf{D}$ with the frequency ω the fourth of Maxwell's equations (2.1) can be rewritten [14]

$$\nabla \times \mathbf{H} = \frac{1}{c}\left(4\pi\sigma - i\omega\epsilon\right)\mathbf{E} = -\frac{i\omega}{c}\hat{\epsilon}\mathbf{E} \tag{2.2}$$

where a complex dielectric constant is introduced

$$\hat{\epsilon} = \epsilon_1 + \epsilon_2 = \epsilon + i\frac{4\pi\sigma}{\omega}. \tag{2.3}$$

The real part of the complex dielectric constant $\Re(\hat{\epsilon}) = \epsilon$ describes the lossless dispersion and the imaginary part $\Im(\hat{\epsilon}) = \frac{4\pi\sigma}{\omega}$ the absorption of the electromagnetic wave in a lossy material. The loss tangent $\tan\delta$ can be defined as [14]

$$\tan\delta = \frac{\epsilon_2}{\epsilon_1} \tag{2.4}$$

and characterizes the phase difference between $\mathbf{E}$ and $\mathbf{D}$.

2.2 Superconductivity

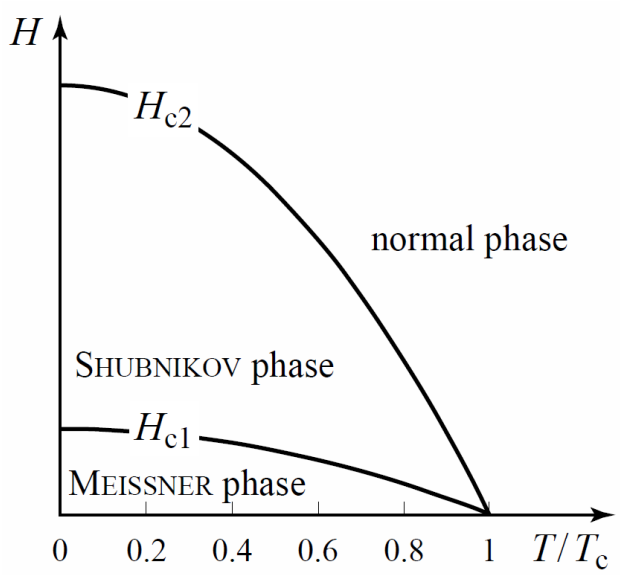

Fig. 2.1: Phases of the Type II superconductor with critical magnetic fields H_{c1} and H_{c2} and critical temperature T_c. In the Meißner state the superconductor exhibits the Meißner-Ochsenfeld effect, in the Shubnikov state vortices are formed in the superconductor and therefore the superconductor partially loses it's superconducting effects.

Superconductors are materials with a vanishing DC-resistance R_{DC} and superconductors eject an external magnetic field (Meißner-Ochsenfeld Effect). In this sense a superconductor is a perfect conductor and diamagnet. A material becomes a superconductor below a critical temperature T_c. The theoretical background of the superconducting state could be given by Bardeen, Cooper and Schrieffer with the BCS-theory who found that electrons exhibit an attractive interaction by exchanging virtual phonons [15]. Two electrons form a so-called Cooper-pair if the attractive interaction dominates the Coulomb-interaction.
A macroscopic view on superconductors is accessible with the London equations [16]. The London equations predict a penetration depth of the magnetic field in the material [17]

$$\lambda_L(T) = \sqrt{\frac{m_e c^2}{4\pi e^2 n_s(T)}} \tag{2.5}$$

where m_e and e are the mass and charge of the superconducting charge carriers. $n_s(T)$ is the density of the superconducting charge carriers. The dependence of $\lambda_L(T)$ on the temperature T is given by the empirical law [18]

$$\lambda_L(T) = \frac{\lambda_L(T=0)}{\sqrt{1-\left(\frac{T}{T_c}\right)^4}} \tag{2.6}$$

near T_c with the temperature dependent density of superconducting charge carriers $n_s(T)$ [18]

$$n_s(T) = n_s(T=0)\left(1 - \left(\frac{T}{T_c}\right)^4\right). \tag{2.7}$$

Superconductors can be divided into Type I and Type II superconductors [18]. Type I superconductors exhibit a critical magnetic flux density B_c, for an external magnetic flux density $B_{\text{ext}} < B_c$ the superconductor retains it's characteristic properties as the Meißner-Ochsenfeld effect and loses them for $B_{\text{ext}} > B_c$. Type II superconductors however exhibit two critical magnetic flux densities B_{c1} and B_{c2} with $B_{c1} < B_{c2}$. For $B < B_{c1}$ the Type II superconductor behaves like the Type I superconductor. For $B_{c1} < B < B_{c2}$ the Type II superconductor is in the Shubnikov phase. In the Shubnikov phase normal conducting filaments parallel to B occur that are referred to as vortices. When a current j is present in the superconductor a Lorentz-like force (Lorentz-like because the force is perpendicular to the current j and the direction of the vortex) drives the vortices resulting in increased losses of the current. In the Shubnikov phase the superconductor also does not dispel an external magnetic flux density B entirely.

2.3 Planar microwave resonators

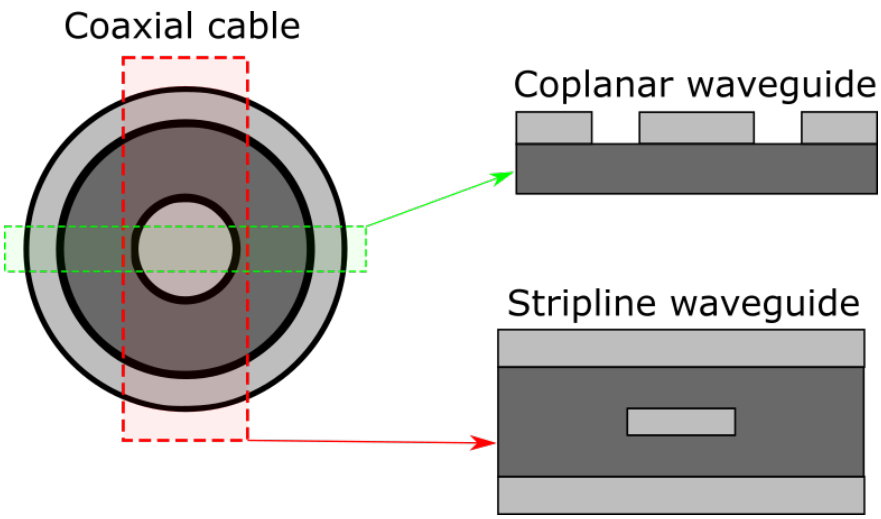

Fig. 2.2: Schematic cross-section of a coaxial cable, a coplanar waveguide and a stripline waveguide. The coplanar waveguide and stripline waveguide can be understood as a cut coaxial cable as implied in the figure.

Waveguides are structures that transmit electromagnetic waves. The most common example for such a structure is the coaxial cable as depicted in figure 2.2. A coaxial cable consists of an inner conducter and an outer conducter that are separated by a dielectric. The electromagnetic wave travels through the dielectric with accompanying current flowing in the inner and outer conductor. There are also other waveguide structures, such as the coplanar

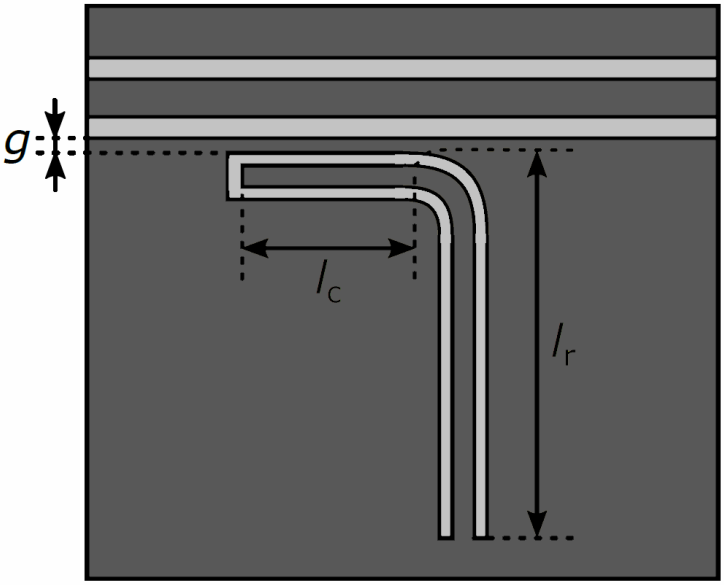

Fig. 2.3: Schematic top-view of a $\frac{\lambda}{4}$-resonator with coupling length l_c and total length $l = l_c + l_r$ coupled by the gap g to the feedline. Taken from [19] with adjusted colours to match figure 2.2.

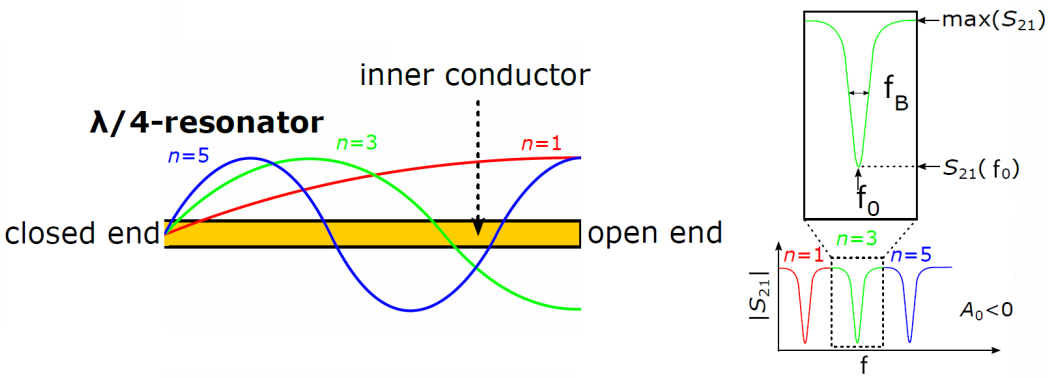

Fig. 2.4: Schematic representation of the occurring standing waves on a $\frac{\lambda}{4}$-resonator with the according transmission signal $|S_{21}|$. The standing waves represents the distribution of the electric field. The absorption resonance in the spectrum $|S_{21}|$ has a Lorentzian shape with half-power bandwidth f_b and resonance frequency f_0. Taken from [19].

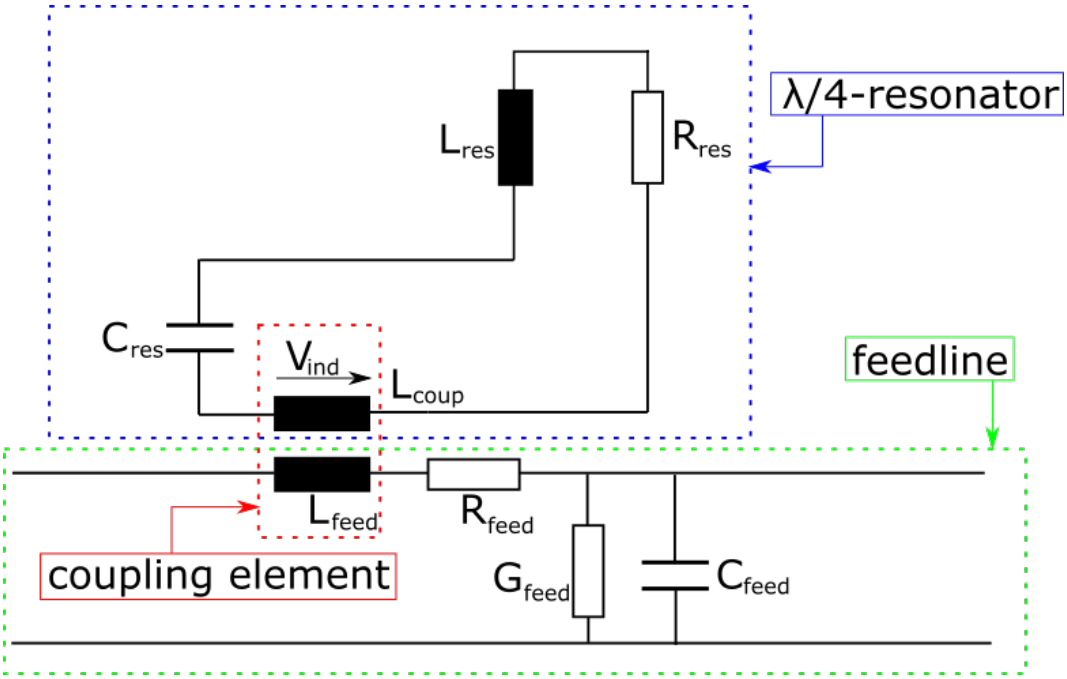

Fig. 2.5: Circuit diagram of a $\frac{\lambda}{4}$-resonator coupled inductively to a feedline with their according resistances R, capacitances C, inductances L and the conductance G_{feed}. The $\frac{\lambda}{4}$-resonator is driven by the coupling element, the resonator itself functions as a LRC-circuit as depicted in figure 2.6. If the frequency $\omega = 2\pi f$ of the transmitted TEM-wave in the feedline matches the resonance frequency $\omega_{\text{res}} = 2\pi f_{\text{res}}$ of the $\frac{\lambda}{4}$-resonator, energy is drained from the transmitted TEM-wave in the feedline which becomes visible in the spectrum as absorption loss with the shape of a Lorentzian as it is schematically depicted in figure 2.4.

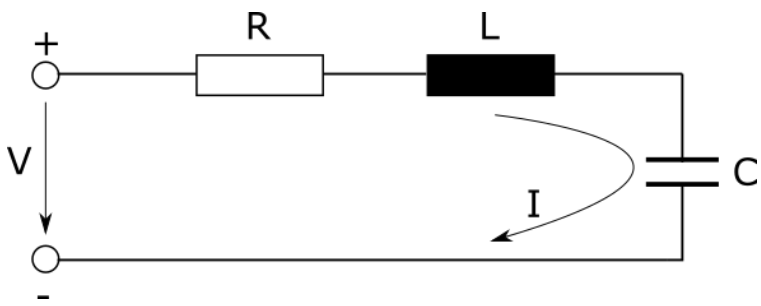

Fig. 2.6: Circuit diagram of a capacitance C, an inductance L and resistance R in series connection. A $\frac{\lambda}{4}$ resonator as depicted in figure 2.3 can be seen as such a series connection [20].

waveguide and the stripline waveguide that are also depicted in figure 2.2. A coplanar waveguide is a suitable tool to investigate the dielectric constant of dielectrics of interest as the waveguide is easy to manufacture with low losses and supports quasi-TEM modes [1].
A $\frac{\lambda}{4}$-resonator can be deposited on the dielectric of interest and coupled inductively to the feedline as schematically depicted in figure 2.3. A $\frac{\lambda}{4}$-resonator exhibits as fundamental mode a wavelength $\lambda = 4l$ where l is the total length of the resonator. A $\frac{\lambda}{4}$-resonator has an open and a closed end which allows only odd modes $n = 1, 3, 5, ...$ to occur. Standing waves on the $\frac{\lambda}{4}$-resonator occur when the wavelength of the standing wave fulfils the condition $\lambda = \frac{4l}{n}$. In this case the resonance frequency f_0 of the resonator is given by

$$f_0 = \frac{n v_{\text{ph}}}{4l} = \frac{nc}{4l\sqrt{\epsilon_{\text{eff}}}}, \quad n = 1, 3, 5, ... \tag{2.8}$$

where v_{ph} is the phase velocity and ϵ_{eff} depends on the dielectric constants ϵ_i of the materials that surround the waveguide and the waveguide's geometry. If the frequency $\omega = 2\pi f$ of the transmitted TEM-wave in the feedline matches the resonance frequency $\omega_0 = 2\pi f_0$ of the $\frac{\lambda}{4}$-resonator, energy is drained from the transmitted TEM-wave in the feedline. When measuring the transmission signal $|S_{21}(f)|$ of the feedline with a coupled $\frac{\lambda}{4}$-resonator in dependence of the frequency f, the resonances at the according resonance frequencies $n \cdot f_0$ can be observed as absorption losses with the shape of a Lorentzian as it is also schematically depicted in figure 2.4. When measuring the resonance frequency f_0 of a superconducting resonator, the temperature dependence of the penetration depth $\lambda_L(T)$ needs to be taken into account, because $\lambda_L(T)$ alters the geometry of the waveguide. Considering the London penetration depth $\lambda_L(T)$ from equation (2.6), the measured resonance frequency $f_{0,\text{meas}}$ can be modelled with [8]

$$f_{0,\text{meas}}(T) = \frac{f_0}{\sqrt{1 + \frac{\Gamma}{2} \frac{\lambda_L(T=0)}{\sqrt{1-\left(\frac{T}{T_c}\right)^4}}}}. \tag{2.9}$$

Here Γ is a geometrical factor that depends of the dimensions of the waveguide. The true resonance frequency f_0 that can be obtained with equation (2.9) is given by equation (2.8). It also needs to be taken into account that equation (2.9) is only valid for T near T_c.
In a mathematical approach to determine the effect of the inductively coupled $\frac{\lambda}{4}$-resonator one expresses the coupling between the feedline and the resonator with two coupled inductances L_{coup} and L_{feed} and adds a capacitance C_{res}, an inductance L_{res} and a resistance R_{res} to model the resonances with a LRC-circuit [20]. The circuit diagram for this setup can be seen in figure 2.5. The impedance Z_{Res} of the $\frac{\lambda}{4}$-Resonator is thus the same impedance as the one of a LRC-circuit as schematically depicted in figure 2.6 and given by [20]

$$Z_{\text{res}} = R_{\text{res}} + i\left(\omega(L_{\text{res}} + L_{\text{coup}}) - \frac{1}{\omega C}\right). \tag{2.10}$$

This way the impedance of the coupling element Z_{coup} can be given [21]

$$Z_{\text{coup}} = i\omega L_{\text{feed}} + \frac{\omega^2 \cdot M^2}{Z_{\text{res}}} = i\omega L_{\text{feed}} + \frac{\omega^2 \cdot M^2}{R_{\text{res}} + i\left(\omega(L_{\text{res}} + L_{\text{coup}}) - \frac{1}{\omega C}\right)}. \tag{2.11}$$

Equation 2.11 forms with the impedance $Z_{\text{remaining components}}$ of the remaining line components of the feedline the total impedance of the feedline

$$Z_{\text{feed}} = Z_{\text{coup}} + Z_{\text{remaining components}}. \tag{2.12}$$

Here the mutual inductance is given by $M^2 = \kappa^2 L_{\text{res}} L_{\text{coup}}$ [22] and consists of the product of the coupled inductances with a coupling factor κ. The quality factor Q of a resonator can be defined as [20]

$$Q = \omega \frac{W_{\text{stored}}}{P_{\text{loss}}} \tag{2.13}$$

the ratio of the average stored energy W_{stored} to the dissipated energy loss per second P_{loss} in the resonator. Equation (2.13) can be brought into the form [20]

$$Q = \frac{f_0}{f_b} = \omega_0 \frac{L_{\text{res}} + L_{\text{coup}}}{R} = \sqrt{\frac{L_{\text{res}} + L_{\text{coup}}}{C_{\text{res}}}} \frac{1}{R} \tag{2.14}$$

with the resonance frequency

$$\omega_0 = 2\pi f_0 = \frac{1}{\sqrt{(L_{\text{res}} + L_{\text{coup}})C_{\text{res}}}} \tag{2.15}$$

of the LRC-circuit and the half-power bandwidth f_b that is illustrated in figure 2.4. The quality factor Q is an important quantity to estimate the losses in the dielectric. Usually additional losses have to be taken into account when investigating resonators. The effects of the different losses can be modelled as resistance R_i of the resonator and summed up resulting in a quality factor [20]

$$\frac{1}{Q_{\text{all}}} = \frac{1}{Q_1} + \frac{1}{Q_2}. \tag{2.16}$$

With equation (2.11), (2.14), (2.15) and the approximation $\omega^2 - \omega_0^2 \approx 2\omega(\omega - \omega_0)$ that can be made for $\omega \approx \omega_0$ one can reformulate Z_{coup} and gets [21]

$$Z_{\text{coup}}(\omega) = i\omega L_{\text{feed}} - i\frac{1}{2(L_{\text{res}} + L_{\text{coup}})} \frac{\omega_0^2 M^2}{\omega - \omega_0 - i\frac{\omega_0}{2Q}}. \tag{2.17}$$

Equation (2.17) motivates a Lorentzian shaped complex fitting function [23]

$$S_{21}^{\text{meas}}(f) = e^{if\tau}\left(\frac{v_1}{f - v_2} + v_3 + v_4(f - \Re(v_2))\right) \tag{2.18}$$

for the measured transmission spectrum of the feedline. The coefficients v_3 and v_4 model the background with a Taylor expansion. The coefficients $v_1 = \frac{iA}{2f_b}$ and $v_2 = f_0 + i\frac{f_b}{2}$ model the Lorentzian. The phase shift τ is the running time and accounts the global oscillation. The coefficients v_i and τ are complex values, the behaviour of the complex fitting function is discussed more detailed in the Bachelor thesis of Konstantin Nikolaou [24].

2.4 Conformal mapping technique

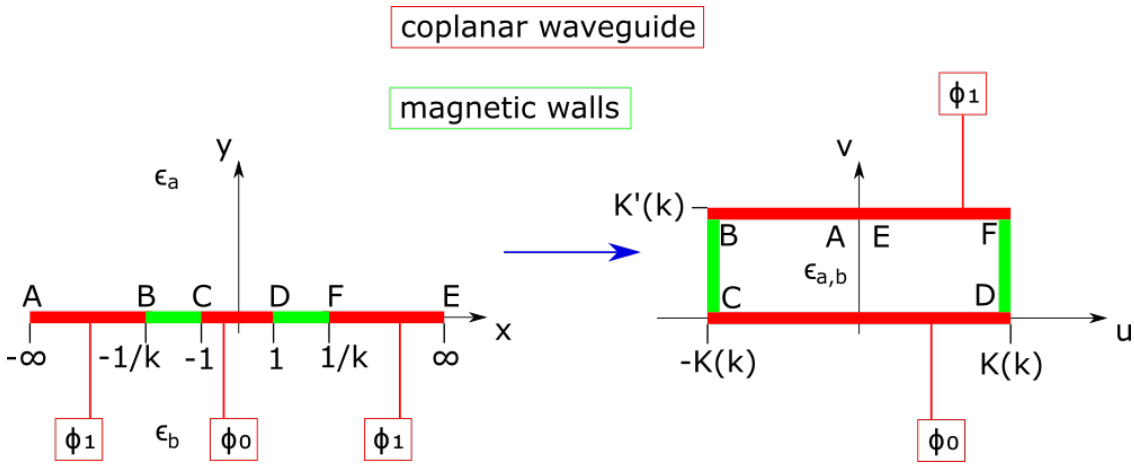

Fig. 2.7: Schematic cross-section view of the coplanar waveguide in xy-plane with the constant potentials ϕ_0 and ϕ_1 and $0 < k < 1$ and the magnetic walls and the mapped geometry in the uv-plane. A, B, C, D, E and F mark the mapped points. The upper half of the xy-plane $y > 0$ exhibits the dielectric constant ϵ_a and the lower half $y < 0$ exhibits ϵ_b. Only the upper or the lower half of the xy-plane can be mapped into the inner space of the uv-plane.

According to equation 2.8 the effective dielectric constant ϵ_{eff} can be obtained when measuring the resonance frequencies f_0 of the coplanar waveguide resonator. To access the desired dielectric constant ϵ of the material of interest one needs to solve the Laplace equation

$$\Delta_{xy}\phi = (\partial_x^2 + \partial_y^2)\phi = 0$$

to determine the effects of the geometry and the materials on ϵ_{eff}. In addition it is important to match the impedance of the coplanar feedline Z_{feed} to the common input impedance $Z_{\text{input}} = 50\,\Omega$ of most electric devices. This is a necessary step because the transmission signal S_{21} is measured and in order to provide a good signal-to-noise-ratio the reflection coefficient [21]

$$R = \left| \frac{Z_{\text{feed}} - Z_{\text{input}}}{Z_{\text{feed}} + Z_{\text{input}}} \right| \tag{2.19}$$

is minimized. Minimizing R requires an impedance of the feedline $Z_{\text{feed}} \approx 50\,\Omega$. As shown in figure 2.7 the solution of the Laplace equation needs to fulfil boundary conditions

which requires in the general case the determination of an appropriate Green's function. The calculation of Green's function is possible [25] but no suitable way as no closed-form expressions are derived. Complex transformations are a more suitable way. Complex transformations allow to map the geometry of the coplanar waveguide in the xy-plane in new coordinates $u(x, y)$ and $v(x, y)$ where the solution of the potential $\phi(u, v)$ is already known. $u(x, y)$ and $v(x, y)$ form the real and imaginary part of a holomorphic function

$$f(z = x + iy) = u(x, y) + iv(x, y) \tag{2.20}$$

and therefore fulfil the Cauchy-Riemann equations. The Laplace equation (2.4) is invariant under complex transformation. The invariance of the Laplace equation

$$\Delta_{uv}\phi = (\partial_u^2 + \partial_v^2)\phi = 0 \tag{2.21}$$

is a result of the validity of the Cauchy-Riemann equations [26].
A suitable mapping function that maps the coplanar waveguide into a plate capacitor as it can be seen in figure 2.7 is the inverse elliptic sinus function [21]

$$f(z = x + iy) = u(x, y) + iv(x, y) = \mathrm{sn}^{-1}(z, k) = \int_0^z \frac{\mathrm{d}z'}{\sqrt{(1 - z'^2) \cdot (1 - k^2 z'^2)}} \tag{2.22}$$

with $0 < k < 1$. The elliptic sinus function shows dual periodicity [27]

$$\begin{aligned} \mathrm{sn}(z, k) &= \mathrm{sn}(z + 4K(k), k) = \mathrm{sn}(z + i2K'(k), k) \\ \mathrm{sn}(z, k) &= -\mathrm{sn}(z + 2K(k), k) \end{aligned} \tag{2.23}$$

with special values

$$\begin{aligned} \mathrm{sn}(0, k) &= 0 \\ \mathrm{sn}(K(k), k) &= 1 \\ \mathrm{sn}(K(k) + iK'(k), k) &= \frac{1}{k} \\ \mathrm{sn}(iK'(k), k) &= \pm\infty. \end{aligned} \tag{2.24}$$

The dual periodicity is a suitable property that allows the mapping of a rectangle into a 1-dimensional structure. Here $K(k) = \mathrm{sn}^{-1}(1, k)$ is the complete elliptic integral of the first kind and $K'(k) = K(k' = \sqrt{1 - k^2})$ is the complementary complete elliptic integral of the first kind with modified $k'^2 = 1 - k^2$ [21].
The easiest case of a coplanar waveguide with vanishing thickness t and infinite width of the outer conductors as depicted in figure 2.7 can be mapped into a plate capacitor with known capacitance $C = \epsilon\frac{A}{d}$. One has to take into account that the upper half $y > 0$ and lower half

$y < 0$ of the coplanar waveguide are separately mapped into the inner space of the plate capacitor. This yields as capacitance C of the structure shown in figure 2.7

$$C = C_{\text{upper half}} + C_{\text{lower half}} = (\epsilon_a + \epsilon_b) \cdot \frac{2K(k)}{K'(k)}. \tag{2.25}$$

In general additional mapping functions are required to calculate the capacitance of coplanar waveguides with finite width of the outer conductor [28] or shielded coplanar waveguides with set thicknesses of the dielectrics [29]. Additional mapping functions would also determine k as a function of the real width of the inner conductor S and the distance between outer conductor and inner conductor W of the coplanar waveguide.

To calculate the capacitance C of a coplanar shielded waveguide the cross-section is divided

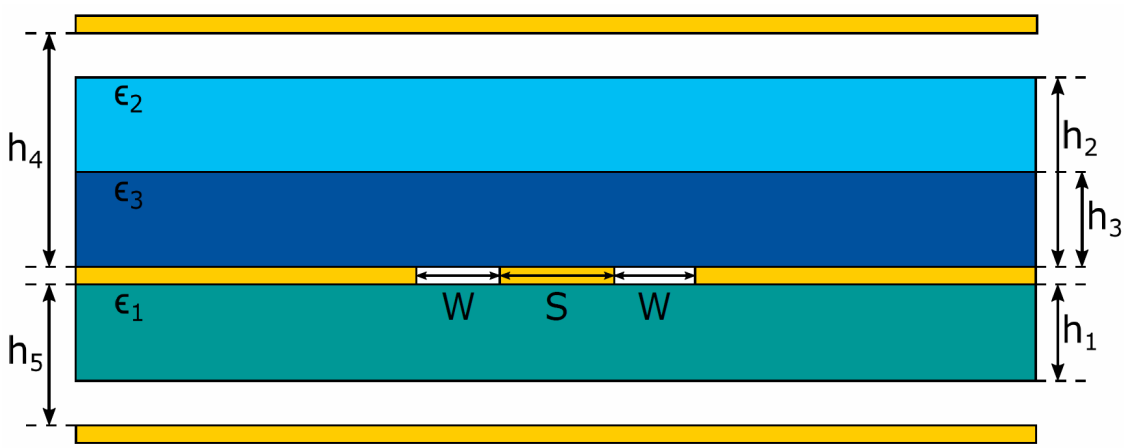

Fig. 2.8: Schematic cross-section view of the coplanar waveguide with the width S of the inner conductor and the distance W between the inner and outer conductor with infinite width of the outer conductor. The coplanar waveguide is surrounded by dielectrics with thicknesses h_1, $h_2 - h_3$ and h_3 and shielded by two plates at distances h_4 and h_5. Taken from [19].

into areas with different dielectric constant with partial capacitances C_i [29] as it can be seen in figure 2.8. The shielding at distances h_4 and h_5 functions a electric wall and contains only lateral **B**-field components and normal **E**-field components. The partial capacitances are given by [19]

$$\begin{aligned} C_1 &= 2\epsilon_0(\epsilon_{r1} - 1)\frac{K(k_1)}{K(k_1')} \quad \text{and} \quad C_2 = 2\epsilon_0(\epsilon_{r2} - 1)\frac{K(k_2)}{K(k_2')} \\ C_3 &= 2\epsilon_0(\epsilon_{r3} - \epsilon_{r2})\frac{K(k_3)}{K(k_3')} \quad \text{and} \quad C_{\text{air}} = 2\epsilon_0\left(\frac{K(k_4)}{K(k_4')} + \frac{K(k_5)}{K(k_5')}\right) \end{aligned} \tag{2.26}$$

with argument k_i in the unshielded case

$$k_i = \frac{\sinh\left(\frac{\pi S}{4h_i}\right)}{\sinh\left(\frac{\pi(S+2W)}{4h_i}\right)} \quad \text{for } i = 1, 2, 3 \tag{2.27}$$

and in the shielded case for the air capacitance

$$k_i = \frac{\tanh\left(\frac{\pi S}{4h_i}\right)}{\tanh\left(\frac{\pi(S+2W)}{4h_i}\right)} \quad \text{for } i = 4, 5. \tag{2.28}$$

In both cases the complementary argument is given by

$$k' = \sqrt{1 - k^2}. \tag{2.29}$$

The total capacitance is given by

$$C_{\text{CPW}} = C_1 + C_2 + C_3 + C_{\text{air}}. \tag{2.30}$$

For a shielded coplanar waveguide completely surrounded by air the total capacitance is given by $C_{\text{CPW}} = C_{\text{air}}$. The relative dielectric constant is given by the ratio of the total capacitances respectively filled with dielectrics and air which yields

$$\epsilon_{\text{eff}} = \frac{C_{\text{CPW}}}{C_{\text{air}}} = 1 + q_1(\epsilon_{r1} - 1) + q_2(\epsilon_{r2} - 1) + q_3(\epsilon_{r3} - \epsilon_{r2}) \tag{2.31}$$

for the effective dielectric constant of the coplanar waveguide with partial filling factors

$$q_i = \frac{K(k_i)}{K(k_i')} \cdot \left(\frac{K(k_4)}{K(k_4')} + \frac{K(k_5)}{K(k_5')}\right)^{-1}. \tag{2.32}$$

The impedance of the coplanar waveguide can be given with the capacitance C_{CPW} and transformed with equation (2.31) and (2.26)

$$Z = \frac{1}{v_{\text{ph}} C_{\text{CPW}}} = \frac{1}{c C_{\text{air}} \sqrt{\epsilon_{\text{eff}}}} = \frac{60\pi}{\sqrt{\epsilon_{\text{eff}}}} \cdot \left(\frac{K(k_4)}{K(k_4')} + \frac{K(k_5)}{K(k_5')}\right)^{-1}. \tag{2.33}$$

3 Experimental setup

3.1 VTI bath cryostat

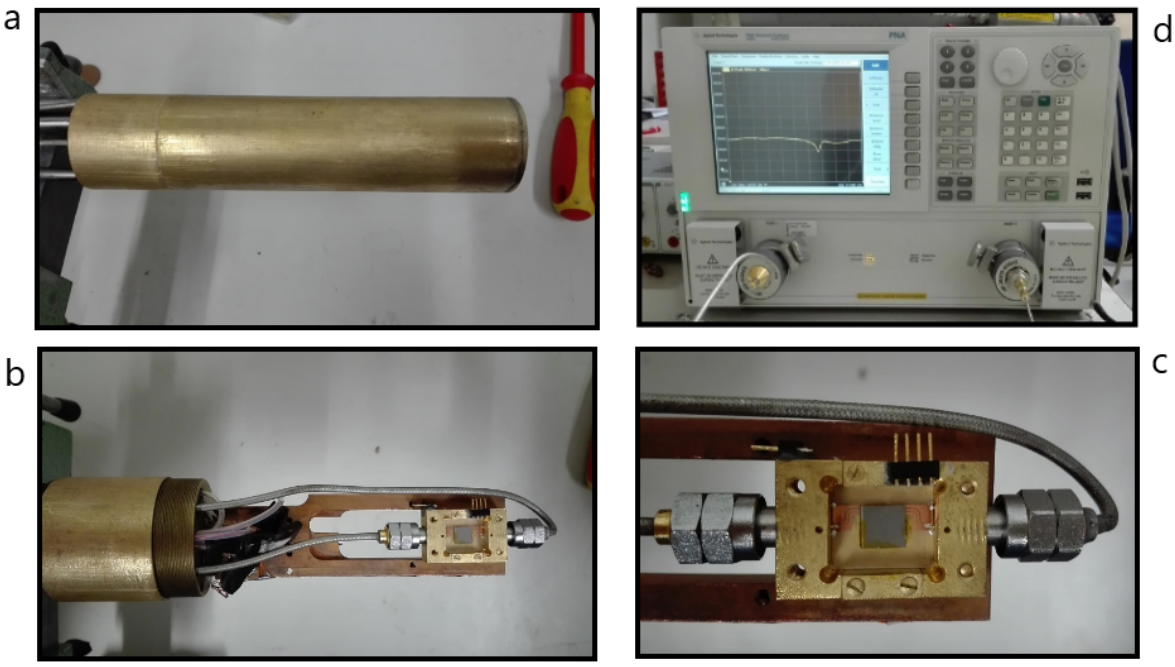

Fig. 3.1: (a) Closed sample holder. (b) Opened sample holder with the resonator mounted on the coplanar feedline in the resonator box. (c) Close up view on the microwave resonator within the resonator box. (d) Vector Network Analyzer.

The microwave measurements are performed at cryogenic temperatures down to $T = 2\,K$. The low measuring temperature requires liquid helium ^{4}He for cooling. The measurements are done in the variable temperature inset (VTI) bath cryostat. A schematic sketch of the experimental setup can be seen in figure 3.2. The microwave resonator is in the resonator box that is located in the sample holder as it can be seen in figure 3.1. The resonator box is made of brass and contains the coplanar feedline that can be connected via the resonator box to common coaxial cables. The Vector Network Analyzer (VNA) ((d) in figure 3.1) is connected to the feedline in the sample holder via the coaxial cables that lead from the VNA to the sample holder. The ^{4}He inflow from the ^{4}He-bath to the sample holder is controlled with the needle valve. The vacuum pump ensures the vacuum. The boiling temperature of helium amounts $T_S = 4.15\,\mathrm{K}$ at atmospheric pressure [30]. Temperatures below the boiling

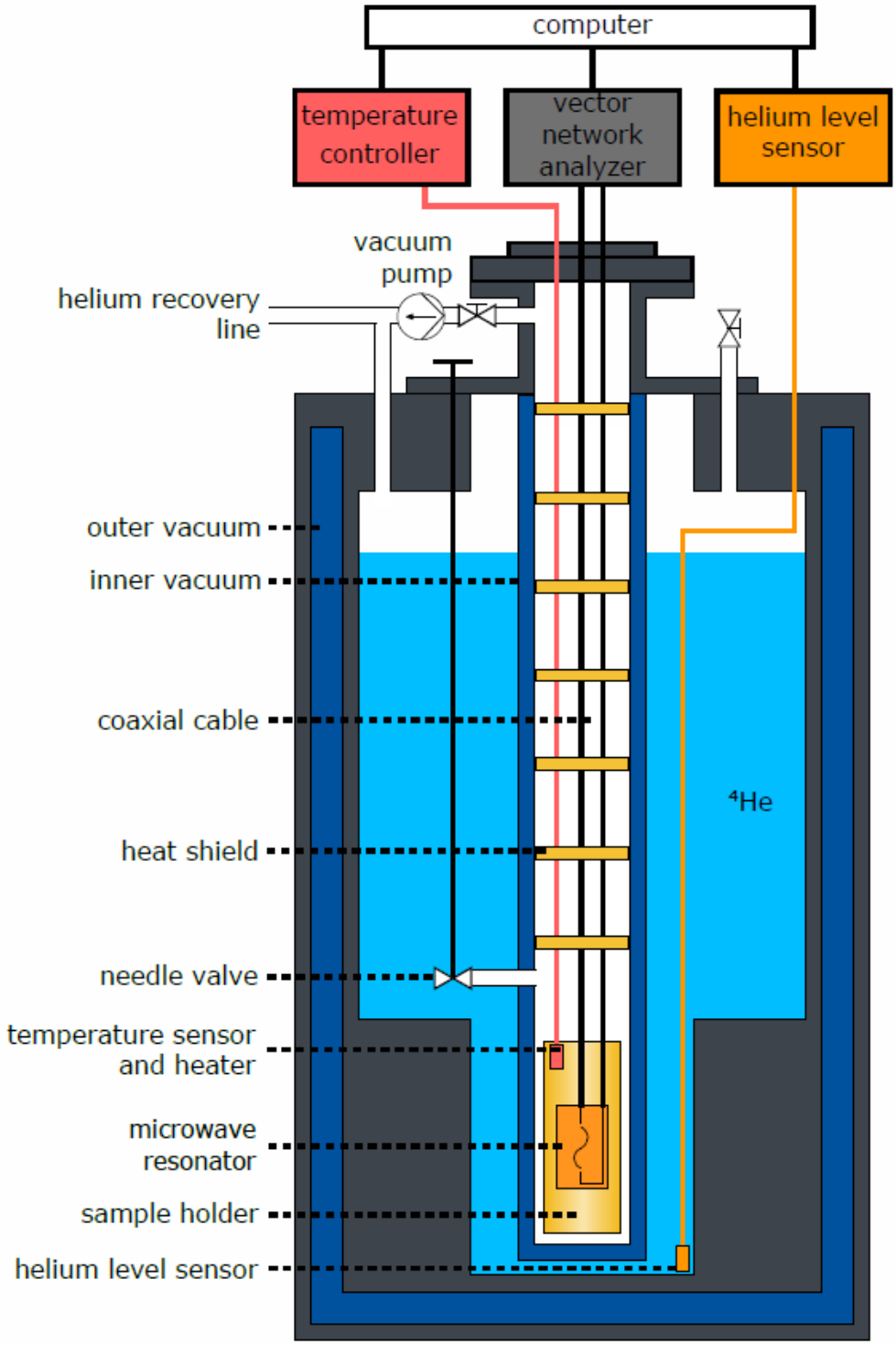

Fig. 3.2: Schematic representation of the VTI bath cryostat with the sample holder and the microwave resonator in the inner vacuum. Via the needle valve the ^{4}He inflow from the ^{4}He-bath to the sample holder can be controlled. The probe is connected with the Vector Network Analyzer (VNA) via the coaxial cable. The temperature controller controls and adjusts the temperature of the resonator via the temperature sensor and heater. The whole setup is surrounded with an outer vacuum. Taken from [19].

temperature of helium are accessible because of the inner vacuum that changes liquid helium into gaseous helium and therefore lowers the temperature of the sample holder by the amount of the enthalpy of vaporization of helium. In addition a superconducting solenoid is located in the helium bath that can provide a static magnetic field up to $B = 8\,\mathrm{T}$ with a precision of $\Delta B = 0.1\,\mathrm{mT}$ along the direction of the sample holder.

3.2 Vector Network Analyzer

By measuring the transmission coefficient S_{21} the microwave resonator can be investigated. The index 21 characterizes the transmission coefficient S_{21} as forward transmission (from Port 1 to Port 2). The Vector Network Analyzer (VNA) [31] allows to measure the transmission and reflection for a frequency range of $0.01\,\mathrm{GHz} < f < 50\,\mathrm{GHz}$ and a power range of $-75\,\mathrm{dBm} < p < 10\,\mathrm{dBm}$. The VNA can be seen in figure 3.1 in (d).
To measure the transmission signal for higher power $p > 10\,\mathrm{dBm}$ an additional setup consisting of a +23 dBm amplifier and a -20 dBm attenuator is required that modify the signal the VNA is measuring and detecting. The output signal of the VNA is amplified by 23 dBm and the input signal of the VNA is weakened by -20 dBm. This means the transmission signal needs to be rescaled as it could otherwise exceed $S_{21} > 1$ due to the 3 dBm gain. For high powers the non-linearity of the +23 dBm amplifier needs to be taken into account. The set power at the VNA in comparison to the power delivered to the flip-chip setup can be seen in table 3.1 for chosen values of p_{set} and more detailed in the appendix in table 6.1.

set power at VNA p_{set} [dBm]	-73	-53	-33	-13	-8	-3
power in the flip-chip setup p_{true} [dBm]	-50	-30	-10.1	9.2	13.4	16.8

Tab. 3.1: Set power p_{set} at the VNA and the transmitted power p_{true} to the coplanar waveguide itself. The power is amplified by 23 dBm for lower powers. The non-linearity of the amplifier needs to be taken into account for higher powers.

3.3 Flip-chip resonator

The flip-chip resonator setup differs from usually used resonator setups in the fact that the resonator and the feedline are placed on separate chips that are mounted in separate planes. A thin niobium film of thickness $t = 300\,\mathrm{nm}$ is sputtered on the dielectric of interest. Superconducting niobium has a critical temperature of $T_c = 9.26\,\mathrm{K}$ [32], however preceding measurements with superconducting flip-chip resonators [19] had shown that the measured $T_c \approx 8 - 9\,\mathrm{K}$ is slightly lower because the quality of the Nb-film depends on the quality of the sputtering process. The resonator is shaped by optical lithography. The resonator chip is then flipped onto the feedline at distance h. Mylar stripes of thickness $h_{\mathrm{Mylar}} = 50\,\mu\mathrm{m}$ between the feedline chip and the flip-chip ensure the desired set distance h, the mounting is done with GE varnish. Preceeding work of Marius Tochtermann showed that the use

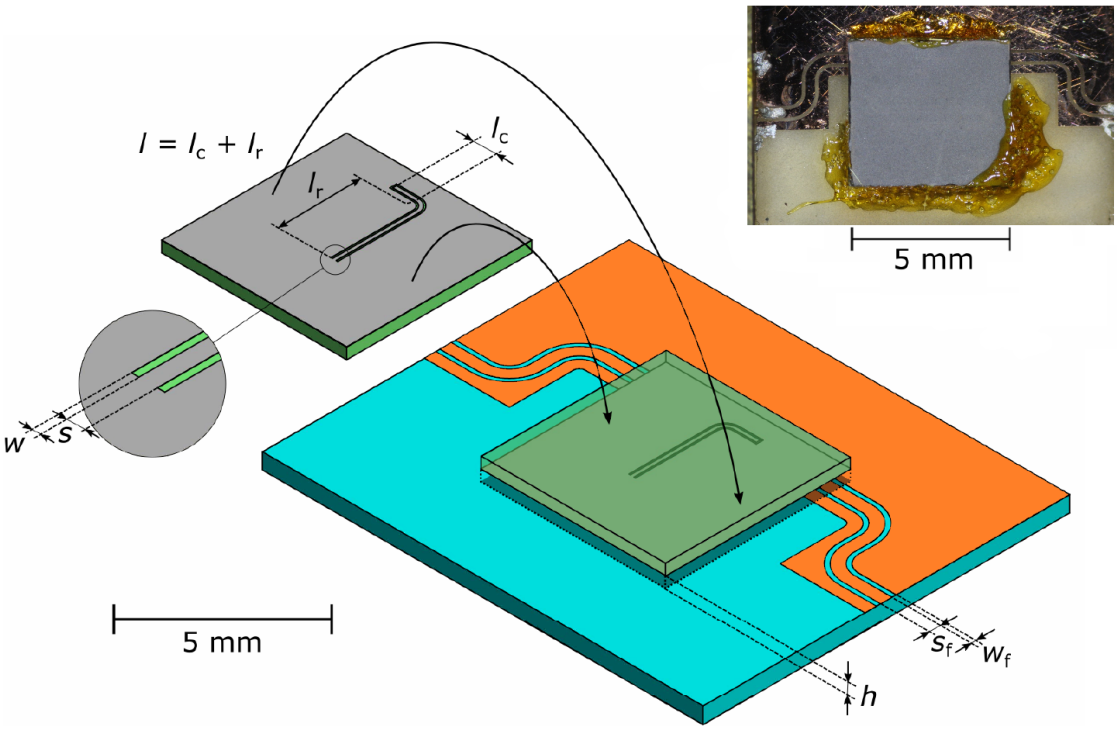

Fig. 3.3: Schematic representation of the flip-chip resonator setup. The Nb film is shown in grey, the copper film is shown in orange, the sapphire ground plane is shown blue, the dielectric of interest is shown in green. W and S characterizes the inner width and distance between outer conductor and inner conductor of the Nb-resonator and W_f and S_f characterizes the inner width and distance between outer and inner conductor of the copper feedline. The flip-chip resonator is mounted on the distance h over the feedline with the resonator facing towards the feedline. Taken from [19] with adjusted colours and a new inset that shows the new flip-chip resonator mounted on Mylar stripes and glued with GE.

of GE stabilizes the flip-chip setup [12]. The whole setup can be seen in figure 3.3. The quantities $W = 50\,\mu\text{m}$ and $S = 120\,\mu\text{m}$ characterize the inner width and distance between outer conductor and inner conductor of the Nb-resonator and $W_f = 120\,\mu\text{m}$ and $S_f = 300\,\mu\text{m}$ characterize the inner width and distance between outer and inner conductor of the copper feedline. As dielectric of interest titanium dioxide TiO_2 and strontium titanate $SrTiO_3$ are used.

The advantage of the flip-chip resonator is the shielding of the high dielectric constant of the dieletric of interest from the feedline. In order to measure the transmission S_{21} with a good signal-to-noise ratio it is desired to match the impedance of the feedline Z_f to the input impedance of $Z_0 = 50\,\Omega$ of most common electric devices. In figure 3.4 in (a) the cross-section view of the feedline with a deposited flip-chip resonator can be seen. Note that the Nb-film shields the material with dielectric constant ϵ_d, this means the impedance of the

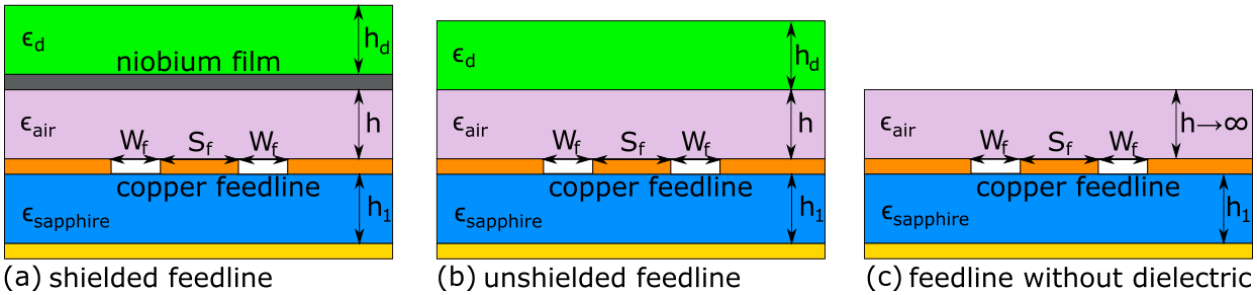

Fig. 3.4: Schematic cross-section view of the used flip-chip setup. In all cases the copper feedline is deposited on sapphire with thickness h_1. In (a) the dielectric (here with dielectric constant ϵ_d) with thickness h_d is placed with a set distance h to the copper feedline on top of the feedline with the niobium film facing towards the feedline, the Nb-film functions as a shielding layer. In (b) a bulk of the dielectric is placed on a distance h on top of the copper feedline. In (c) the copper feedline without a dielectric can be seen.

feedline is mainly effected by the dielectric constant $\epsilon_{\text{r-air}} = 1$ of air and $\epsilon_{\text{r-sapphire}} = 9.9$ of sapphire. The impedance Z of the shielded feedline can be calculated with equation (2.31)

$$\epsilon_{\text{eff-feedline}} = 1 + (\epsilon_{\text{r-sapphire}} - 1)\,\frac{\frac{K(k_{s1})}{K(k'_{s1})}}{\frac{K(k)}{K(k')} + \frac{K(k_1)}{K(k'_1)}} = 3.0 \tag{3.1}$$

where $k(h_i = h)$ and $k_1(h_i = h_1)$ are given by equation (2.28) and $k_{s1}(h_i = h_1)$ is given by equation (2.27) with $h = 70\,\mu\text{m}$, $h_1 = 450\,\mu\text{mm}$, $S_f = 300\,\mu\text{m}$ and $W_f = 120\,\mu\text{m}$. With equation (2.33) and (3.1) the impedance of the feedline

$$Z(\epsilon_{\text{eps-feedline}}) = \frac{60\pi}{\sqrt{\epsilon_{\text{eff-feedline}}}} \cdot \left(\frac{K(k)}{K(k')} + \frac{K(k_1)}{K(k'_1)}\right)^{-1} = 31.0\,\Omega \tag{3.2}$$

can be calculated.
For $h \to \infty$ an effective dielectric constant $\epsilon_{\text{eff-feedline}} = 5.0$ results with an impedance $Z(\epsilon_{\text{eps-feedline}}) = 47.9\,\Omega$. The condition $h \to \infty$ characterizes a coplanar feedline without the upper shielding and therefore without the flip-chip setup as it can be seen in (c) in figure 3.4. In this case the matching is possible with almost no reflections.
When calculating the effective dielectric constant of the feedline with a flipped high-ϵ bulk with thickness $h_d = 250\,\mu\text{m}$ on the feedline at distance $h = 70\,\mu\text{m}$, the setup as shown in (b) in figure 3.4 is present. In this case the dielectric constant ϵ_{r-d} disturbs the feedline resulting in an effective dielectric constant

$$\epsilon_{\text{eff-feedline}} = 1 + \frac{(\epsilon_{\text{r-sapphire}} - 1)\,\frac{K(k_{s1})}{K(k'_{s1})} + (\epsilon_{\text{r-d}} - 1) \cdot \left(\frac{K(k_{s2})}{K(k'_{s2})} - \frac{K(k_s)}{K(k'_s)}\right)}{\frac{K(k)}{K(k')} + \frac{K(k_1)}{K(k'_1)}} \tag{3.3}$$

Cases of feedline	$\epsilon_{\text{eff-feedline}}$ [1]	$Z(\epsilon_{\text{eff-feedline}})$ [Ω]	R [1]
Shielded feedline with flip-chip (a)	3.0	31.0	0.23
Unshielded feedline with TiO_2 flip-chip (b)	23.4	11.1	0.64
Unshielded feedline with $SrTiO_3$ flip-chip (b)	2056	1.2	0.98
Unshielded feedline without flip-chip (c)	5.0	47.9	0.02

Tab. 3.2: Effective dielectric constants $\epsilon_{\text{eff-feedline}}$, impedances Z and reflection coefficients $R(Z_{\text{input}} = 50\,\Omega, Z_{\text{feed}} = Z)$ from equation (2.19) of the feedline in the case of shielded and unshielded dielectrics in the flip-chip setup. The schematic cross-section of the feedline in the different cases can be seen in figure 3.4.

with the same values for k, k_1 and k_{s1} as used in equation (3.1) and $k_{s2}(h_i = h + h_d)$ and $k_s(h_i = h)$ from equation (2.27). The impedance Z can be calculated with equation (2.33). Using the dielectric constant of TiO_2 $\epsilon_{r-d} = \epsilon_{\text{r-TiO}_2} \approx 200$ [33] at cyrogenic temperatures yields $\epsilon_{\text{eff-feedline}} = 23.4$ and $Z(\epsilon_{\text{eff-feedline}}) = 11.1\,\Omega$. When using the even higher dielectric constant of $SrTiO_3$ with $\epsilon_{r-d} = \epsilon_{\text{r-SrTiO}_3} \approx 20\,000$ at cryogenic temperatures [34] an effective dielectric constant $\epsilon_{\text{eff-feedline}} = 2056$ with an impedance $Z(\epsilon_{\text{eff-feedline}}) = 1.2\,\Omega$ can be obtained. The results for the effective dielectric constants of the feedline $\epsilon_{\text{eff-feedline}}$ with the impedances Z are summarized in table 3.2. Although $Z(\epsilon_{\text{eff-feedline}}) = 31.0\,\Omega$ in the shielded case does not match the required input impedance $Z = 50\,\Omega$, it results only in a relatively small reflection coefficient $R = 0.23$ compared to the reflections coefficients $R(\text{SrTiO}_3) = 0.98$ and $R(\text{TiO}_2) = 0.64$ that would result in the unshielded case.

4 Analysis

4.1 Approach to the analysis

When measuring the resonance frequency of flip-chip $\frac{\lambda}{4}$-resonators one expects odd multiples $n = 1, 3, 5, ...$ of the resonance frequency $f(n) = nf(n = 1)$. This has already been measured by Engl [11] and Wendel [10] for a wide variety of samples. Open questions remain concerning the parasitic modes of the resonator and their origin. For TiO_2, a sample that is well understood, the parasitic modes can be distinguished from the resonator modes by considering only the odd multiples of the fundamental mode. However when the fundamental mode $n = 1$ is missing as it is the case in the work of Engl [11], identifying the resonator modes is not obvious.
Therefore it is appropriate to investigate a well understood sample as TiO_2 again, but now with additional focus on the parasitic modes. By varying external parameters as the temperature T, the magnetic flux density B or the power p the behaviour of the parasitic modes and the resonator modes is observed in order to distinguish them. The analysis section for the measurements on TiO_2 is structured as followed:

- First general considerations concerning the anisotropic dielectric constant ϵ of TiO_2 are made.
- Next the spectrum of TiO_2 is investigated to extract the resonance frequencies and to compare them with already known data from Wendel [10] and with the theoretical expected values as they would result from the anisotropic ϵ.
- Both resonator modes and parasitic modes and their dependence on the temperature T is investigated.
- Again both resonator modes and parasitic modes are investigated and their dependence on the magnetic flux density B is observed and classified.
- An ESR measurement is executed on both the resonator modes and parasitic modes with DPPH (abbreviation for 2,2-diphenyl-1-picrylhydrazyl). The ESR measurement is considered as a fingerprint method to investigate the resonators as it returns a sharp signal that is directly dependent on the distribution of the magnetic field of the resonator mode.
- Last the power p dependence of both resonator modes and parasitic modes are investigated.

In addition, the off-resonant transmission signal of the TiO_2 and $SrTiO_3$ flip-chip setup is compared for different temperatures.

4.2 Measurements with TiO_2

4.2.1 Anisotropic dielectric constant ϵ of TiO_2

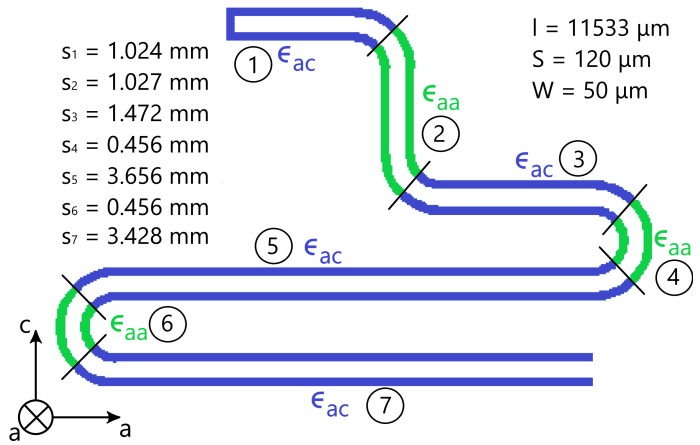

Fig. 4.1: Schematic top-view of the flip-chip resonator on TiO_2 with total length $l = 11533\,\mu\text{m}$ and parameters $S = 120\,\mu\text{m}$, $W = 50\,\mu\text{m}$. The dielectric constant ϵ_{ac} parallel to the meander structure differs from the dielectric constant ϵ_{aa} perpendicular to the meander structure. The stated values s_i are the lengths of the different sections of the resonator.

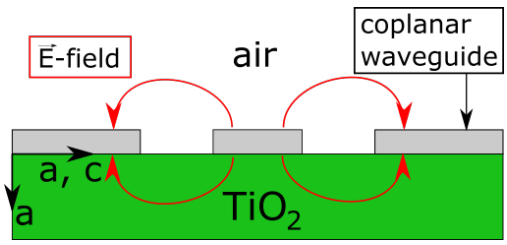

Fig. 4.2: Schematic representation of the cross section of the flip-chip resonator with the coplanar waveguide deposited on TiO_2 and the according **E**-field lines. Depending on the direction of the coplanar waveguide in figure 4.1 the **E**-field is located in the ac-plane or the aa-plane.

Titanium dioxide TiO_2 is a material with anisotropic relative dielectric constant $\epsilon_{\text{c}} = 256$ in c-direction and $\epsilon_{\text{a}} = 131$ in a-direction [33] in the microwave regime at temperature $T = 4.2\,\text{K}$. Similar values were obtained in a static electric field [35]. The loss tangent $\tan\delta = 2.5 \cdot 10^{-6}$ [33] is relatively small. In this thesis the TiO_2 flip-chip resonator of Lars Wendel with total length $l = 11533\,\mu\text{m}$ is used [10]. Wendel's work yielded a relative dielectric constant of $\epsilon_{ac} = 156$ and $\epsilon_{aa} = 120$ when measured with the flip-chip setup at cryogenic temperatures for the $n = 5$ mode. The flip-chip of TiO_2 is schematically depicted in figure 4.1 as well as the according sections it is divided into. The **E**-field is located in the ac-plane or the aa-plane [10] depending on the direction of the waveguide as depicted in figure 4.2. As result

the measured dielectric constant ϵ_{ac} in the *ac*-plane can approximately be understood as the mean value $\epsilon_{ac} = \frac{\epsilon_a + \epsilon_c}{2}$.

The distribution of the electric or magnetic field in a meander-shaped $\frac{\lambda}{4}$-resonator as it is

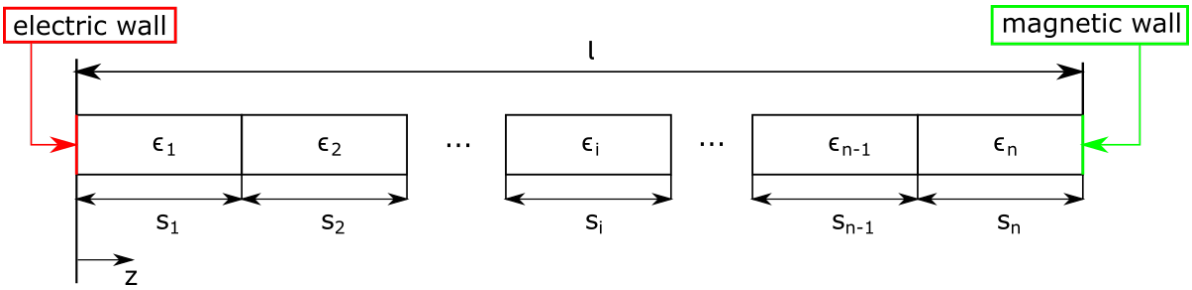

Fig. 4.3: Schematic $\frac{\lambda}{4}$-resonator with length l divided into n sections with partial length s_i with dielectric constant ϵ_i and bounded by a electric and magnetic wall. The E-field component of a standing wave exhibits a non-vanishing component at the magnetic wall and vanishes at the electric wall and vice versa for the B-field component

present here with anisotropic ϵ can be calculated in the general case if the resonator is split into sections with respective partial length s_i and their according dielectric constants ϵ_i as depicted in figure 4.3. Furthermore a harmonic time dependence $\partial_t E = i\omega E$ with frequency $\omega = 2\pi f$ is assumed. In this case the Helmholtz equation that describes the distribution of the electric component E in the resonator can be given [21]

$$\partial_z^2 E_i = -k_i^2(\epsilon = \epsilon_i)E_i = -\epsilon_{ri} k_0^2(\epsilon = \epsilon_0)E_i. \tag{4.1}$$

Equation (4.1) can be solved for each section separately which yields for the distribution of the electric field E

$$E_i(z) = A_i \sin(k_i \cdot (z - h_i)) + B_i \cos(k_i \cdot (z - h_i)) \tag{4.2}$$

with

$$h_i = \sum_{j=1}^{i} s_j \tag{4.3}$$

and $2n$ integration coefficients A_i, B_i with $1 \leq i \leq n$. Here $k_i(\epsilon_i)$ describes the absolute value of the wave vector

$$k_i(\epsilon = \epsilon_i) = |\mathbf{k}_i(\epsilon = \epsilon_i)| = \frac{\omega}{v_i} = \sqrt{\epsilon_{ri}}\frac{\omega}{c} = \sqrt{\epsilon_{ri}} k_0(\epsilon = \epsilon_0) \tag{4.4}$$

with phase velocity v_i where the index i accounts for the dependence of k_i on the dielectric constant ϵ_{ri} and $k_0 = \frac{\omega}{c}$ is the wave vector in vacuum that contains the same value for all considered sections.

The integration coefficients are determined by the boundary condition the electric and

magnetic wall request and by the continuity of E and the derivative $\partial_z E$ at the interface of two sections

$$\begin{aligned} E_1(z=0) &= 0 \\ E_n(z=l) &= E_{\max} \\ E_i\left(z=h_i\right) &= E_{i+1}\left(z=h_i\right) \text{ for } 1 \leq i \leq n-1 \\ \partial_z E_i(z)|_{z=h_i} &= \partial_z E_{i+1}(z)|_{z=h_i} \text{ for } 1 \leq i \leq n-1. \end{aligned} \tag{4.5}$$

The integration coefficients $B_1 = A_1 \tan(k_1 s_1)$ and $B_n = E_{\max}$ can be given as well as the dependence of the integration coefficients $A_{i+1}(A_i, B_i)$ and $B_{i+1}(A_i, B_i)$ on the previous coefficients

$$\begin{aligned} A_{i+1} &= \delta_{i+1} A_i \cos(k_{i+1} s_{i+1}) - B_i \sin(k_{i+1} s_{i+1}) \\ B_{i+1} &= \delta_{i+1} A_i \sin(k_{i+1} s_{i+1}) + B_i \cos(k_{i+1} s_{i+1}) \end{aligned} \tag{4.6}$$

with $\delta_{i+1} = \sqrt{\frac{\epsilon_i}{\epsilon_{i+1}}}$. Equation (4.6) can also be brought into matrix form and iterated

$$\begin{pmatrix} A_i \\ B_i \end{pmatrix} = M_i M_{i-1} ... M_3 M_2 \begin{pmatrix} A_1 \\ B_1 \end{pmatrix} = \prod_{j=2}^{i} M_{i+2-j} \begin{pmatrix} A_1 \\ B_1 \end{pmatrix} \tag{4.7}$$

with iterating matrix

$$M_i = \begin{pmatrix} \delta_i \cos(k_i s_i) & -\sin(k_i s_i) \\ \delta_i \sin(k_i s_i) & \cos(k_i s_i) \end{pmatrix}. \tag{4.8}$$

With

$$\begin{aligned} \begin{pmatrix} A_1 \\ B_1 \end{pmatrix} &= A_1 \begin{pmatrix} 1 \\ \tan k_1 s_1 \end{pmatrix} \\ \begin{pmatrix} A_n \\ B_n \end{pmatrix} &= \begin{pmatrix} A_n \\ E_{\max} \end{pmatrix} \\ \mathbf{f} = \begin{pmatrix} f_1 \\ f_2 \end{pmatrix} &= \prod_{j=2}^{n} M_{n+2-j} \begin{pmatrix} 1 \\ \tan(k_1 s_1) \end{pmatrix} \end{aligned} \tag{4.9}$$

and equation (4.7) for $i = n$ the following expression can be obtained

$$\begin{pmatrix} A_n \\ E_{\max} \end{pmatrix} = A_1 \begin{pmatrix} f_1 \\ f_2 \end{pmatrix} \tag{4.10}$$

which determines $A_1 = \frac{E_{\max}}{f_2}$ and $A_n = E_{\max} \frac{f_1}{f_2}$. $\mathbf{f}$ compresses the product over the iterating matrices and therefore accounts for the anisotropic ϵ.
The additional requirement

$$\partial_z E_n(z)|_{z=l} = 0 \tag{4.11}$$

is only fulfilled for standing waves and sets as further condition $A_n k_n = 0$ which returns as condition for standing waves

$$\frac{f_1}{f_2} k_n = 0. \tag{4.12}$$

For an isotropic ϵ, δ_i is given by $\delta_i = 1$ and the absolute value of the wave vector is the same for every section $k_i = k$. As consequence $M_i(\delta_i = 1)$ is a rotation matrix with argument ks_i. In this case $\mathbf{f}$ can be easily determined to

$$\mathbf{f} = \frac{1}{\cos(ks_1)} \begin{pmatrix} \cos(kl) \\ \sin(kl) \end{pmatrix} \tag{4.13}$$

which allows to reformulate the condition for standing waves (4.12) to

$$\frac{1}{\tan kl} = 0. \tag{4.14}$$

Equation (4.14) yields the already known resonance frequency from (2.8) showing that the considerations made here yield in the special case of $\delta_i = 1$ the already known solution.

4.2.2 Spectrum of Nb resonator on TiO_2

mode n	f [GHz] Wendel [36]	$f^{\text{corr.}}$ [GHz]	f [GHz] Fig. 4.4	$f^{\text{corr.}}$ [GHz]
1	0.747	0.754	0.752	0.759
3	2.21	2.22	2.21	2.24
5	3.65	3.68	3.62	3.66
7	5.15	5.19	5.08	-
9	6.63	6.68	6.53	6.59
11	8.07	8.14	7.99	8.06
13	9.67	9.75	9.55	9.65
15	11.24	11.33	11.06	11.14
17	12.58	12.68	12.38	12.48
19	-	-	13.73	13.86

Tab. 4.1: Measured resonances frequencies f and corrected resonance frequencies f^{corr} according to equation (4.16) from Lars Wendel [36] and from figure 4.4. Note that the $n = 7$ mode as seen in figure 4.4 in (c) is not corrected as it was not measured in dependence of T.

In figure 4.4 in (a) the measured spectrum of the TiO_2 flip-chip resonator at temperature $T = 2\,\text{K}$ can be seen. The measured spectrum exhibits resonator modes $n = 1, 3, 5, ...$ as well as parasitic modes PI-PVI. All characterized modes vanish above T_c of the superconducting Nb-layer on the flip-chip. The $n = 1$ and $n = 7$ modes are not visible in figure 4.4 in (a) as the $n = 1$ mode exhibits a high quality factor Q and the $n = 7$ mode shows a small absorption loss that is even smaller than the standing waves of the background. The standing waves

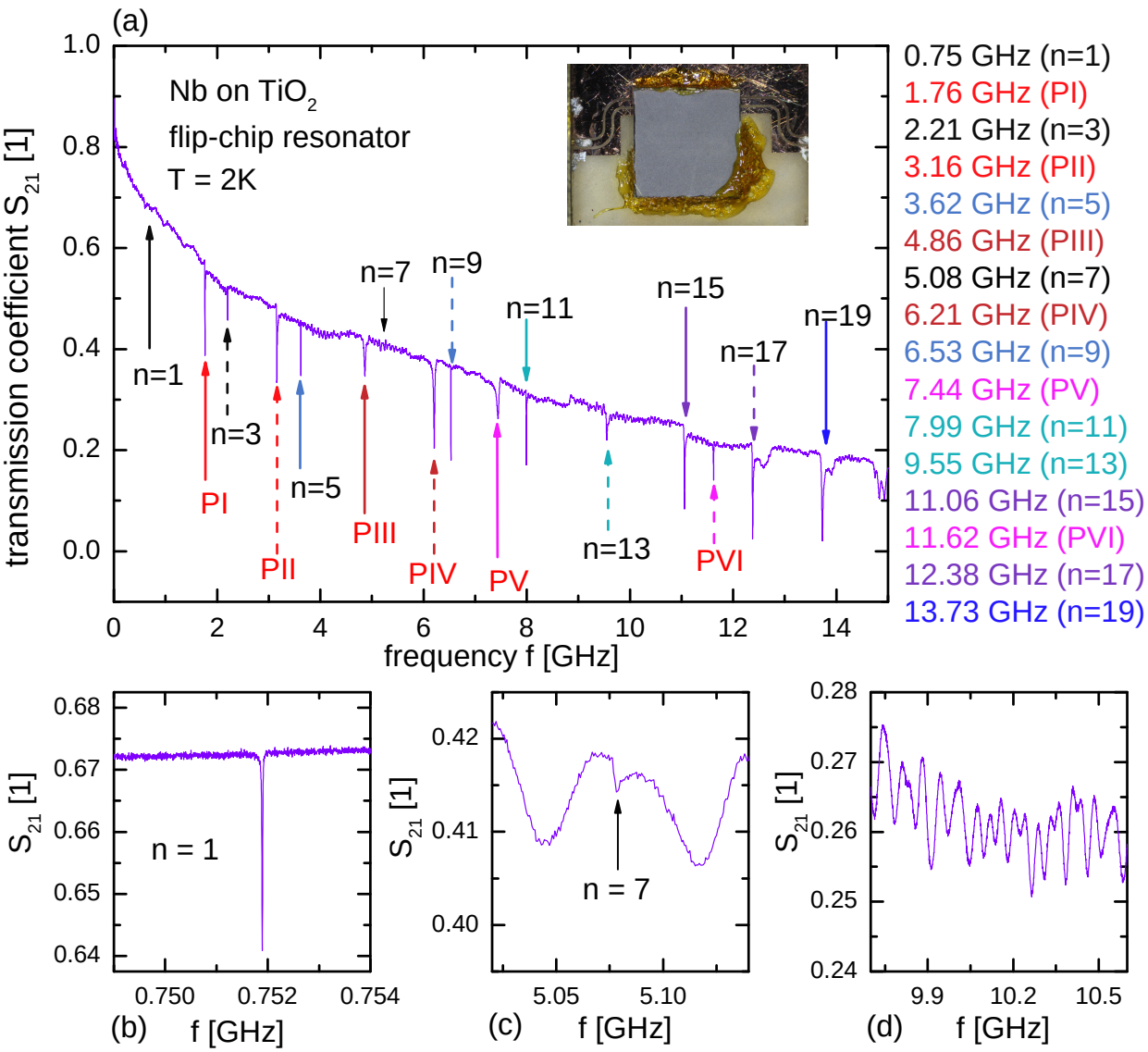

Fig. 4.4: In (a) the measured transmission coefficient S_{21} in frequency range $0.05\,\mathrm{GHz} < 15\,\mathrm{GHz}$ of the TiO_2 flip-chip resonator at temperature $T = 2\,\mathrm{K}$ can be seen. Here PI-PVI characterize the parasitic modes. Resonator modes are colour-coded in black, blue and violet whereas parasitic modes are colour-coded in shades of red. (b) shows a close-up view on the $n = 1$ and (c) shows a close-up view on the $n = 7$ mode. (d) shows the standing waves in the broadband background of the transmission coefficient.

mode n	$f^{\text{corr.}}$ [GHz] Wendel	$f^{\text{corr.}}$ [GHz] Fig. 4.4	f [GHz] odd n	f [GHz] anis. ϵ
1	0.754	0.759	0.752	0.751
3	2.22	2.24	2.26	2.23
5	3.68	3.66	3.76	3.68
7	5.19	-	5.26	5.13
9	6.68	6.59	6.77	6.62
11	8.14	8.06	8.27	8.14
13	9.75	9.65	9.78	9.71
15	11.33	11.14	11.28	11.23
17	12.68	12.48	12.78	12.66
19	-	13.86	14.29	14.13

Tab. 4.2: Corrected resonances frequencies f^{corr} from Lars Wendel [36] and from figure 4.4. The expected resonance frequencies f for odd multiple of the n=1 mode and when calculating for anisotropic ϵ according to the condition formulated in (4.12).

of the background can be seen in figure 4.4 in (d) and are the result of small impedance mismatching of the coaxial cable and coplanar waveguide or the output at the VNA that lead to standing waves along the feedline. These standing waves are the cause of the fluctuations of the transmission signal S_{21} that also limit the accuracy of the resonance measurements. When zooming into the transmission signal, the $n = 1$ and $n = 7$ modes can be observed in the spectrum as depicted respectively in (b) and (c) in figure 4.4. The absorption loss of the $n = 7$ mode is smaller than the standing waves which complicates fitting when it is also taken into account that the $n = 7$ mode can shift in frequency f when a control parameter as the temperature T, power p or the B-field is varied. Therefore the $n = 7$ mode is not investigated in the succeeding sections.
The observed resonance frequencies f in figure 4.4 are listed in table 4.1 with the measured resonance frequencies f from Lars Wendel [36]. The measured resonance frequency has to be corrected, because the London penetration depth λ_L alters the width of the inner conductor S and the gap W which affects f. The measured resonance frequencies f can be corrected by measuring f in dependence of T and fitting them with equation (2.9). The process of fitting is described in the succeeding section where the temperature-dependent behaviour of the modes is investigated, the corrected resonance frequencies $f^{\text{corr.}}$ are already given in table 4.1 and table 4.2.
The expected resonance frequencies of TiO_2 can be calculated with the condition formulated in equation (4.12). The measured dielectric constant of Lars Wendel amount to $\epsilon_{ac} = 156$ and $\epsilon_{aa} = 120$ for the $n = 5$ mode as previously mentioned. Wendel calculated these dielectric constants according to equation (2.8) and (2.9) by measuring and correcting the resonance frequencies of the meander-shaped resonator. The designation of the dielectric constants as ϵ_{ac} and ϵ_{aa} is actually imprecise, because the meander-shaped resonator always contains section parallel to the ac plane and the aa plane (Wendel himself did not name his measured dielectric constants ϵ_{aa} or ϵ_{ac}). But his investigated meander-shaped resonator as one of them can be seen in figure 4.1 exhibit mainly sections in the ac plane or the aa plane, therefore it

could be assumed that the measured resonance frequency would be mainly effected by the dielectric constant ϵ_{ac} or ϵ_{aa}. So his calculated values are slightly disturbed. So in addition, it is now assumed that the true dielectric constant $\epsilon_{\text{ac}}^{\text{true}} = \epsilon_{\text{ac}} + 6 = 162$ and $\epsilon_{\text{aa}}^{\text{true}} = \epsilon_{\text{aa}} - 6 = 114$ are given by a shift in opposite direction. For high dielectric constants, the effective dielectric constant can be assumed as $\epsilon_{\text{eff}} = \frac{\epsilon}{2}$. The effective dielectric constant can be calculated to

$$\begin{aligned} \epsilon_{\text{ac-eff}} &= 81 \\ \epsilon_{\text{aa-eff}} &= 57. \end{aligned} \tag{4.15}$$

The length s_i of the sections the resonator is divided into can be seen in figure 4.1. The expected resonance frequencies f calculated according to (4.12) are listed in table 4.2. In table 4.2 are also listed the corrected resonance frequencies by Wendel and the corrected resonance frequencies in this thesis obtained from figure 4.4 along with the odd multiples of the fundamental mode $n = 1$. For an anisotropic ϵ it can be seen that the calculated resonance frequencies for $n \geq 3$ is always lower than the odd multiples of the fundamental mode. The obtained data in this thesis as well as Lars Wendel's data with exception of the $n = 9$ also exhibit this feature. This is a result of the distribution of the electric field, mode $n = 1$ contains in section s_2 with ϵ_{aa} in figure 4.1 the highest **E**-field component when compared to the other modes. In general it can be seen that for $1 \leq n \leq 9$ the calculated resonance frequencies match the obtained data better than the odd multiples. For higher modes the calculated and measured data differ more because small deviations tend to have greater effects on the resonance frequencies for higher n, this is the result of smaller wavelengths λ that are more easily disturbed when the partial lengths s_i of the sections are rounded and therefore not given correctly.

4.2.3 Temperature dependence of TiO_2 modes

It is expected that no temperature-dependent effects due to the TiO_2 substrate occur for $T < 10\,\text{K}$ [33]. Temperature-dependent effects are expected to be caused by the superconducting niobium film on the flip-chip resonator as the density of superconducting charge carrier $n_s(T)$ depends heavily on the temperature as seen in equation (2.7).
The dependence of the resonance frequency $f(T)$ of the identified modes in figure 4.4 on the temperature T can be seen in figure 4.5. The resonance frequency f is normalized to the measured data at $T = 2\,\text{K}$. A decrease of the frequency f can be seen for all modes as expected from equation (2.9). Equation (2.9) can be used as a fit function

$$f(T) = \frac{f^{\text{corr.}}}{\sqrt{1 + \frac{A}{\sqrt{1-\left(\frac{T}{T_c}\right)^4}}}} \tag{4.16}$$

to correct the resonance frequencies $f(T)$ in dependence of T. Here $f^{\text{corr.}}$ is the corrected resonance frequency, A is a fit coefficient and T_c is the critical temperature of niobium, all three quantities are the fit parameter. The fit in equation (4.16) of the temperature-dependent

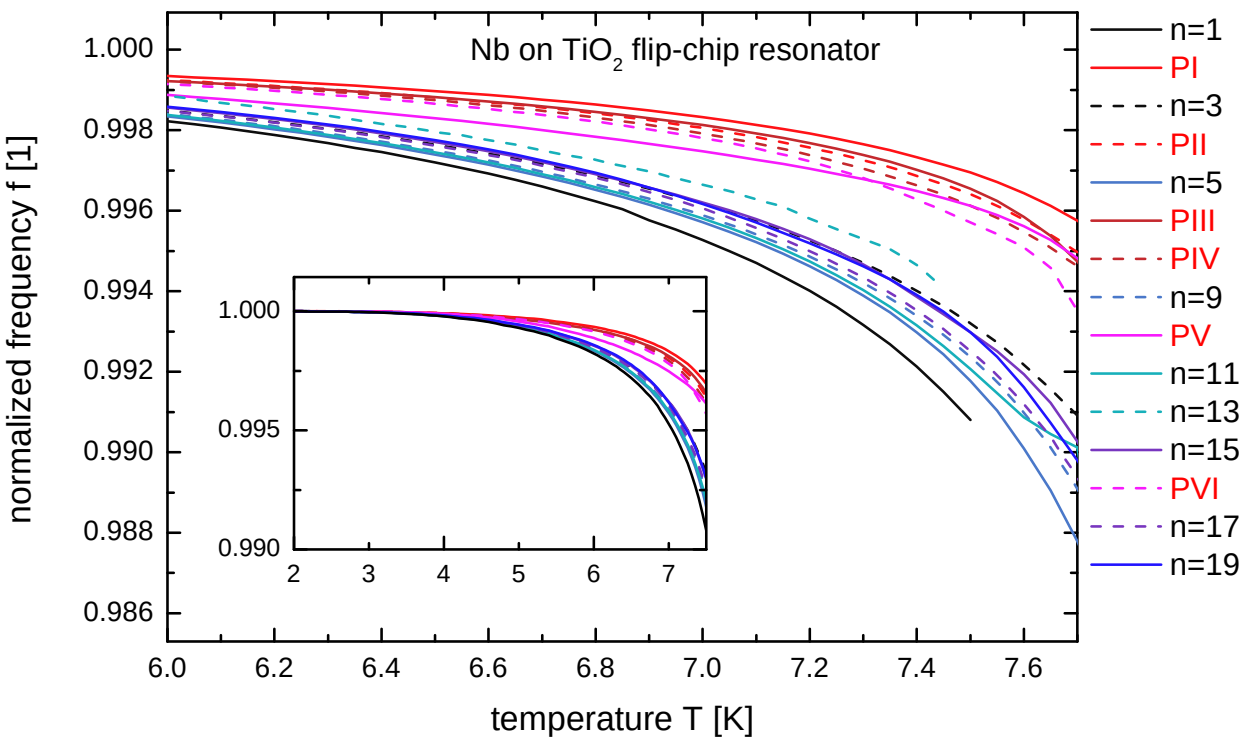

Fig. 4.5: Measured resonance frequency f in dependence of the temperature T for the TiO_2 flip-chip setup for the resonator modes measured in figure 4.4. The frequency is normalized to $f(T = 2\,\mathrm{K})$.

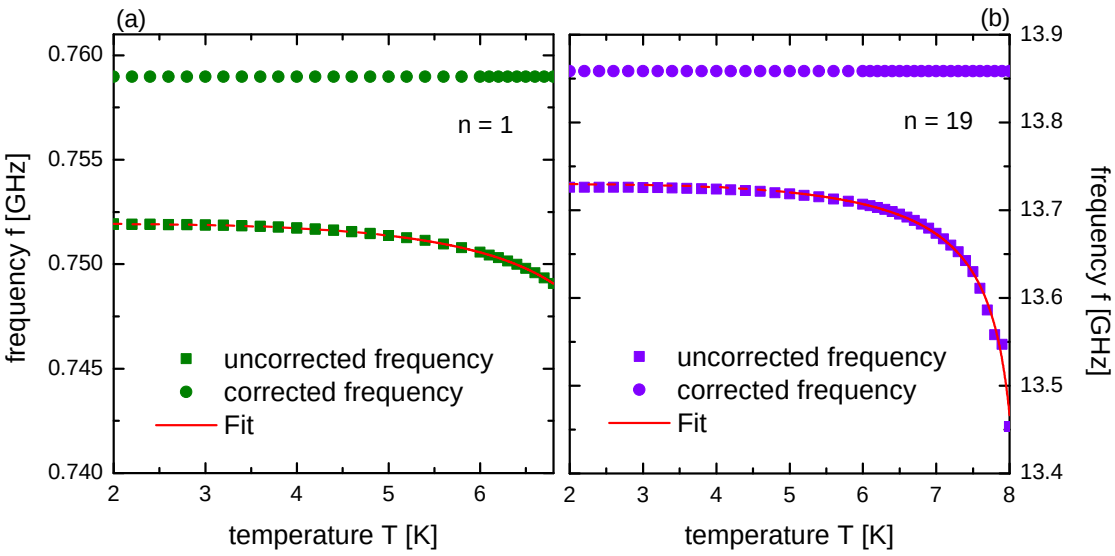

Fig. 4.6: Frequency f of the $n = 1$ and $n = 19$ mode in dependence of the temperature T and fitted with equation (4.16), in addition the corrected resonance frequency is shown.

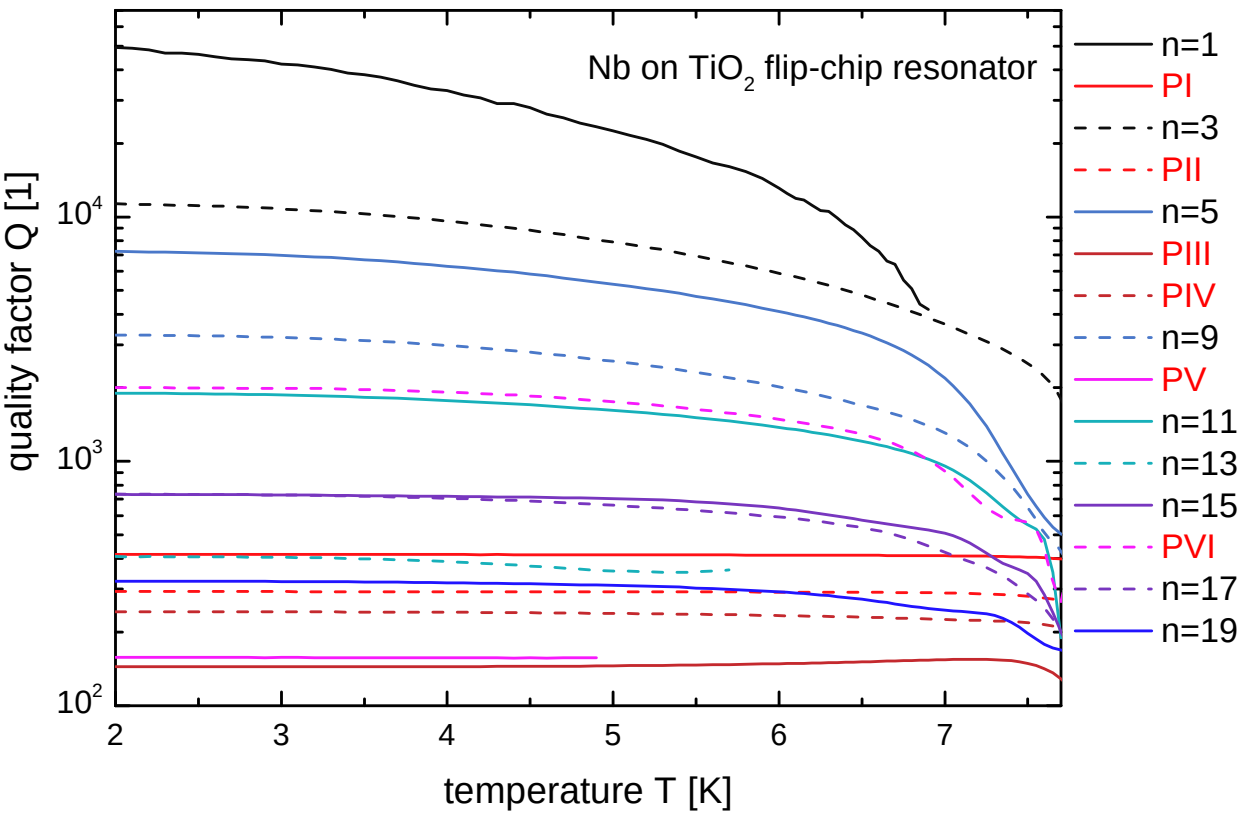

Fig. 4.7: Measured quality factor Q in dependence of the temperature T in logarithmic scale for the TiO_2 flip-chip setup for the resonator modes measured in figure 4.4.

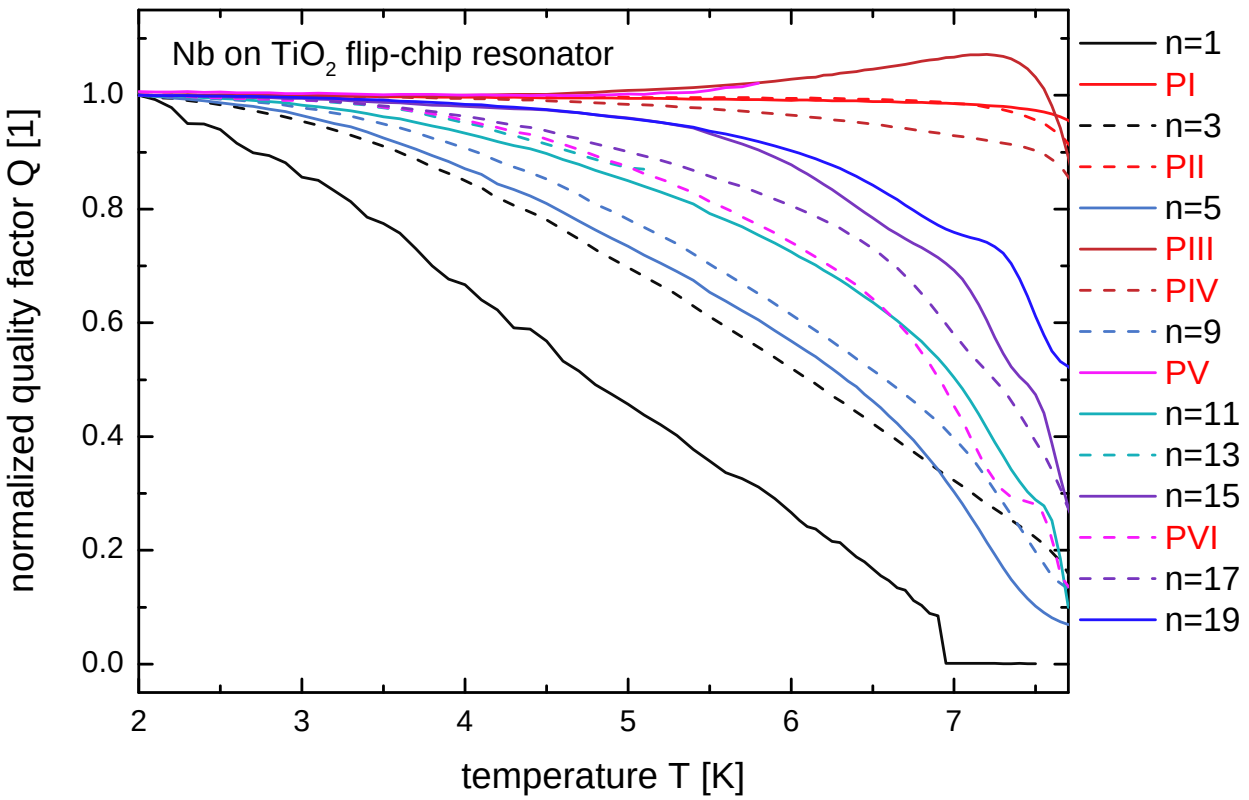

Fig. 4.8: Measured normalized quality factor Q in dependence of the temperature T for the TiO_2 flip-chip setup for the resonator modes measured in figure 4.4. The quality factor is normalized to $Q(T = 2\,\mathrm{K})$.

frequency f of the resonator modes in figure 4.5 is shown for the $n = 1$ and $n = 19$ mode in figure 4.6. The corrected resonance frequencies of the resonator modes are listed in table 4.1. The decrease of $f(T)$ results from the increasing London penetration depth λ_L according to equation (2.6) that decreases the width of the outer and inner conductor [37] of the coplanar waveguide resulting in a increased impedance Z [29]. According to equation (2.33) the frequency f

$$v_{\mathrm{ph}} = \frac{\lambda f}{\sqrt{\epsilon_{\mathrm{eff}}}} = \frac{1}{ZC_{\mathrm{CPW}}} \tag{4.17}$$

shifts to lower values for an increasing impedance Z as it is observed. The phase velocity v_{ph} is defined as $v_{\mathrm{ph}} = \frac{\lambda f}{\sqrt{\epsilon_{\mathrm{eff}}}}$.
Resonator modes and parasitic modes form respectively bundles that fall of towards T_c. The dependence of the resonance frequency f of the parasitic modes on T confirms that the parasitic modes are affected by the superconducting layer on the flip-chip as it is already expected because the parasitic modes as well as the resonator modes vanish for $T > T_c$. However the formation of bundles indicates that the parasitic modes are differently distributed in the superconducting layer compared to the resonator modes. The delayed decrease of f in dependence of T in case of the parasitic modes can be explained when assuming that the parasitic modes form a standing wave over the whole TiO_2 bulk that is bounded on one side by the superconducting layer as it would be the case for a cavity mode. The penetration depth λ_L alters the shape of the whole superconducting chip not only by effectively decreasing the thickness t of the chip but also it's width with total side lengths $s = 5\,\mathrm{mm}$ and the resonator dimensions with inner width $S = 120\,\mu\mathrm{m}$ and gap $W = 50\,\mu\mathrm{m}$. But when comparing the effects of a total side length with $s = 5\,\mathrm{mm}$ decreased by λ_L on the parasitic modes to the effects of the effectively altered inner width $S = 120\,\mu\mathrm{m}$ and gap $W = 50\,\mu\mathrm{m}$ of the resonator on the resonator modes, it can be seen that the relative alteration of the geometry is stronger for the resonator modes that are located along the resonator in contrast to the parasitic modes where it is assumed that they form a cavity mode and are therefore affected by the whole superconducting layer. This results in a relatively weaker increase of the impedance Z that explains the delayed decrease of the resonance frequency f in the case of parasitic modes.
The quality factor Q is depicted in figure 4.7 in logarithmic scale and for a better observation

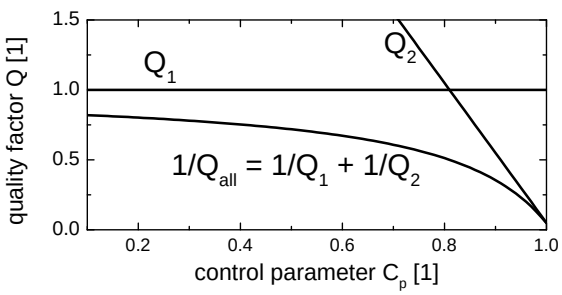

Fig. 4.9: Constant quality factor Q_1 and a linear decreasing quality factor Q_2 in dependence of a control parameter C_p and the resulting quality factor $\frac{1}{Q_{\mathrm{all}}} = \frac{1}{Q_1} + \frac{1}{Q_2}$.

of the T-dependence normalized to $Q(T = 2\,\mathrm{K})$ in figure 4.8. The quality factor Q of all modes with the exception of the PIII-mode decrease for higher temperatures T. The resonator modes tend to decrease stronger than the parasitic modes. When investigating the resonator modes, the relative decrease as seen in figure 4.8 tends to be weaker for higher resonator modes n. In general as seen in figure 4.7 the resonator modes show for higher n a smaller quality factor Q. The parasitic modes show only a small decrease or are widely constant.
The lower quality factor Q for higher resonator modes n is a common feature that is often observed when investigating resonances in the superconducting regime. Within the LRC-circuit model the resonance frequency can be calculated where the inductance L changes for higher frequencies [2] according to equation (2.15)

$$\omega_0^n = n\omega_0^{n=1} = \frac{1}{\sqrt{(L_{\mathrm{res}} + L_{\mathrm{coup}})C_{\mathrm{res}}}} \tag{4.18}$$

for odd n. It has to be noted that the LRC-circuit model simplifies the analysis of the resonator, but the quantities L_{res}, L_{coup} and C_{res} are not the real inductances and capacitance one would obtain by considering the geometry and physical properties of the waveguide. But L_{coup}, L_{res} and C_{res} can be linked to the real inductances L_l and capacitance C_l by calculating the resonant behaviour of a short-circuited $\frac{\lambda}{4}$-resonator [20]. This was done by Göppl [2] for an open $\frac{\lambda}{2}$-resonator, in the case of a $\frac{\lambda}{4}$-resonator the same approach yields for the investigated capacitance and inductances

$$L_{\mathrm{coup}} + L_{\mathrm{res}} = \frac{8l}{\pi^2 n^2} L_l \tag{4.19}$$

$$C_{\mathrm{res}} = \frac{l}{2} C_l \tag{4.20}$$

where l is the total length of the resonator. It can be seen that $L_{\mathrm{coup}} + L_{\mathrm{res}}$ depends on n which is no surprise because the basic LRC-circuit model only takes into account one resonance frequency where the calculation of the resonances frequencies ω_0^n of a short-circuited $\frac{\lambda}{4}$ resonator exhibit n odd multiples of the fundamental mode.
This motivates to replace $L^* = n^2(L_{\mathrm{res}} + L_{\mathrm{coup}})$ with a new inductance L^* that does not depend on n. This way the quality factor $Q(n)$ can be given with equation (2.14) in dependence on n

$$Q(n) = \sqrt{\frac{L_{\mathrm{res}} + L_{\mathrm{coup}}}{C_{\mathrm{res}}}} \cdot \frac{1}{R} = \sqrt{\frac{L^*}{C_{\mathrm{res}}}} \cdot \frac{1}{nR} = \frac{Q(n=1)}{n}. \tag{4.21}$$

This approach is only valid for overcoupled resonators $g > 1$. As it can be seen in figure 4.4 the absorption loss of the resonator modes increases with higher frequency resulting in a increased coupling coefficient [20]

$$g = \frac{S_{21}^{\mathrm{background}}(f) - S_{21}^{\mathrm{resonance}}(f)}{S_{21}^{\mathrm{resonance}}(f)} \tag{4.22}$$

for higher modes. The decrease of the quality factor $Q \propto \frac{1}{n}$ was already measured and evaluated [38][39][40]. The decrease of Q of the resonator modes can be understood when the quality factor is split into two parts Q_1 and Q_2 according to equation (2.16). It is assumed that the quality factor of the resonator modes consists of a T-independent Q_1 and a decreasing $Q_2(T)$ in dependence of T. A schematic representation of the effects of Q_1 and $Q_2(T)$ on Q in case of a linearly decreasing $Q_2(C_p)$ can be seen in figure 4.9. It can be seen that the behaviour of the quality factor Q is dominated by Q_1 for small C_p and by Q_2 for greater C_p. This corresponds to equation (2.16), Q is dominated by the behaviour of Q_1 for $Q_1 < Q_2$ and vice versa. This explains the stronger decrease of Q for lower n as the quality factor $Q(T = 2\,)K$ is greater for lower n as seen in figure 4.8. When the parasitic modes in figure 4.7 are investigated it can be seen that these show a weaker decrease and eventually intersect with the resonator modes. When splitting Q also in Q_1 and $Q_2(T)$ for the parasitic modes it can be concluded that the parasitic modes show a weaker decrease in $Q_2(T)$, otherwise the resonator modes and parasitic modes with comparable quality factor Q would not intersect. The T-dependence of the partial quality factor $Q_2(T)$ is caused by the superconducting layer. For higher T an increase of normal conducting charge carrier occurs that results in a decrease of the quality factor that is modelled by $Q_2(T)$. Q_1 is a measured parameter that depends on the already present losses in the microwave resonator. The resonator modes are bounded by an open and closed end with the superconducting layer that prevents high losses on the border resulting in a high quality factor. The parasitic modes however are distributed over the whole superconducting flip-chip. The standing waves in the flip-chip could dissipate and be reflected at the walls of the resonator box that would result in higher losses and therefore in a lower quality factor. The parasitic and resonator modes show a different behaviour of $Q_2(T)$. This is also the result of the London penetration depth λ_L that decreases the superconducting volume of the resonator relatively stronger than of the whole chip. This results in a weaker dependence of $Q_2(T)$ on the temperature in case of the parasitic modes. When measuring resonances towards the critical temperature T_c of niobium the influence of the standing waves of the background becomes stronger. The frequencies also shift over the standing waves resulting in a slightly alternating quality factor Q because the standing waves add up with the resonance signal. The effect of alternating Q becomes stronger for higher modes as Q becomes weaker and the shifting is stronger for higher f. The alternating Q can be seen for the $n = 11$, $n = 15$, $n = 17$ and $n = 19$ mode. The PIII-mode shifts slightly over a standing wave, resulting in higher Q. This effect is mainly observed for resonances with low Q as the higher n modes and the PIII-mode
The quality factor of the PVI mode behaves like the resonator modes whereas the resonance frequency f shifts like the parasitic modes. This shows that it is necessary to divide the parasitic modes further as they may not share the same origin.

4.2.4 B-field dependence of TiO_2 modes

Similar to the temperature dependence of the resonator modes, it is expected that no effects due to the magnetic permeability of TiO_2 occur as these are negligibly small [41]. B-field dependent effects are expected to be caused by the superconducting layer which were already observed for Pb stripline resonators [8] and Nb stripline resonators [42] as well as in coplanar

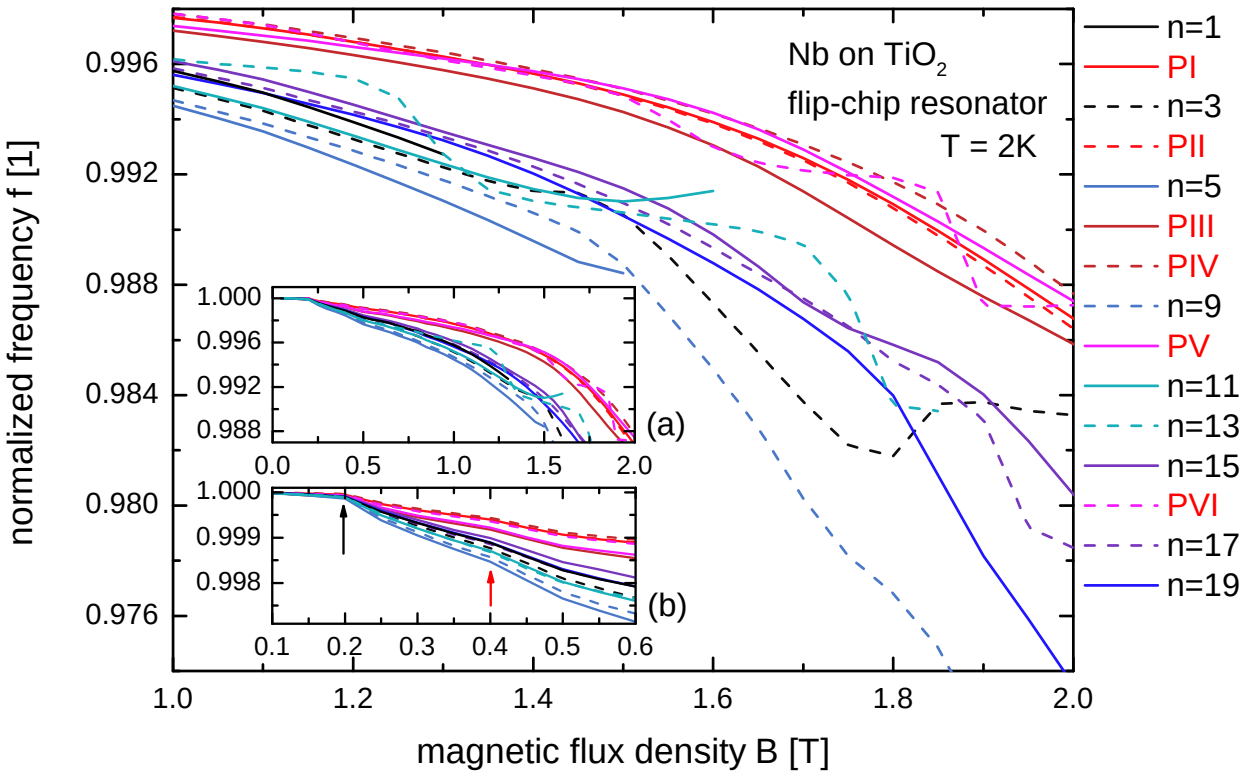

Fig. 4.10: Measured resonance frequency f normalized to the data at $B = 0\,\mathrm{T}$ for the TiO_2 flip-chip setup with the resonator modes measured in figure 4.4. Inset (a) shows f for the whole range $0\,\mathrm{T} < B < 2\,\mathrm{T}$ and inset (b) shows f for $0.1\,\mathrm{T} < B < 0.6\,\mathrm{T}$. The black arrow marks the starting point of decrease of f at $B \approx 0.2\,\mathrm{T}$ and the red arrow marks an abrupt change in decrease of f at $B \approx 0.4\,\mathrm{T}$. The fluctuations for $B > 1\,\mathrm{T}$ are due to the decrease of the quality factor $Q(B)$ in dependence of B that result in a stronger disturbance of the resonator modes as the resonator modes shift in their frequencies over the standing waves of the background.

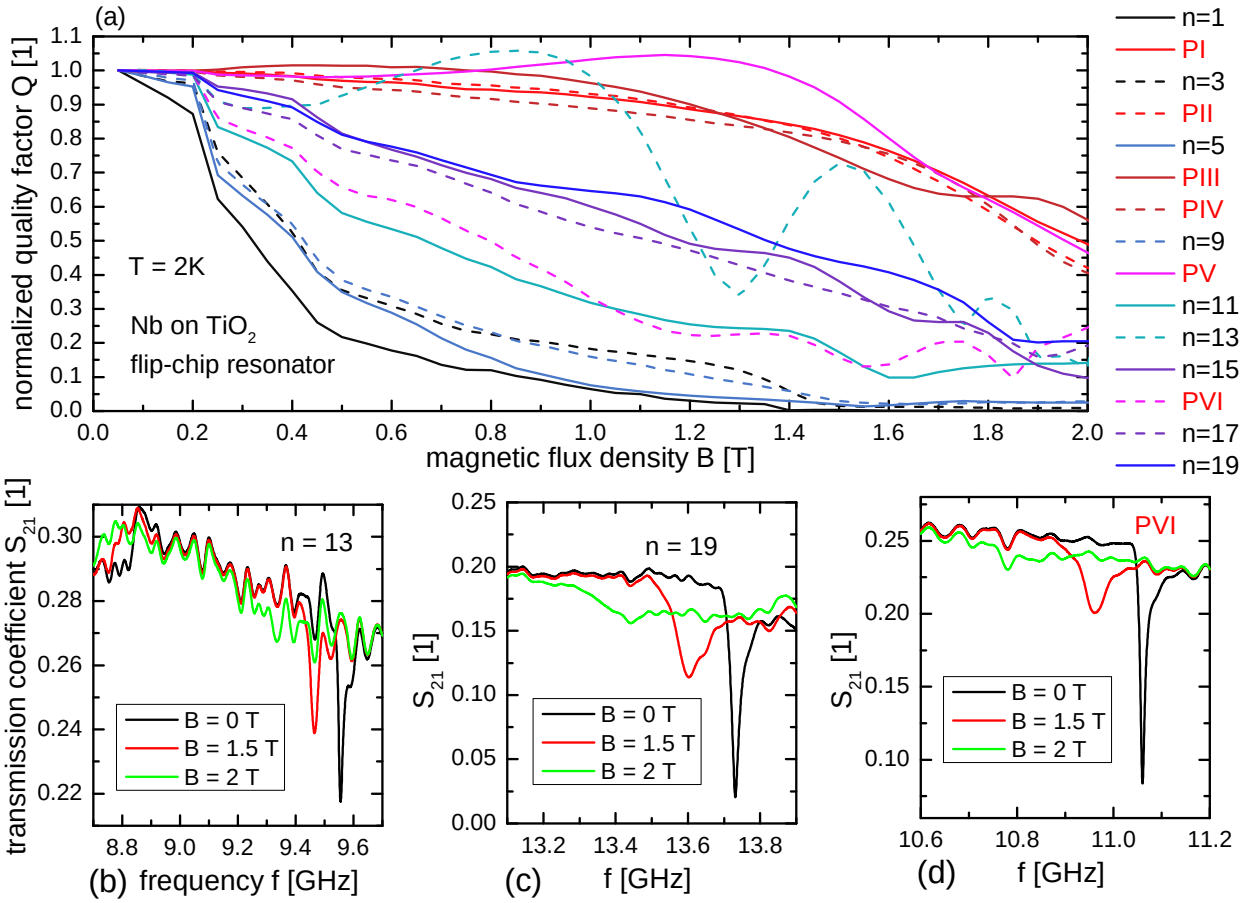

Fig. 4.11: Figure (a) shows the measured quality factor Q normalized to the data at $B = 0\,\mathrm{T}$ for the TiO_2 flip-chip setup with the resonator modes measured in figure 4.4. The fluctuating quality factor Q is a result of the decrease of f in dependence of B, the resonator modes shift over the standing waves of the background resulting in a varying Q. In (b), (c) and (d) the transmission signal for three modes can be seen at different B-fields.

waveguides [43]. The resonance frequency f and quality factor Q of the resonator and parasitic modes were measured for $0\,\mathrm{T} < B < 2\,\mathrm{T}$.
In figure 4.10 the resonance frequency f and in figure 4.11 in (a) the quality factor Q can be observed in dependence of the magnetic flux density B. The data is normalized to the measured values at $B = 0\,\mathrm{T}$. In both figures 4.10 and 4.11 it can be seen that f and Q decrease with increasing B. For a few modes, f and Q fluctuate in dependence of B for high B, this is a result of the shifting resonance frequency f as well as the decreasing quality factor Q that increases the disturbing influences of the standing waves for a higher magnetic flux density B as well as higher modes n. This effect can be seen in figure 4.11 in (b), (c) and (d). Similar to the observations that were made for the temperature sweep, the resonance frequencies f of the resonator modes and the parasitic modes respectively form bundles indicating that their distribution on the superconducting Nb-layer differs.
Here the magnetic field is orientated parallel to the flip-chip. In measurements with a perpendicular orientation of the magnetic field to the superconducting Nb-film, coplanar resonators already show for $B > 0.5\,\mathrm{mT}$ a strong decrease of the quality factor Q [43]. For a parallel magnetic field Q decreases for $B > 0.2\,\mathrm{T}$ as it can be seen in figure 4.11 in (a). The higher magnetic flux density B that is necessary to disturb the resonances is a result of the geometry. In the parallel case the Nb-film can more effectively repel an external magnetic flux density than in the perpendicular case. In figure 4.10 it can be seen that the resonance frequency f does not shift for $B < 0.2\,\mathrm{T}$. This is also the result of the displacement of the magnetic flux density B.
For $B > 0.2\,\mathrm{T}$ the quality factor of the resonator modes heavily decreases. The decrease is stronger for lower n. The initial quality factor $Q(B = 0\,\mathrm{T})$ of the resonator modes n decreases for higher harmonics as it was shown in equation (4.21). When assuming that the influence of the magnetic flux density B on the resonances can be modelled by a disturbing additional quality factor Q_B that is approximately the same for all resonator modes, the weaker decrease of the quality factor Q in dependence of Q for higher n can be explained with equation (2.16)

$$\frac{1}{Q} = \frac{1}{Q(B = 0\,\mathrm{T})} + \frac{1}{Q_\mathrm{B}(B)}. \tag{4.23}$$

For lowered $Q(B = 0\,\mathrm{T})$ the disturbance caused by the magnetic flux density Q_B is reduced. The decrease of the quality factor of the resonator modes can be explained with the formation of vortices. The formation of vortices lowers the quality factor Q over a broad range of B as the vortices continually rise in density. However the quality factor Q of the parasitic modes with the exception of the PVI mode is almost unaffected, again indicating a different distribution of the parasitic modes as a different loss mechanism is present. The PVI mode shows a quality factor Q that behaves similar to the quality factors of the resonator modes but a resonance frequency f that falls off like the resonance frequencies of the parasitic modes. This observation is consistent with the temperature-dependent behaviour of the PVI mode.
The resonance frequency f in the dependence of the magnetic flux density B can be seen in figure 4.10. Inset (a) shows the B-dependence over the whole range of $0\,\mathrm{T} < B < 2\,\mathrm{T}$ and inset (b) shows the dependence for $0\,\mathrm{T} < B < 0.6\,\mathrm{T}$. For $B > 0.2\,\mathrm{T}$ the resonance frequency decreases towards $B = 2\,\mathrm{T}$ for both resonator and parasitic modes. This is also the result

of the formation of vortices as the decrease of the resonance frequency f and of the quality factor Q start for the same magnetic flux density $B > 0.2\,\mathrm{T}$ when investigating the resonator modes. The effects of the formation of vortices that occur inside the superconducting plane can be modelled with the kinetic inductance L_{kin}. The kinetic inductance L_{kin} takes the inertia of the charge carriers into account. It can be shown that the kinetic inductance scales with the London penetration depth $L_{\mathrm{kin}} \propto \lambda_L^2$ [2]. Because the formation of vortices involves the excitation of normal conducting quasi-particles, the density of superconducting charge carriers n_s decreases which results in an increasing λ_L according to equation (2.5). This means that L_{kin} increases for greater B-fields. When $L_{\mathrm{coup}} + L_{\mathrm{res}} = L_{\mathrm{m}} + L_{\mathrm{kin}}$ is replaced, the following expression for the resonance frequency can be obtained with equation (2.15)

$$\omega = 2\pi f = \frac{1}{\sqrt{C \cdot (L_{\mathrm{kin}} + L_{\mathrm{m}})}} \tag{4.24}$$

where L_{m} is the magnetic inductance due to the geometry of the resonator. It can be seen that for greater L_{kin} the resonance frequency f decreases.
However it seems remarkable that the decrease of the resonance frequency f of the parasitic modes is of a similar order of the resonator modes, but the quality factor is not. It could be speculated that additional losses occur with an increasing magnetic flux density that have a greater impact on the effective geometry than the formation of vortices. The formation of vortices takes place in the superconducting layer itself, which does not necessarily change the effective geometry. Additional losses that increase the London penetration depth λ_L with increasing B however could more directly impact the geometry. Inset (b) in figure 4.10 shows a red arrow where a change in decrease of the resonance frequency can be seen. This could indicate a change of the loss mechanism in the superconducting layer.

4.2.5 ESR-measurements with TiO_2

mode	f [GHz]	$B_{\mathrm{ext}}^{\mathrm{calc.}}$ [mT]	$B_{\mathrm{ext}}^{\mathrm{meas.}}$ [mT]	mode	f [GHz]	$B_{\mathrm{ext}}^{\mathrm{calc.}}$ [mT]	$B_{\mathrm{ext}}^{\mathrm{meas.}}$ [mT]
$n = 1$	0.75	26.8	26.0	PV	7.44	265.5	259.8
PI	1.76	62.8	61.2	$n = 11$	7.99	285.1	278.6
$n = 3$	2.21	78.9	76.6	$n = 13$	9.55	340.8	333.4
PII	3.16	112.8	109.6	$n = 15$	11.06	394.7	386.5
$n = 5$	3.62	129.2	125.9	PVI	11.62	414.6	406.7
PIII	4.86	173.4	169.1	$n = 17$	12.38	441.8	432.9
PIV	6.21	221.6	216.5	$n = 19$	13.73	489.9	480.6
$n = 9$	6.53	233.0	227.5				

Tab. 4.3: $B_{\mathrm{ext}}^{\mathrm{calc.}}$ for the frequency f of the resonator modes and parasitic modes according to equation (4.26). $B_{\mathrm{ext}}^{\mathrm{meas}}$ is the measured magnetic flux density as it can be seen in figure 4.12. At B_{ext} energy transmission between two electron states is stimulated which results in a sharp decrease of the quality factor Q.

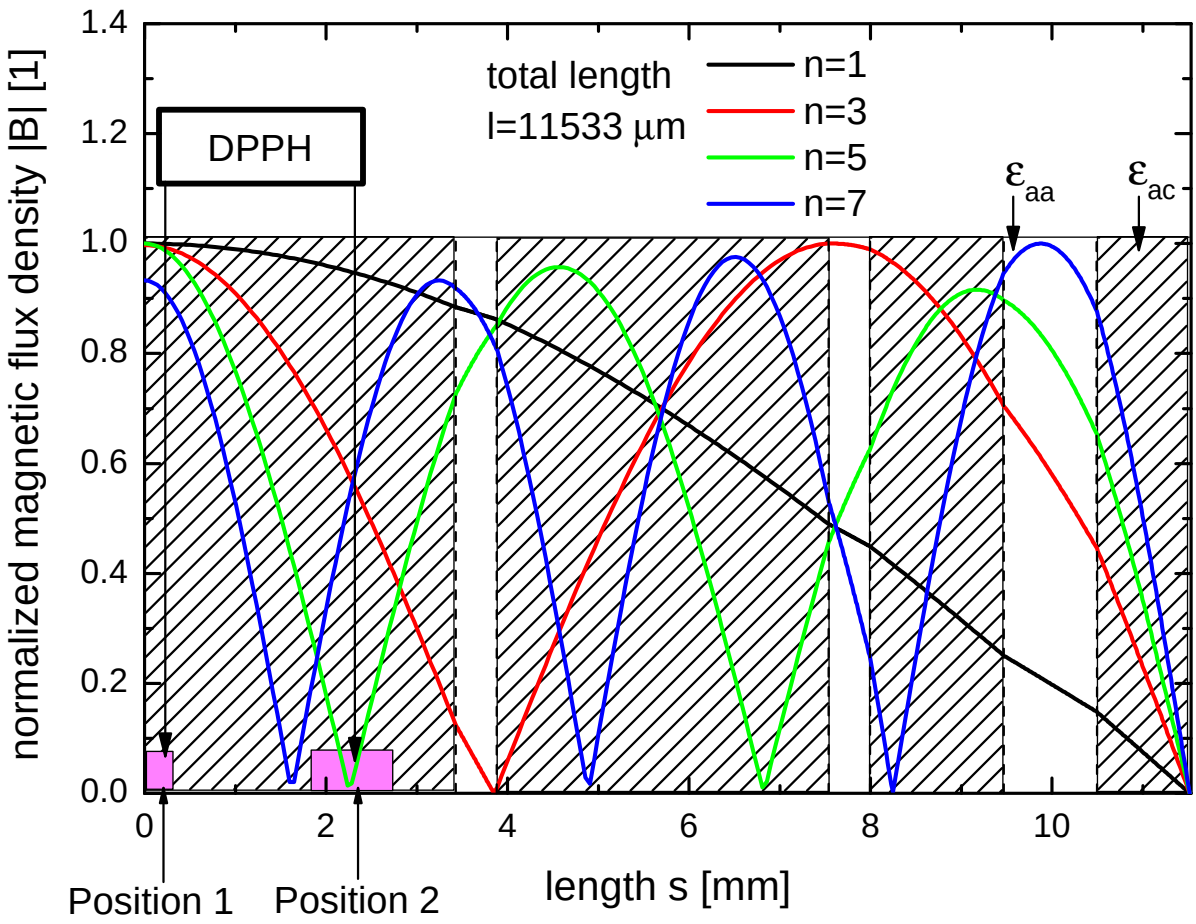

Fig. 4.12: Schematic representation of the distribution of the magnetic flux density $|B|$ on the whole resonator. The resonator is divided into sections with dielectric constants ϵ_{aa} and ϵ_{ac}. A DPPH sample is placed on two different positions 1 and 2.

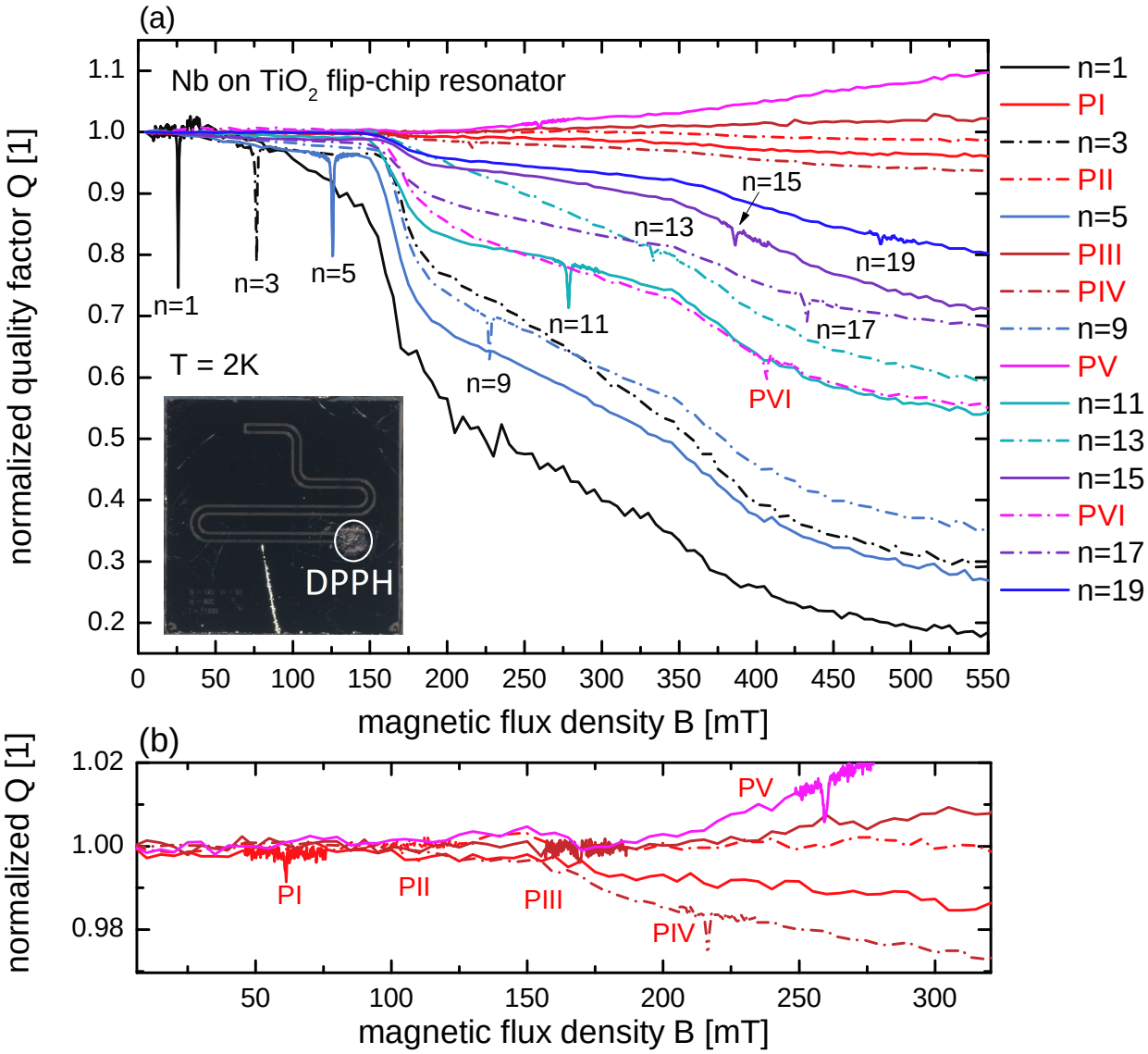

Fig. 4.13: (a) shows the normalized quality factor Q of the resonator modes and parasitic modes of the TiO_2 flip-chip resonator at $T = 2\,\mathrm{K}$ in dependence of B. Q is normalized to $B = 0\,\mathrm{T}$. The DPPH sample is placed at position 1 at the open end as shown in the inset. (b) shows the parasitic modes from (a) in a close-up view.

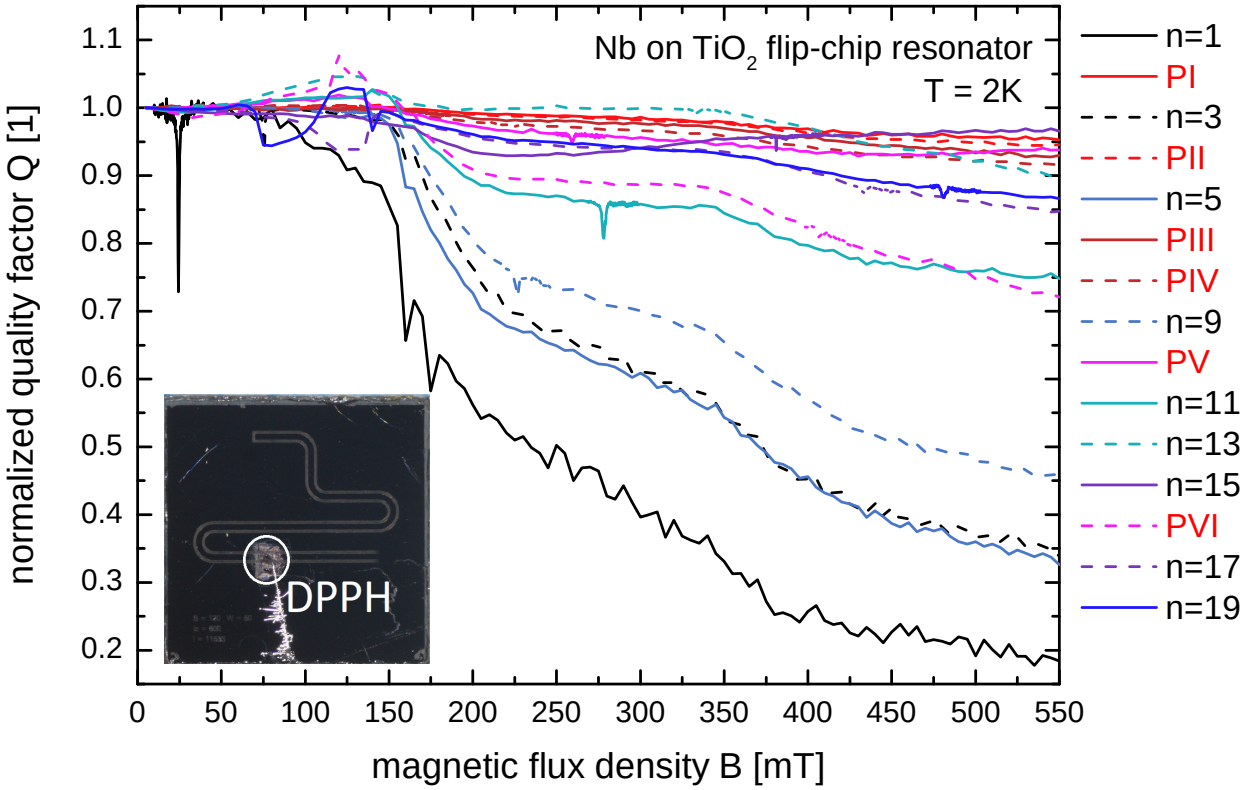

Fig. 4.14: Normalized quality factor Q of the resonator modes and parasitic modes of the TiO_2 flip-chip resonator at $T = 2\,\mathrm{K}$ in dependence of B. Q is normalized to $B = 0\,\mathrm{T}$. The DPPH sample is placed at position 2 as shown in the inset.

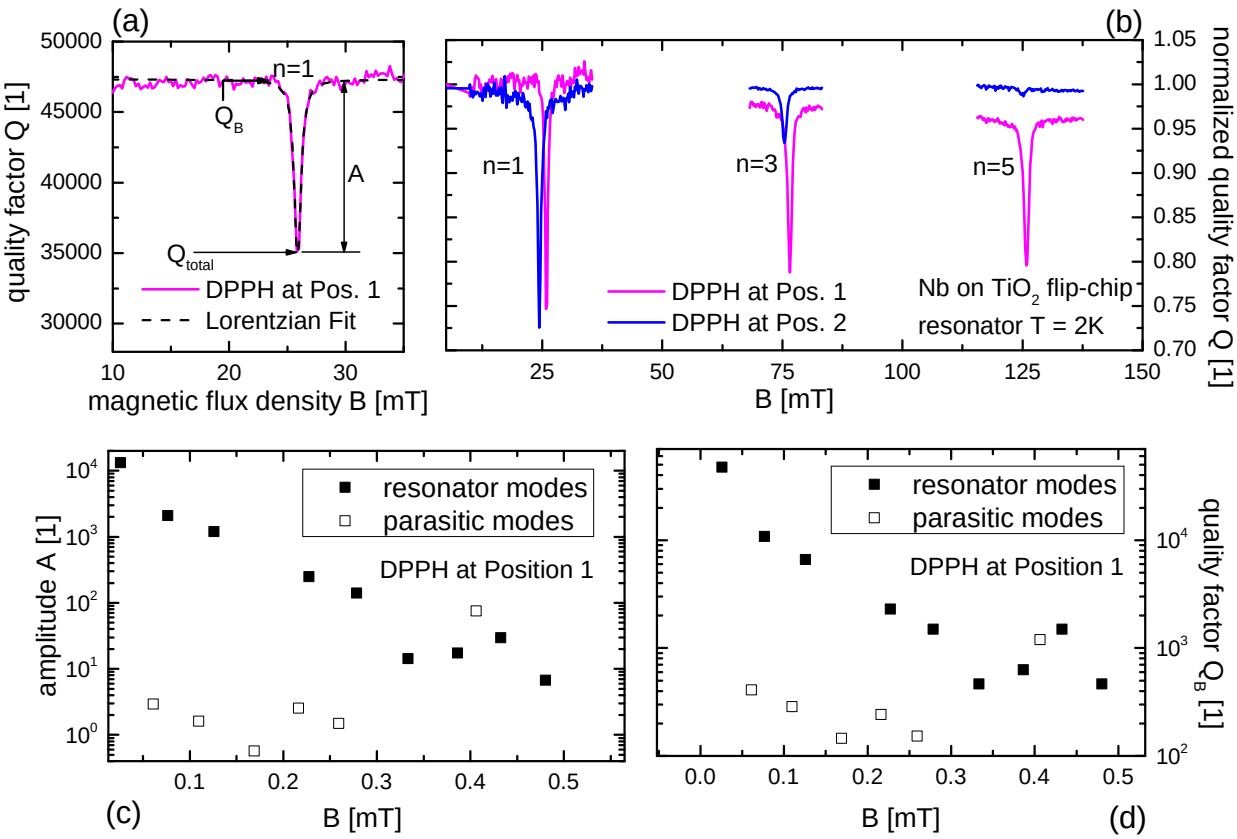

Fig. 4.15: Figure (a) shows the measured quality factor Q for the $n = 1$ mode for DPPH at position 1, Q_B is the quality factor that is not influenced by DPPH, Q_total accounts for the losses caused by DPPH and amplitude $A = Q_\mathrm{B} - Q_\mathrm{total}$ is the difference between both quantities. Q_B and A can be extracted by using a Lorentzian Fit. Figure (b) shows the measured normalized quality factor Q for the $n = 1$, $n = 3$ and $n = 5$ mode for DPPH at both positions 1 and 2. Figure (c) shows the amplitude A for resonator modes and parasitic modes. Figure (d) shows Q_B for resonator modes and parasitic modes.

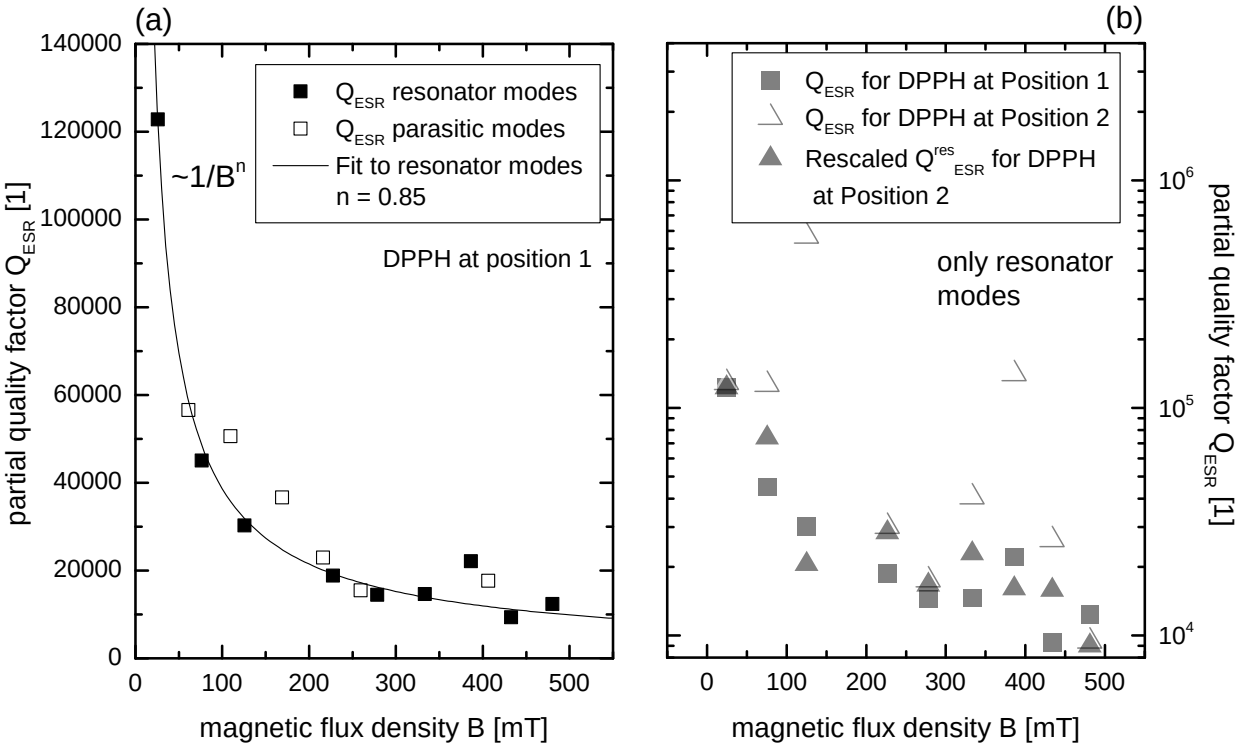

Fig. 4.16: Figure (a) shows the obtained Q_{ESR} for resonator and parasitic modes and fitted to $Q_{\mathrm{ESR}} \propto \frac{1}{B^n}$ with $n = 0.85$ for the resonator modes. Figure (b) shows the obtained Q_{ESR} for DPPH at both positions and a rescaled $Q_{\mathrm{ESR}}^{\mathrm{res}}$ that can be obtained when scaling Q_{ESR} according to the distribution of the B-field as in figure 4.12.

ESR is an abbreviation for Electron Spin Resonance. ESR measurements use the Zeeman effect as basis. According to the Zeeman effect an energy difference ΔE between two electron states with opposite spins occurs in a magnetic field

$$\Delta E = g\mu_B B_{\text{ext}} \tag{4.25}$$

where $g = 2.0023$ is the g-factor, $\mu_B = 9.274 \cdot 10^{-24} \frac{\text{J}}{\text{T}}$ the Bohr magneton [44] and B_{ext} is the external magnetic flux density. A widely used substance for the detection of ESR-signals is 1,1-diphenyl-2-picryl-hydrazyl or abbreviated DPPH [45]. When DPPH is placed on the flip-chip waveguide before the mounting process and cooling is executed, an ESR-signal can be observed in the spectrum. For standing waves in the resonator with resonance frequencies f, energy transmission $E = hf$ is stimulated when the condition

$$f = \frac{g\mu_B}{h} B_{\text{ext}} = 28.025 \, \frac{\text{GHz}}{\text{T}} B_{\text{ext}} \tag{4.26}$$

is met. Here $h = 6.626 \cdot 10^{-34}$Js is Planck's constant. In this case the spins of the electrons are flipped. When the quality factor Q of a resonator mode with resonance frequency f is observed in dependence of an external magnetic flux density B_{ext}, a sharp decrease of Q at $B_{\text{ext}} = \frac{hf}{g\mu_B}$ can be seen. The according calculated values of B_{ext} for the frequency f of the modes can be seen in table 4.3. The decrease strongly depends on the intensity of the standing wave in the resonator and therefore on the distribution of the B-field component of the standing wave in the resonator.
Similar ESR measurements where DPPH was deposited on a metallic capacitively coupled coplanar resonator [46] or on a metallic coplanar feedline [47] were already performed. Miksch showed that ESR-measurements are a suitable tool to investigate the electron energy levels of samples, one of his investigated samples was ruby [47]. Javaheri's work showed that the effects of DPPH can be observed when a capacitively coupled copper resonator with an approximate quality factor of $Q \approx 200$ is used [46]. This motivates to use DPPH also for the superconducting flip-chip resonator.
The distribution of the magnetic flux density B of the resonator modes in the resonator is schematically depicted in figure 4.12 for the fundamental mode and 3 higher harmonic modes of the resonator. Note that the anisotropic ϵ of titanium dioxide has to be considered when calculating the distribution of B. Two positions were chosen for the DPPH sample. Position 1 was chosen because all standing waves show a maximal B-component and should therefore show a clearly visible ESR-signal. This is important to evaluate the effects of the DPPH sample on the quality factor. Position 2 was chosen because the $n = 5$ mode shows a minimum in this regime that should result in a minimal ESR-signal in the quality factor of the $n = 5$ mode. The goal of this method is to use DPPH as a fingerprint method to identify the resonator modes and to distinguish them from the parasitic modes.
Figure 4.13 and 4.14 show the normalized quality factor Q of the resonator modes and parasitic modes in dependence of the magnetic flux density B for different positions of the DPPH sample. In figure 4.13 the ESR-signal for DPPH at position 1 can be seen for all resonator modes and weakly for all parasitic modes. The according B_{ext}-fields where the ESR-signal occurs are also listed in table 4.3. The calculated and measured data differ slightly

because the solenoid that ensures B_{ext} is not perfectly calibrated. The ESR-signal can be observed for all modes. In figure 4.14 the ESR-signal for DPPH at position 2 is weaker for most of the modes. In figure 4.15 in (b) the $n = 1$, $n = 3$ and $n = 5$ can be seen for DPPH at Position 1 and 2. When comparing the ESR-signal for different positions and considering the expected magnetic flux density B that can be seen in figure 4.12 at the respective points for the $n = 1, 3, 5$ modes, it can be seen that at the new position the ESR-signal of the $n = 5$ mode is much weaker and that the ESR-signal of the $n = 3$ mode is also weaker. The $n = 1$ mode is roughly the same, the slight increase can be explained with a higher amount of DPPH that was deposited on position 2 than on position 1. Also it can be seen that the modes slightly shifted to lower B-fields for the new position, this is a result of the not perfectly calibrated solenoid coil.
DPPH increases the losses in the waveguide when the condition formulated in equation (4.26) is met. The B-field dependent quality factor Q_{B} of the resonator is decreased to Q_{total} when the effects of DPPH become present, this can be seen in figure 4.15 in (a) where the quantities Q_{B}, Q_{total} and amplitude A are given. Here the amplitude

$$A = Q_{\text{B}} - Q_{\text{total}} \tag{4.27}$$

would be a natural choice to account for the losses due to the DPPH sample. Amplitude A can be extracted from the quality factors Q as they can be seen in figure 4.13 and 4.14 by fitting with a Lorentzian

$$Q^{\text{fit}}(B_{\text{ext}}) = Q_{\text{B}} - A \frac{\left(\frac{B_{\text{BW}}}{2}\right)^2}{(B_{\text{ext}} - B_{\text{ext}}^{\text{meas.}})^2 + \left(\frac{B_{\text{BW}}}{2}\right)^2}. \tag{4.28}$$

where B_{BW} is the B-width of the Lorentzian, which shows a minimum at $B_{\text{ext}}^{\text{meas}}$. An exemplary Lorentzian fit can be seen in figure 4.15 in (a) for the $n = 1$ mode, the obtained measured $B_{\text{ext}}^{\text{meas}}$ are listed in table 4.3.
The obtained amplitude A and quality factors Q_{B} can be seen in figure 4.15 in (c) and (d). Q_{B} is lower for higher modes of the resonator and Q_{B} is in general lower in the case of parasitic modes. The amplitude A strongly resembles the behaviour of Q_{B} which is surprising because Q_{B} is not affected by the ESR-signal where A actually is affected. So it has to be assumed that the amplitude A also depends on Q_{B}. In fact the losses due to DPPH are modelled as additional resistance in the LRC-circuit and summed which results in a total lowered quality factor according to equation (2.16)

$$\frac{1}{Q_{\text{total}}} = \frac{1}{Q_{\text{B}}} + \frac{1}{Q_{\text{ESR}}}. \tag{4.29}$$

Q_{ESR} accounts for the losses caused by the DPPH sample where it is important to note that Q_{ESR} is calculated at a set magnetic flux density B_{ext}. When observing the ESR-signal in figure 4.13 and 4.14 it could be assumed that the greater amplitude A for the resonator modes accounts for a greater magnetic field density B of the modes in comparison to the parasitic modes where A is barely visible. However, the amplitude A does not directly represent losses

due to DPPH, although it would be a natural choice. The previous considerations for A were done in order to show it's similar behaviour to Q_{B}. It is important to note that A is a misleading quantity which is the reason why it was discussed more detailed.
Q_{ESR} can be calculated with equation (4.29) and (4.27) to

$$Q_{\mathrm{ESR}} = \frac{Q_{\mathrm{B}}(Q_{\mathrm{B}} - A)}{A}. \tag{4.30}$$

where A and Q_{B} are obtained through a Lorentzian Fit (4.28). For DPPH at position 1 Q_{ESR} can be seen in figure 4.16 in (a). A decrease of Q_{ESR} can be seen for both resonator and parasitic modes. This means that parasitic modes exhibit a B-field component at the open end of the resonator. As Q_{ESR} has a similar order of magnitude for both parasitic modes and resonator modes, the B-field component also has a similar order of magnitude for both parasitic modes and resonator modes. As a consequence, it seems likely that the parasitic modes are not distributed on the whole superconducting layer but form an additional localized mode on the resonator. It should be mentioned that this result does not contradict the smaller influence of the DPPH sample on the quality factor of the parasitic modes as the quality factor of the parasitic modes is in general lowered when compared to the resonator modes. Furthermore Q_{ESR} of the resonator modes is fitted with

$$Q_{\mathrm{ESR}} \propto \frac{1}{B^n} \tag{4.31}$$

which yields $n = 0.85$. The decrease of Q_{ESR} corresponds to an increase of losses that is the result of a greater energy difference ΔE as it is proportional to the magnetic flux density $\Delta E \propto B_{\mathrm{ext}}$.
In (b) in figure 4.16 Q_{ESR} of the resonator modes is depicted for DPPH at both positions 1 and 2. For DPPH at position 2, Q_{ESR}(position 2) shows increased values because the B-fields of the modes at position 2 are lowered to a different extent depending on the resonator mode that is investigated. A lowered B-field of the mode corresponds to decreased losses due to DPPH and therefore with an increased Q_{ESR}. In this case the obtained values Q_{ESR}(position 2) can be rescaled with the known distribution of the magnetic flux density B as it is depicted in figure 4.12 to compare them with the obtained values Q_{ESR}(position 1) when DPPH is at position 1. The rescaled quality factor

$$Q_{\mathrm{ESR}}^{\mathrm{n\ rescaled}}(\text{position 2}) = \frac{B^n(\text{position 2})}{B^n(\text{position 1})} \cdot Q_{\mathrm{ESR}}^{\mathrm{n}}(\text{position 2}) \tag{4.32}$$

for the n'th mode when DPPH is placed at position 2 should equal Q_{ESR}(position 1). Here B^n is the distribution of the magnetic flux density of the n'th mode. The underlying idea assumes that Q depends anti proportional on the B-field $Q \propto \frac{1}{B}$ of the resonator modes, this motivates to rescale Q_{ESR}(position 2) in a way that it matches Q_{ESR}(position 1). The rescaled quality factor $Q_{\mathrm{ESR}}^{\mathrm{rescaled}}$(position 2) according to equation (4.32) can be seen in (b) in figure 4.16. $Q_{\mathrm{ESR}}^{\mathrm{rescaled}}$(position 2) matches the obtained Q_{ESR}(position 1) relatively good.

Slight errors occur because the dimensions of the DPPH sample on the resonator can't be evaluated exactly.

4.2.6 Power dependence of the TiO_2 modes

In this part of the analysis the power dependence of the resonator modes is investigated. For a power range of $-50\,\mathrm{dBm} < p < 16.8\,\mathrm{dBm}$ and two temperatures $T = 2\,\mathrm{K}, 7\,\mathrm{K}$ the quality factor Q of the parasitic and resonator modes was measured. The measured quality factors Q can be seen in figure 4.17 in (a) for $T = 2\,\mathrm{K}$ and in figure 4.18 in (a) for $T = 7\,\mathrm{K}$. In addition Q was measured for a magnetic flux density $B = 1.25\,\mathrm{T}$ and $T = 2\,\mathrm{K}$ as it can be seen in figure 4.19 in (a).
(b), (c) and (d) in figure 4.17 and 4.18 show the transmission coefficient for selected parasitic and resonator modes that exhibit strong non-linear effects towards high power. (b), (c) and (d) in figure 4.19 also show weak non-linear effects, but the overall quality factor of the investigated modes is strongly reduced because of the magnetic flux density $B = 1.25\,\mathrm{T}$. Also note that the background of the transmission coefficient decreases for higher power p because of the non-linear amplifier that is used.
Non-linear effects of superconducting resonators are a well-known feature as they are the result of a non-linear surface impedance R_s [48]. However there were different mechanisms proposed that can cause a rise in surface impedance R_s as the weak-link theory in granular substrates as proposed by Halbritter [49] or in general heating effects and intrinsic losses of the superconducting charge carriers. The weak-link theory of Halbritter can also be expanded with the assumption of local heating effects [50]. With increasing power p the current density j also increases which can cause vortex losses in the superconducting layer [51]. Although these mechanisms differ in their physical background, they aim to explain the behaviour of the surface impedance R_s of the superconductor as it is an important quantity to understand non-linear effects. Therefore it can also be said that non-linear effects occur when the current density j in the resonator exceeds a critical current density $j > j_{\mathrm{nl}}$, where nl denotes non-linear.
The measurements for $T = 2\,\mathrm{K}$, $B = 0\,\mathrm{T}$ as it can be seen in figure 4.17 in (a) show a constant quality factor Q for all resonator modes and parasitic modes up to a certain power that is here called p_{nl}. For $p > p_{\mathrm{nl}}$ a linear decrease of Q occurs. Note here that p is given in units of dBm which is a logarithmic scale. For the resonator modes it can be seen that p_{nl} increases when Q decreases. This is a result of the overall lowered quality factor Q, the disturbing effects of a greatly increased power p that can be modelled with a partial quality factor Q_p effects a lowered quality factor $Q(p < p_{\mathrm{nl}})$ less according to equation (2.16). It is natural to assume that the observed critical power p_{nl} marks the point where the critical current density $j > j_{\mathrm{nl}}$ is exceeded. The figures (b), (c) and (d) show that strong non-linear effects occur approximately for $p > 5\,\mathrm{dBm}$. These non-linear effects can often be modelled with a Duffing oscillator [50][52]

$$\ddot{x}(t) + \delta\dot{x}(t) + c_1 x(t) + c_3(x(t))^3 = F(t) \tag{4.33}$$

where F is an external force, δ is the damping, x is the amplitude, c_1 and c_3 are coefficients and t is the time. The additional cubic dependence with $c_3 \neq 0$ causes the observed transmission

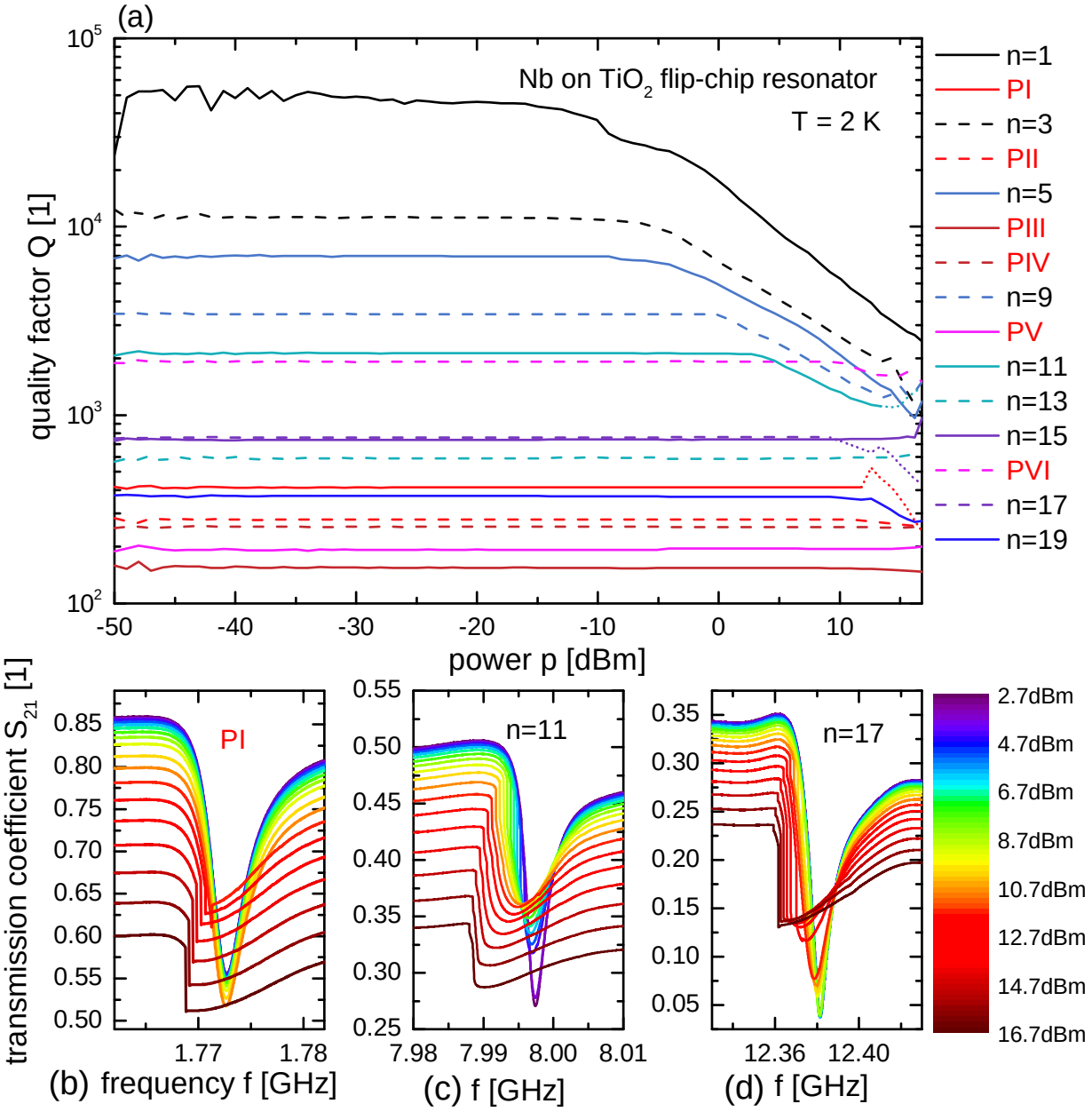

Fig. 4.17: (a) shows the measured quality factor Q of the resonator modes and parasitic modes in dependence of the power p for $B = 0\,\mathrm{T}$ and $T = 2\,\mathrm{K}$. Here the dotted lines represents data where strong non-linear effects have to be taken into account. (b), (c) and (d) show the transmission coefficient S_{21} of the PI, $n = 11$ and $n = 17$ modes.

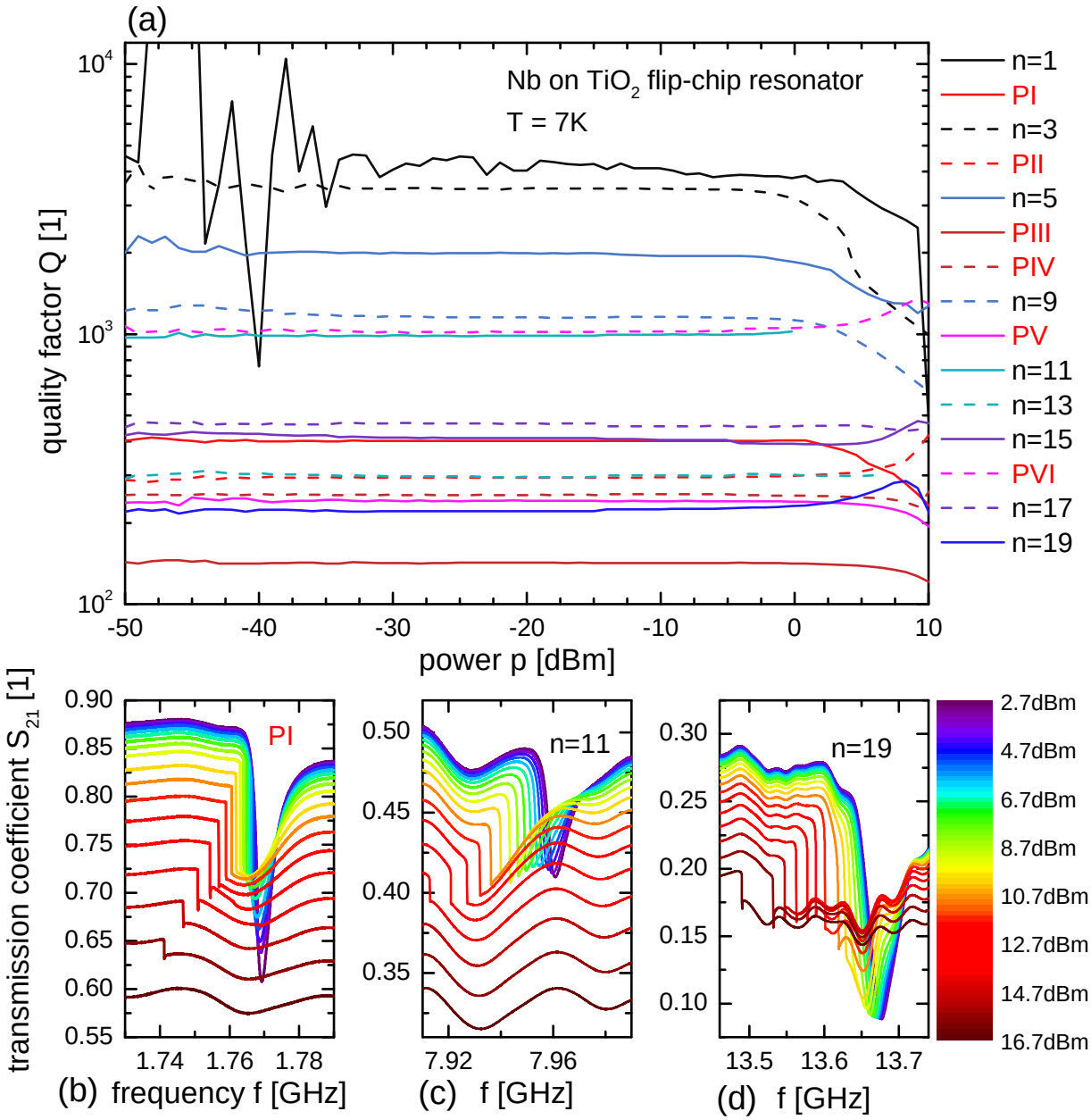

Fig. 4.18: (a) shows the measured quality factor Q of the resonator modes and parasitic modes in dependence of the power p for $B = 0\,\mathrm{T}$ and $T = 7\,\mathrm{K}$. (b), (c) and (d) show the transmission coefficient S_{21} of the PI, $n = 11$ and $n = 19$ modes.

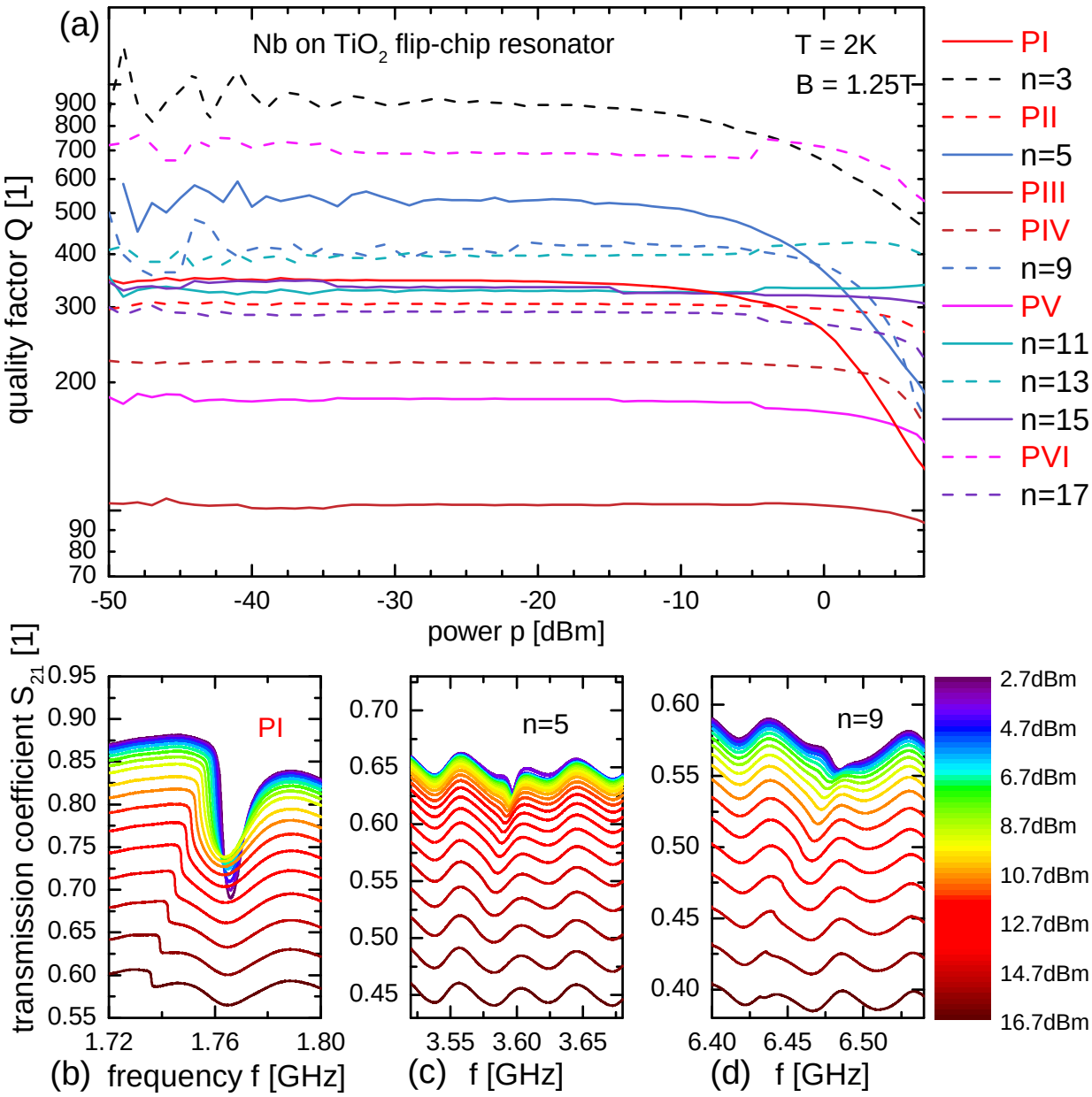

Fig. 4.19: (a) shows the measured quality factor Q of the resonator modes and parasitic modes in dependence of the power p for $B = 1.25\,\mathrm{T}$ and $T = 2\,\mathrm{K}$. (b), (c) and (d) show the transmission coefficient S_{21} of the PI, $n = 5$ and $n = 9$ modes.

steps. It can be assumed that c_3 directly depends on the power p.
The parasitic modes in figure 4.17 in (a) are almost constant with the exception of the PI mode that shows non-linear behaviour for $p > 5\,\mathrm{dBm}$ because of the Duffing oscillator. It is especially remarkable that the quality factor Q(PVI) of the PVI mode intersects with some of the resonator modes, again indicating a different loss mechanism for the parasitic modes. The quality factor of the parasitic modes is not that strongly affected by a greater temperature T or magnetic flux density B as the quality factor of the resonator modes as it could be seen in the preceding sections. Therefore it is appealing to measure the power dependence at greater temperature T and magnetic flux density B as the quality factor of the resonator modes and parasitic modes could be easier compared. However as it can be seen in figure 4.18 and figure 4.19 respectively in (a) the modes are more susceptible to the standing waves of the background which disturbs the resonances.
When investigating the quality factor for $T = 7\,\mathrm{K}$, $B = 0\,\mathrm{T}$, it can be seen in figure 4.18 in (b), (c) and (d) that non-linear effects for $p > 5\,\mathrm{dBm}$ need to be taken into account. However when only considering quality factors Q for $p < 5\,\mathrm{dBm}$ as it can be seen in figure 4.19 in (a) almost no power-dependent behaviour of Q can be observed as Q is already significantly lowered.
The same applies to the measured quality factor for $T = 2\,\mathrm{K}$, $B = 1.25\,\mathrm{T}$ as it can be seen in figure 4.19 in (a). In (b), (c) and (d) in figure 4.19 an even weaker quality factor of the modes can be observed. As a consequence the dependence of the quality factor Q on the power p cannot be systematically evaluated.

4.2.7 Interpretation of the data concerning the parasitic modes

The first considerations will focus on the parasitic modes PI-PV as PVI shows deviating effects that need to be investigated separately. When measuring the dependence of the parasitic modes on the temperature T and the magnetic flux density B, it could be seen that the quality factor decreases less when compared to the resonator modes. Also the resonance frequency decreases less when compared to the resonator modes. This means that parasitic modes cannot be as easily disturbed as resonator modes. It is natural to assume that the parasitic modes form cavity modes in the TiO_2 substrate. These cavity modes would be partially bounded by the TiO_2 substrate and the superconducting layer. This would also mean that the disturbing effects of a T sweep or a B sweep on the parasitic modes would be weaker as the parasitic modes are supported by the whole superconducting film whereas the standing wave of the resonator modes is located between the inner conductor and outer conductor of the coplanar waveguide.
The PVI mode is interesting because the quality factor behaves similar to the resonator modes but the frequency shift resembles more the behaviour of the parasitic modes. It can be assumed that the PVI mode is a slotline mode. It could be shown that finite grounding planes of different width can cause slotline modes and that the intensity of the slotline modes can be decreased when the grounding planes are bonded [53]. Bonding means that the outer conductor are connected with an air bridge over the inner conductor that prevents in the ideal case fluctuating differences of the potential. This is a common procedure when coplanar waveguides are used for circuit quantum electrodynamics [54].

However it is interesting that the parasitic modes and resonator modes showed a similar order of magnitude of the magnetic flux density B when the ESR measurement was executed. This would be no surprise for the PVI mode as it was assumed to be a slotline mode. However it is surprising when it comes to the cavity modes PI-PV because they would be distributed on the whole superconducting chip and therefore their intensity in the resonator should be less than in the case of the resonator modes that are localized in the resonator itself. It could be speculated that the parasitic modes also slightly couple into the resonator. This could explain the similar order of B of the resonator modes and parasitic modes.

4.3 Measurements concerning the background of the transmission signal

4.3.1 Temperature sweep of the background

In figure 4.20 the transmission signal of the flip-chip setup can be seen for TiO_2 for $0.05\,\mathrm{GHz} < f < 15\,\mathrm{GHz}$ in (a) and for $SrTiO_3$ for $0.05\,\mathrm{GHz} < f < 2\,\mathrm{GHz}$ in (c) for different temperatures $T = 2, 10, 20\,\mathrm{K}$. Resonances can be seen in the spectra for $T = 2\,\mathrm{K}$ which are investigated in their respective sections. For higher temperatures $T = 10, 20\,\mathrm{K}$ the resonances diminish as niobium is not superconducting any longer. The off-resonant transmission signal lowers for higher temperatures. Here the ratio

$$K_{T_1/T_2} = \frac{S_{21}^{T_1}}{S_{21}^{T_2}} \tag{4.34}$$

is defined as ratio of the transmission signals S_{21}^{T} at different temperatures. The ratio K can be seen in figure 4.20 in (b). The ratio of the transmission signals with $T = 2\,\mathrm{K}$ and $T = 10\,\mathrm{K}$ increases in dependence of the frequency f for TiO_2 and for $SrTiO_3$. The ratio of the transmission signals for $T = 10\,\mathrm{K}$ and $T = 20\,\mathrm{K}$ in the case of TiO_2 remains mostly constant.
The transmission signal in dependence of the temperature T can also be seen in figure 4.21 in (a) for the TiO_2 resonator and in (b) for the $SrTiO_3$ for several frequencies f. The transmission signal is normalized to the data at $T = 2\,\mathrm{K}$ in order to compare the transmission for different frequencies. The transmission signal has been further averaged over a frequency range of $0.5\,\mathrm{GHz}$ for the TiO_2 resonator and $0.05\,\mathrm{GHz}$ for the $SrTiO_3$ resonator to minimize the influence of the noise. It can be seen that the transmission strongly decreases for $T \approx 8.6\,\mathrm{K}$ in (a) and for $T \approx 7.4\,\mathrm{K}$ in (b). The strong decrease of the transmission signal depends on the frequency f, for higher frequencies f the transmission signal tends to decrease stronger. In addition a maximum of the transmission coefficient S_{21} can be seen at $2\,\mathrm{K} < T < 3\,\mathrm{K}$. A further rise of the transmission spectrum occurs at $T = 11\,\mathrm{K}$ in (a) but it also has to be taken into account that the temperature step width was increased from $\Delta T = 0.1\,\mathrm{K}$ for $T < 10\,\mathrm{K}$ to $\Delta T = 1\,\mathrm{K}$ for $T > 10\,\mathrm{K}$. The higher temperature step width ΔT results in a stronger heating that could also cause a higher error for the transmission.
The decrease of transmission signal occurs approximately at the critical temperature of

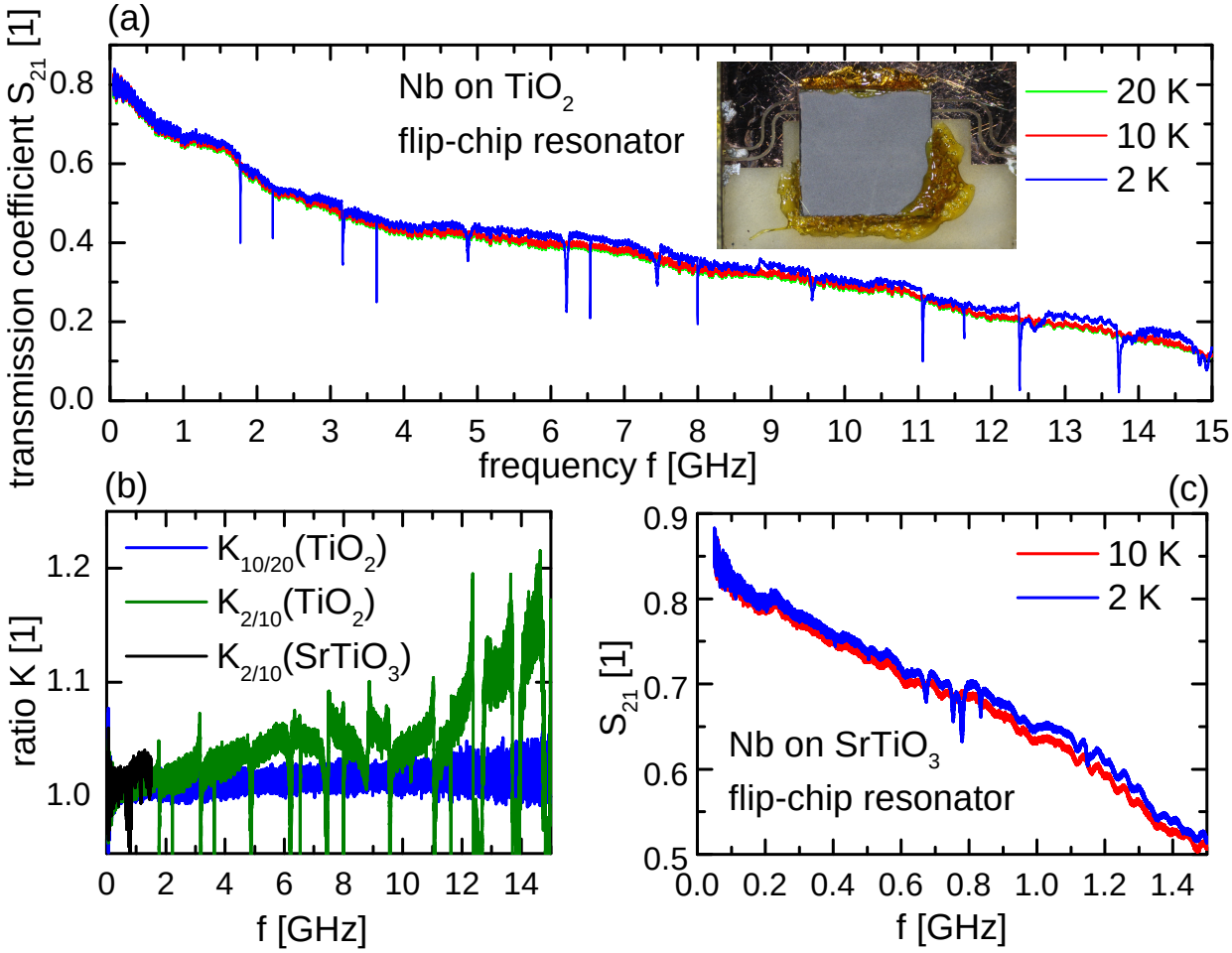

Fig. 4.20: The transmission signal of the flip-chip setup can be seen for TiO_2 in (a) and for $SrTiO_3$ in (c) for different temperatures $T = 2, 10, 20\,\mathrm{K}$. For $T = 2\,\mathrm{K}$ resonances can be seen in the spectrum. The inset in (a) shows a photograph of the mounted flip-chip on the feedline. For higher temperatures it can be seen that the broadband background transmission signal lowers. The ratio K of the transmission signals for both materials TiO_2 and $SrTiO_3$ according to equation (4.34) for different temperatures can be seen in (c). The shift of the transmission signal depends on the frequency.

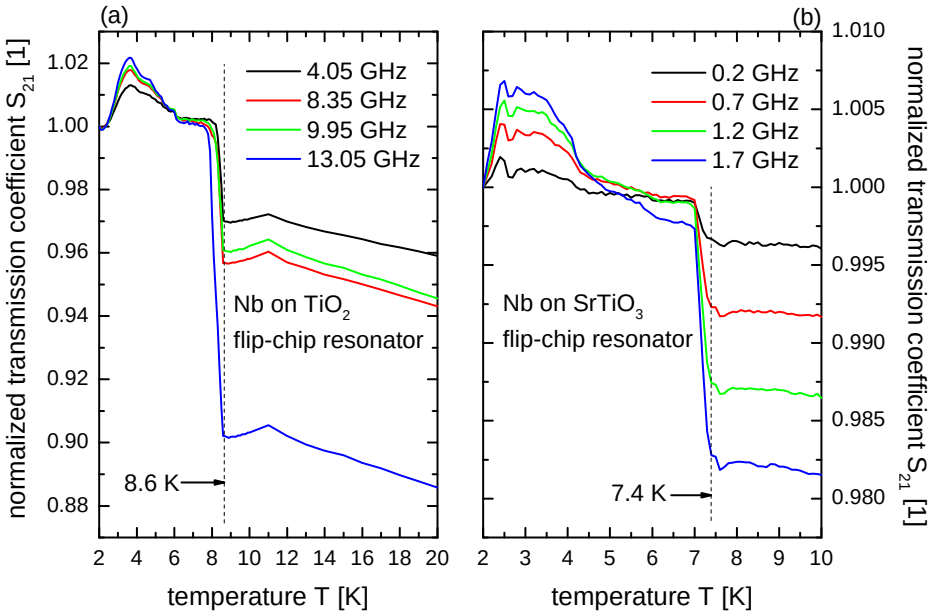

Fig. 4.21: The transmission coefficient S_{21} normalized to it's value at 2 K for different frequencies f can be seen in dependence of the temperature T. (a) shows S_{21} for the TiO_2 resonator and (b) for the $SrTiO_3$ resonator. S_{21} has been averaged over a frequency range of 0.5 GHz for the TiO_2 resonator and 0.05 GHz for the $SrTiO_3$ resonator to minimize the noise-disturbance.

niobium $T \approx T_c$. The critical temperatures that are observed in (a) and (b) in figure 4.21 differ because the sputtering process is not exactly reproducible. Superconducting niobium dispels a magnetic field (Meißner-Ochsenfeld effect), therefore it can be assumed as a perfect shielding layer that separates the high ϵ dielectric of interest from the feedline as depicted in figure 3.4. For $T > T_c$ niobium is normal conducting and therefore does not shield the high ϵ dielectric perfectly, resulting in a small increase of the effective dielectric constant ϵ_{eff} of the feedline. The increased ϵ_{eff} causes a decreased impedance of the feedline Z_{feedline} according to equation (2.33) and increases as result the reflection R according to equation (2.19). The increased reflection R can be observed as a lowered transmission coefficient S_{21}. This effect of the niobium film on the feedline heavily depends on the distance h between the feedline and the flip-chip.

The shift of the transmission signal S_{21} in dependence of the temperature T depends on the frequency f. In figure 4.20 in (b) it can be seen that the ratio $K_{2/10}$ for both materials significantly increases for $f > 2\,\text{GHz}$. The wavelength of the quasi TEM mode in the feedline for $f = 2\,\text{GHz}$ with $\epsilon_{\text{eff}} = 4.95$ from table 3.2 in the case of absent flip-chip can be calculated to

$$\lambda = \frac{c}{f\sqrt{\epsilon_{\text{eff}}}} = 6.7\,\text{cm} \tag{4.35}$$

for $c = 2.997 \cdot 10^8\,\frac{\text{m}}{\text{s}}$. This wavelength $\lambda = 6.7\,\text{cm}$ is larger than the dimensions of the flip-chip with side length $s = 5\,\text{mm}$. The greater wavelength $\lambda > s$ results in a weaker rise of the impedance for lower frequencies and therefore results in lower reflections R for lower

frequencies $f < 2\,\mathrm{GHz}$.
With an appropriate reference measurement or detailed simulations, the temperature dependence of the background could possibly be used to determine the distance h between the flip-chip and feedline.

5 Summary

Measurements on the superconducting flip-chip microwave resonator that was deposited on TiO_2 showed the resonance frequency in the fundamental mode and their odd multiples $n = 1, 3, 5, ...$ and parasitic modes. The anisotropic dielectric constant ϵ of TiO_2 could be taken into account by splitting the meander-shaped resonator into partial sections with defined ϵ_i. With the continuity condition of the standing waves at the interface of the partial sections the resonance frequencies f could be calculated. The effective dielectric constants of the resonators were assumed as $\epsilon_{\text{aa-eff}} = 57$ and $\epsilon_{\text{ac-eff}} = 81$. The measured and calculated resonance frequencies differ less compared to the case where one would have just assumed odd multiplies $n = 1, 3, 5, ...$ of the fundamental mode and compared them with the measured resonance frequency.
The parasitic modes and resonator modes could be clearly separated by investigating the resonance frequencies and their odd multiples. Additional experimental procedures were studied to separate the resonator modes and parasitic modes. One of them was the observation of the temperature-dependent behaviour of the resonator modes and parasitic modes in their quality factors Q and resonance frequencies f. It could be shown that the resonance frequencies of the resonator and parasitic modes respectively form bundles and decrease towards T_c. The quality factor Q of the parasitic modes showed small effects towards T_c whereas Q of all resonator modes continually decreased with T.
Similar results were found when the dependence of the quality factor Q and the resonance frequency f on the magnetic flux density B was observed. The resonance frequency f of the resonator modes and parasitic modes respectively form bundles that fall off towards $B = 2\,\text{T}$, The onset of the frequency shift was at $B = 0.2\,T$. When investigating the quality factor, a strong decrease of Q for $B > 0.2\,\text{T}$ in case of the resonator modes could be observed, even stronger than in the temperature-dependent measurements, whereas Q of the parasitic modes only changed slightly towards $B = 2\,\text{T}$. The different T- and B-behaviour of the parasitic modes and resonator modes can be explained when considering the different distribution of the modes on the superconducting film. Parasitic modes that are supported by the whole superconducting Nb-film are less disturbed by stronger loss mechanisms than the resonator modes that are mainly supported by the inner conductor of the resonator.
ESR measurements were performed in order to distinguish the parasitic modes and resonator modes. A DPPH sample was deposited on two positions on the resonator where different magnetic flux densities B of the resonator modes could be expected. By measuring the quality factor Q of all modes the effects of the DPPH sample could be evaluated by extracting Q_{ESR} which accounts for the losses caused by DPPH. By depositing DPPH on a different position it could be seen that the effects of the DPPH sample on the quality factor directly depends on the distribution of B on the resonator. Q_{ESR} showed for the parasitic and resonator modes a similar order of magnitude, indicating that their B-field components also have a similar

order of magnitude. When fitting Q_{ESR} for the resonator modes when DPPH was deposited on the open end of the resonator a decrease $Q_{\mathrm{ESR}} \propto \frac{1}{B^n}$ with $n = 0.85$ could be found.
A power-dependent measurement of the quality factor showed for resonator modes and parasitic modes inharmonicities for higher power $p > 5\,\mathrm{dBm}$ that can be modelled with a Duffing oscillator. For the resonator modes a decrease of the quality factor Q could be seen when the power exceeded a fixed value p_{nl}. p_{nl} was greater for higher modes n. The decrease of the quality factor Q can be explained with a critical current density j_{nl} where non-linear effects have to be taken into account. The parasitic modes showed no decrease in dependence of the power which indicates that their critical current density j_{nl} was not exceeded when the power sweep was performed.
In addition the temperature dependence of the off-resonant transmission signal was investigated which showed a strong decrease at T_c of niobium. This can be assigned to the loss of superconductivity where the perfect shielding of the high ϵ flip-chip from the feedline is not any longer given. The high ϵ flip-chip can slightly alter the impedance of the coplanar feedline resulting in increased reflections.

6 Outlook

The results of this Bachelor thesis can be used to distinguish the resonator modes and parasitic modes. Additional measurements where the temperature dependence and magnetic flux density dependence of all modes on superconducting resonators would be observed, could be used to distinguish the resonator modes and parasitic modes. This simplifies mode identification a lot. A more elaborate mode identification process becomes necessary when the fundamental mode of the resonator is missing, here this thesis can serve as reference.
The ESR measurements could be further advanced and applied with higher precision to determine the distribution of the magnetic flux density. This would also help in the characterization of already known resonator modes and parasitic modes. A more detailed knowledge on the distribution of the modes on the superconducting layer could also deepen the insight on the parasitic modes. A higher precision would be possible with a standardized amount of DPPH that is deposited.
The dependence of the off-resonant transmission signal on the superconducting layer could be used to measure the distance between the flip-chip and the feedline in situ with an appropriate reference. Investigations on the appropriate references would include to measure flip-chip resonators with different dielectric constants ϵ of the flip-chip at different distances h to the feedline, this is necessary to evaluate the effects of ϵ of the dielectric and h on the off-resonant transmission signal. Simulations can also be used as they are a powerful tool, whereas it needs to be checked if the simulations and the experiments show the same tendencies for varying ϵ and h.
As the flip-chip setup is appropriate to measure high dielectric constants, it is further desired to investigate more on the microwave properties of the setup. This includes a detailed investigation on the coupling. This would allow in the best case to find an equivalent circuit diagram for the flip-chip setup where the inductances, capacitances and resistances can be linked to the geometry of the setup. This was only briefly discussed in this thesis, but it would help to examine the behaviour of the modes more quantitatively.

Appendix

A: Measurements concerning the background: Power sweep of the background

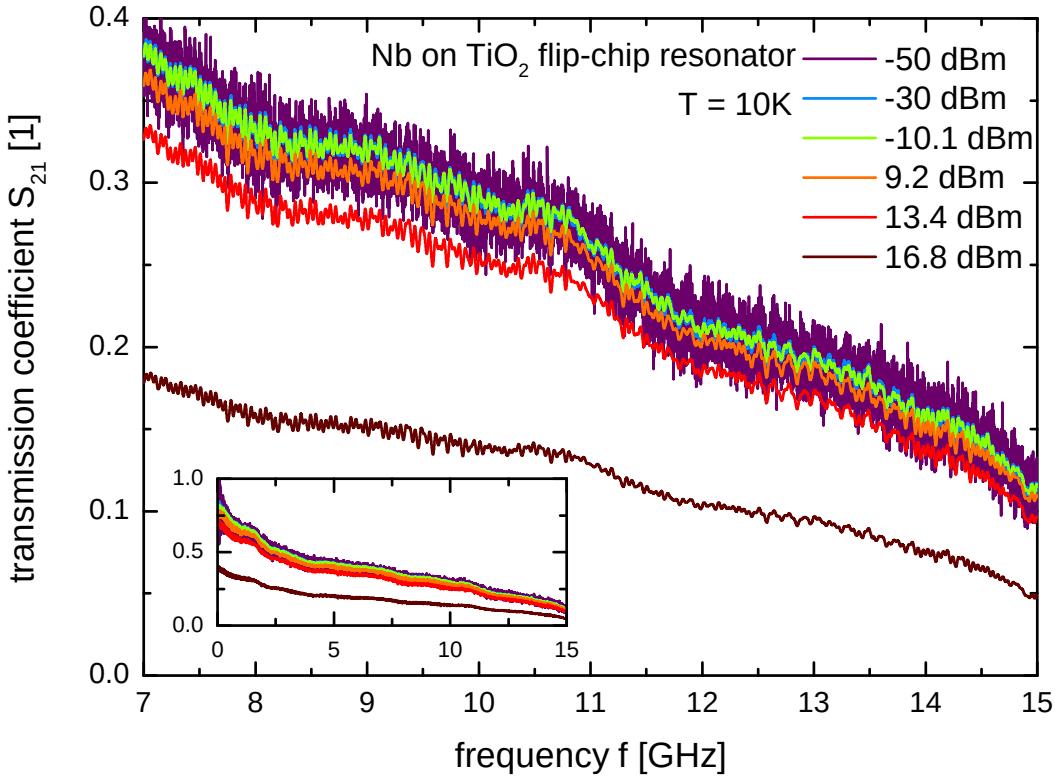

Fig. 6.1: Transmission spectrum $S_{21}(f)$ of the flip-chip setup at temperature $T = 10\,\mathrm{K}$ above the critical temperature T_c of niobium. The transmission coefficient S_{21} remains relatively constant for $-50\,\mathrm{dBm} < p < -10\,\mathrm{dBm}$ and decreases for all frequencies f for $p > -10\,\mathrm{dBm}$.

In figure 6.1 the transmission signal S_{21} can be seen for the flip-chip setup at temperature $T = 10\,\mathrm{K}$ for different power settings p. The transmission signal without resonances is referred to as background. As the temperature $T = 10\,\mathrm{K} > T_c$ is above the critical temperature of niobium, the resonator modes are suppressed. The set power p_{set} at the VNA and the amplified power p_{true} that is transmitted to the coplanar waveguide p_{true} are shown in table 6.1. It can be seen in figure 6.1 that for a set power $-50\,\mathrm{dBm} < p < -10\,\mathrm{dBm}$ the transmission

p_{set} [dBm]	p_{true} [dBm]	p_{set} [dBm]	p_{true} [dBm]	p_{set} [dBm]	p_{true} [dBm]
-73	-50	-49	-26	-25	-2.2
-72	-49	-48	-25	-24	-1.2
-71	-48	-47	-24	-23	-0.2
-70	-47	-46	-23	-22	0.8
-69	-46	-45	-22	-21	1.7
-68	-45	-44	-21	-20	2.7
-67	-44	-43	-20	-19	3.6
-66	-43	-42	-19	-18	4.6
-65	-42	-41	-18	-17	5.5
-64	-41	-40	-17	-16	6.5
-63	-40	-39	-16	-15	7.4
-62	-39	-38	-15	-14	8.3
-61	-38	-37	-14	-13	9.2
-60	-37	-36	-13	-12	10.1
-59	-36	-35	-12	-11	10.9
-58	-35	-34	-11	-10	11.8
-57	-34	-33	-10.1	-9	12.6
-56	-33	-32	-9.1	-8	13.4
-55	-32	-31	-8.1	-7	14.2
-54	-31	-30	-7.1	-6	14.9
-53	-30	-29	-6.1	-5	15.6
-52	-29	-28	-5.1	-4	16.2
-51	-28	-27	-4.1	-3	16.8
-50	-27	-26	-3.1		

Tab. 6.1: Set power p_{set} at the VNA and the transmitted power p_{true} to the coplanar waveguide itself. The power is amplified by 23 dBm for lower powers. The non-linearity of the amplifier needs to be taken into account for higher powers.

coefficient does shift only slightly. For $p = -50\,\text{dBm}$ it can be seen that the transmission signal exhibits a lower signal-to-noise ratio. For $p = 9.2\,\text{dBm}$, $p = 13.4\,\text{dBm}$ and $p = 16.8\,\text{dBm}$ the transmission signal strongly decreases over the whole frequency range. When measuring the transmission at high powers additional losses need to be taken into account as heating effects that lower the overall transmission. But the main reason for the decreasing transmission coefficient is the non-linear amplifier which nominally amplifies by $+23\,\text{dBm}$ but for input powers $p > -30\,\text{dBm}$ only amplifies less.

B: Exemplary python script to account for an anisotropic ϵ

An important part of this thesis was the calculation of the effects of an anisotropic ϵ on the resonator modes. Here shall be presented an exemplary python script that returns the resonance frequencies and the distribution of the electric field E on a resonator for a set frequency range.

```
import numpy as np
import matplotlib.pyplot as plt
from scipy import fftpack
import os

#Partial lengths defined here (in ym), here lg is the coupling arm
lg = 800. + 285.*np.pi/4.
lf = 580. + 285.*np.pi/2.
le = 1020. + 0.25*285. * np.pi + 580.*0.125*np.pi
ld = 580.*0.25*np.pi
lc = 3200. + 0.125*580. * np.pi + 580.*0.125*np.pi
lb = 580.*0.25*np.pi
la = 3200. + 580.*0.125*np.pi

#respective epsilon values defined here
epsaa = 81.
epsac = 57.

#define minimum frequency and maximum frequency as well as numberpoints
freqmin = 0.05 * 10**9
freqmax = 5.   * 10**9
nump1 = 15001

#second numberpoints, is important for the distribution of E or B
nump2 = 31

c = 2.997 * 10**8
f0 = np.linspace(freqmin, freqmax, num=nump1, endpoint=True)
k0 = 2.* np.pi *f0 /c

#adjust these arrays to account for the partial lengths and respective dielectric constants
ss = np.array([ la, lb, lc, ld, le, lf, lg ]) * 10**(-6)
eps = np.array([ epsaa, epsac, epsaa, epsac, epsaa, epsac, epsaa ])

#print(ss)
#Creates a file "howsdevided.dat" that marks the partial lengths across the whole length
zeross = np.zeros(len(ss))
toprint = np.zeros(len(ss))
for i in range(0, len(ss)):
        toprint[i] = np.sum(ss[:i])
matrixc = np.zeros((len(ss),2), dtype=float)
matrixc[:, 0] = toprint
matrixc[:, 1] = zeross
np.savetxt('howsdivided.dat', matrixc, delimiter = '\t')

def delta(i):
        return np.sqrt( eps[i-1] / eps[i] )

y = np.zeros(len(k0))
y_z = np.zeros(len(k0))
y_y = np.zeros(len(k0))

#xi_1 and xi_2 are calculated, see thesis for details
for j in range(0, len(k0)):
        sinus = np.sin(k0[j] * np.sqrt(eps) * ss)
        cosinus = np.cos(k0[j] * np.sqrt(eps) * ss)
        tangens = np.tan(k0[j] * np.sqrt(eps) * ss)
        Z_iter = 1.
        Y_iter = tangens[0]
        for i in range(1, len(ss)):
                speicher = Z_iter
                Z_iter = delta(i) * cosinus[i] * Z_iter - sinus[i] * Y_iter
                Y_iter = delta(i) * sinus[i] * speicher + cosinus[i] * Y_iter
        y[j] = Z_iter / Y_iter
        y_z[j] = Z_iter  #xi_1
        y_y[j] = Y_iter  #xi_2

#n multiples and resonance frequencies are calculated
```

```
lsg = np.array([0])
y_lsg = lsg
y_z_lsg = lsg
y_y_lsg = lsg
for j in range(0, len(k0)-1):
        if ((y[j]>0) and (y[j+1]<0)): #condition xi_1/xi_2 = 0
                y_lsg = np.append( y_lsg, [(y[j]+y[j+1])/2], 0)
                y_z_lsg = np.append(y_z_lsg, [(y_z[j]+y_z[j+1])/2], 0)
                y_y_lsg = np.append(y_y_lsg, [(y_y[j]+y_y[j+1])/2], 0)
                lsg = np.append(lsg, [(k0[j]+k0[j+1])/2], 0)
lsg_norm = lsg / lsg[1]
print('n multiples' + str(lsg_norm[1:]))
y_lsg = y_lsg[1:]
lsg = lsg[1:]
y_z_lsg = y_z_lsg[1:]
y_y_lsg = y_y_lsg[1:]
print('frequencies of the modes:' + str(lsg * 0.5*c/np.pi))

#resonance frequencies and 'odd' multiples are saved into file frequencies.dat
matrixa = np.zeros( (len(lsg_norm[1:]), 2), dtype=float )
matrixa[:, 0] = lsg_norm[1:]
matrixa[:, 1] = lsg * 0.5*c/np.pi
np.savetxt('frequencies.dat', matrixa, delimiter = '\t')

#Here the Efield distribution on the resonator length is calculated
matrixb = np.zeros( (len(ss)*nump2, len(lsg)+1), dtype=float )
for n in range(0, len(lsg)):
        sinus = np.sin( lsg[n] * np.sqrt(eps) * ss )
        cosinus = np.cos( lsg[n] * np.sqrt(eps) * ss )
        tangens = np.tan( lsg[n] * np.sqrt(eps) * ss )
        ber_kont = np.array([0])
        Efield_kont = np.array([0])
        for i in range(0, len(ss)):
                Z_iter = 1./y_y_lsg[n]
                Y_iter = tangens[0] / y_y_lsg[n]
                ss_ers = 0
                for j in range(0, i):
                        ss_ers = ss_ers + ss[j]
                bereich = np.linspace( ss_ers, ss_ers + ss[i], num=nump2, endpoint=True )
                ber  = np.linspace( -ss[i] , 0, num=nump2, endpoint = True)
                for m in range(1,i+1):
                        speicher = Z_iter
                        Z_iter = delta(m) * cosinus[m] * Z_iter - sinus[m] * Y_iter
                        Y_iter = delta(m) * sinus[m] * speicher + cosinus[m] * Y_iter
                #plotted is the Efield, if Bfield is wished, comment out the Efield, take in Bfield and
                #replace three lines under this Efield also with Bfield (nothing more needed)
                Efield = Z_iter* np.sin( lsg[n]*np.sqrt(eps[i])*ber ) + Y_iter* np.cos( lsg[n]*np.sqrt(eps[i])*ber )
                #Bfield=np.sqrt(eps[i])*(Z_iter*np.cos(lsg[n]*np.sqrt(eps[i])*ber)-Y_iter*np.sin(lsg[n]*np.sqrt(eps[i])*ber))
                Efield_kont = np.append( Efield_kont, Efield, 0 ) #if Bfield is wished, replace Efield with Bfield
                ber_kont = np.append( ber_kont, bereich, 0 )
                plt.plot(bereich[-1], 0.5, 'o')
        plt.plot( ber_kont[1:] , np.abs((Efield_kont[1:])), '-',label="Mode n=" + str(2*n+1) )
        matrixb[:, n+1] = np.abs((Efield_kont[1:]))
plt.legend()
plt.grid()
plt.show()

#saves distribution of the Efield (or Bfield) in fielddistribution.dat
matrixb[:,0] = ber_kont[1:]
np.savetxt('fielddistribution.dat', matrixb, delimiter = '\t')
```

Deutsche Zusammenfassung

Supraleitende Mikrowellenresonatoren sind ein aktuelles Forschungsgebiet. Supraleitende koplanare Wellenleiter, an die Mikrowellenresonatoren gekoppelt sind, werden als unabdingbar angesehen wenn es darum geht Quantencomputer zu konstruieren. Entsprechend konnten schon Einzelphotonendetektoren konstruiert werden als auch Mikrowellenresonatoren deren Güte $Q > 10^6$ übersteigt. Ähnliche Mikrowellenresonatoren können allerdings auch verwendet werden um die dielektrischen Eigenschaften interessanter Materialien mit hoher Präzession zu messen. Dies wird auch an der Universität Stuttgart getan, diese Bachelorarbeit reiht sich ein in jene Abfolge der Arbeiten, die der Untersuchung von dielektrischen Eigenschaften interessanter Materialien bei kryogenen Temperaturen dient.
Vorangegangene Master-Arbeiten von Lars Wendel und Vincent Engl verwendeten ein Distanz Flip-Chip Aufbau, bei dem das zu untersuchende Material mit einer dünnen Niob-Schicht an der Oberfläche versehen wurde, auf der ein $\frac{\lambda}{4}$-Resonator aufgebracht wurde. Das dergestalt präparierte Material, der Flip-Chip, wurde dann mit einem festen Abstand zur Feedline auf die Feedline aufgebracht. Hierbei liegt die Niob-Schicht der Feedline gegenüber und der Kopplungsarm des Resonators liegt direkt oberhalb der Feedline. Bei der Messung der Transmission in Abhängigkeit der Frequenz sind Absorptionsverluste beobachtbar, diese werden durch den induktiv gekoppelten Flip-Chip verursacht und liegen entsprechend bei den ungeraden Vielfachen der Grundmode.
Allerdings zeigen sich auch Absorptionsverluste bei weiteren Frequenzen, diese können nicht direkt dem Resonator zugeordnet werden und werden als parasitäre Moden bezeichnet. Ihr Auftreten ist nicht ungewöhnlich und häufig der Fall, da sie Boxmoden darstellen können. Wenn allerdings die Grundmode des Resonators nicht sichtbar ist oder wesentlich schwächer, wie dies beim Flip-Chip schon öfters der Fall war, dann ist die Identifizierung der Moden nicht eindeutig. Die vorliegende Bachelorarbeit greift diese Problematik auf und hat zum Ziel die Eigenschaften der parasitären Moden zu charakterisieren und Möglichkeiten zu finden, parasitäre Moden und tatsächliche Resonatormoden zu identifizieren. Dazu wird das Verhalten der parasitären Moden und Resonatormoden auf einem TiO_2 Flip-Chip untersucht. Messungen mit dem supraleitenden TiO_2 Flip-Chip Mikrowellen-Resonator zeigten die Grundmode sowie ihre ungeraden Vielfache $n = 1, 3, 5, ...$ wie sie erwartet worden sind als auch die parasitären Moden. Die anisotrope Dielektrizitätskonstante ϵ von TiO_2 konnte dabei berücksichtigt werden, indem die Mäanderform des Resonators in Teilsequenzen mit konstantem ϵ_i aufgeteilt wurde. Mit der Kontinuitätsbedingung an den Schnittstellen zwischen den Teilsequenzen konnte die Frequenz f der stehenden Welle bestimmt werden. Dazu wurde die effektive Dielektrizitätszahl des Resonators auf $\epsilon_{\text{aa-eff}} = 57$ und $\epsilon_{\text{ac-eff}} = 81$ geschätzt. Die gemessenen und berechneten Resonanzfrequenzen unterscheiden sich dabei weniger gegenüber dem Fall, wenn für die zu erwartende Resonanzfrequenz das ungerade Vielfache $n = 1, 3, 5, ...$ der Grundmode angenommen worden wäre.

Die parasitären Moden und Resonatormoden konnten klar getrennt werden indem die Resonanzfrequenz und ihre ungeraden Vielfache betrachtet wurden. Zusätzliche Experimente wurden durchgeführt um die Resonatormoden und parasitären Moden zu trennen. Eine dieser Experimente war die Aufnahme der Temperaturabhängigkeit der Güten Q und der Resonanzfrequenzen f der Resonatormoden und parasitären Moden. Es konnte beobachtet werden, dass die Resonanzfrequenzen der Resonatormoden und parasitären Moden jeweils Bündel formen und zu T_c hin abnehmen. Die Güte Q der parasitären Moden zeigten schwache Effekte zu T_c hin, wohingegen die Güte der Resonatormoden kontinuierlich mit der Temperatur T abnahmen.
Zu ähnliche Ergebnisse war man gekommen als die Güte Q und die Resonanzfrequenz f in Abhängigkeit des Magnetfeldes B aufgenommen wurden. Die Resonanzfrequenzen f der Resonatormoden und parasitären Moden formen jeweils Bündel und fallen zu $B = 2\,\mathrm{T}$ ab, der Abfall konnte für $B > 0,2\,\mathrm{T}$ beobachtet werden. Im Falle der Resonatormoden fällt die Güte Q für $B > 0,2\,\mathrm{T}$ stark ab, noch stärker als sie bei der T-Abhängigkeit beobachtet werden konnte. Dahingegen veränderte sich die Güte Q der parasitären Moden erst zu $B = 2\,\mathrm{T}$ hin. Das unterschiedliche Verhalten der parasitären Moden und Resonatormoden bei der T- und B- Abhängigkeit kann mit der unterschiedlichen Verteilung der Moden auf der supraleitenden Fläche erklärt werden. Parasitäre Moden werden durch den ganzen supraleitenden Film unterstützt, bei dem Verlusteffekte einen vergleichsweise geringere Störung verursachen als bei den Resonatormoden, die empfindlich von dem schmalen Innenleiter des Resonators abhängen.
Um parasitäre Moden und Resonatormoden zu unterscheiden sind weiterhin ESR Messungen durchgeführt worden. Eine DPPH Probe ist auf zwei Positionen auf dem Resonator aufgebracht worden, bei der unterschiedliche Magnetfelder B der Resonatormode erwartet werden konnten. Indem die Güte Q aller Moden gemessen worden ist, konnten die Effekte der DPPH Probe beurteilt werden indem Q_{ESR} berechnet wurde, welches gerade die Verlusteffekte des DPPH berücksichtigt. Durch das Auftragen von DPPH auf zwei unterschiedliche Positionen konnte gezeigt werden, dass die Verlusteffekte des DPPH direkt von der Verteilung des B-Feldes auf dem Resonator abhängen. Q_{ESR} zeigte sowohl für parasitäre als auch Resonatormoden eine ähnliche Größenordnung, dies impliziert auch eine ähnliche Größenordnung für das B-Feld. Ferner konnte Q_{ESR} der Resonatormoden gefittet werden welches einen Abfall $Q_{\mathrm{ESR}} \propto \frac{1}{B^n}$ mit $n = 0.85$ zeigt, hierbei war die DPPH Probe auf dem offenen Ende des Resonators aufgebracht.
Die Leistungsabhängigkeit der Güte Q zeigte sowohl für Resonatormoden als auch parasitäre Moden Inharmonizitäten für $p > 5\,\mathrm{dBm}$, diese können mit einem Duffing-Oszillator modelliert werden. Für die Resonatormoden konnten ein Abfall der Güte Q beobachtet werden, wenn die Leistung p einen festgelegten Wert p_{nl} überschritt. p_{nl} ist hierbei größer für höhere Moden n. Die Abnahme der Güte Q kann mit der kritischen Stromdichte j_{nl} erklärt werden, wo zusätzliche nichtlineare Effekte berücksichtigt werden müssen. Die Güte Q der parasitären Moden zeigen keine Abnahme in Abhängigkeit der Leistung, dies deutet darauf hin dass ihre kritische Stromdichte j_{nl} während der Messung nicht überschritten wurde.
Zusätzlich ist die Temperaturabhängigkeit des Transmissionssignals abseits der Moden gemessen worden. Das Transmissionssignal fällt stark bei der kritischen Temperature T_c von Niob ab. Dafür kann der Verlust der Supraleitung von Niob verantwortlich gemacht werden,

die supraleitende Schicht schirmt nämlich die hohe Dielektrizitätskonstante des Flip-chip ab, sobald die Supraleitung nicht mehr vorliegt, kann die hohe Dielektrizitätskonstante die Feedline schwach stören. Dies bewirkt eine schwach veränderte Impedanz der Feedline wodurch die Reflektion zunimmt und die Transmission abnimmt.
Diese Ergebnisse können dazu verwendet werden um parasitäre Moden und Resonatormoden besser zu unterscheiden, auch wenn die Grundmode des Resonators unterdrückt ist. Die ESR Messmethode kann noch weiter ausgebaut werden um die Verteilung des B-Feldes genauer zu messen. Die Abhängigkeit des Transmissionssignal von der Temperatur abseits der Moden kann dazu verwendet werden um den Abstand des Flip-Chip von der Feedline zu messen, dafür sind aber weitere Messreihen oder Simulationen als Referenz notwendig.

Acknowledgments

I want to thank everybody, who made this project possible and supported me throughout. In particular I want to thank

- Prof. Dr. Martin Dressel, for giving me the opportunity to work on this project
- Dr. Marc Scheffler, for being my supervisor and for the helpful guidance and discussions
- Nikolaj Ebensperger for being my direct supervisor and for the introduction to the lab
- Gabi Untereiner for sample preparation and assembling
- Konstantin Nikolaou for helpful discussions and new ideas
- Marius Tochtermann for introducing me to the flip-chip samples
- the low temperature department, for continuous supply of liquid helium
- the whole of 1. Physikalisches Institut, for the pleasant research atmosphere.

Eigenständigkeitserklärung

Ich, Cenk Beydeda, bestätige hiermit, dass ich die vorliegende Arbeit eigenständig verfasst habe. Es wurden keine anderen Quellen verwendet als die angegebenen und alle wörtlich oder sinngemäß aus anderen Werken übernommenen Aussagen als solche gekennzeichnet. Diese Arbeit wurde weder vollständig, noch in Teilen in einem anderen Prüfungsverfahren verwendet und weder vollständig noch in Teilen bereits veröffentlicht. Der Inhalt des elektronischen Exemplars ist mit dem Inhalt des Druckexemplars identisch.

Stuttgart, den 30. September 2020

References

[1] C. P. Wen, *IEEE Trans. Microw. Theory Tech.* **17**, 1087 (1969).

[2] M. Göppl, A. Fragner, M. Baur, R. Bianchetti, S. Filipp, J. M. Fink, P. J. Leek, G. Puebla, L. Steffen, and A. Wallraff, *J. Appl. Phys.* **104**, 113904 (2008).

[3] A. Megrant, C. Neill, R. Barends, B. Chiaro, Y. Chen, L. Feigl, J. Kelly, E. Lucero, M. Mariantoni, P. J. J. O'Malley, D. Sank, A. Vainsencher, J. Wenner, T. C. White, Y. Yin, J. Zhao, C. J. Palmstrøm, J. M. Martinis, and A. N. Cleland, *Appl. Phys. Lett.* **100**, 113510 (2012).

[4] R. Barends, J. J. A. Baselmans, J. N. Hovenier, J. R. Gao, S. J. C. Yates, T. M. Klapwijk, and H. F. C. Hoevers, *IEEE Trans. Appl. Supercond.* **17**, 263 (2007).

[5] A. Wallraff, D. Schuster, A. Blais, L. Frunzio, R.-S. Huang, J. Majer, S. Kumar, S. Girvin, and R. Schoelkopf, *Nature* **431**, 162 (2004).

[6] D. S. Rausch, M. Thiemann, M. Dressel, D. Bothner, D. Koelle, R. Kleiner, and M. Scheffler, *J. Phys. D* **51**, 465301 (2018).

[7] M. Thiemann, M. H. Beutel, M. Dressel, N. R. Lee-Hone, D. M. Broun, E. Fillis-Tsirakis, H. Boschker, J. Mannhart, and M. Scheffler, *Phys. Rev. Lett.* **120**, 237002 (2018).

[8] N. G. Ebensperger, M. Thiemann, M. Dressel, and M. Scheffler, *Supercond. Sci. Technol.* **29**, 115004 (2016).

[9] N. G. Ebensperger, B. Ferdinand, D. Koelle, R. Kleiner, M. Dressel, and M. Scheffler, *Rev. Sci. Instrum.* **90**, 114701 (2019).

[10] L. Wendel, V. T. Engl, G. Untereiner, N. G. Ebensperger, M. Dressel, A. Farag, M. Ubl, H. Giessen, and M. Scheffler, *Rev. Sci. Instrum.* **91**, 054702 (2020).

[11] V. T. Engl, N. G. Ebensperger, L. Wendel, and M. Scheffler, arXiv:1911.11456 [cond-mat.supr-con] (2019).

[12] M. Tochtermann, *Bachelor thesis: Optimierung von supraleitenden Mikrowellenresonatoren auf SrTiO3* (University of Stuttgart, 2020).

[13] J. C. Maxwell, *Philos. Trans. Roy. Soc. London* **155**, 459 (1865).

[14] M. Dressel and G. Grüner, *Electrodynamics of Solids: Optical Properties of Electrons in Matter* (Cambridge University Press, 2011).

[15] J. Bardeen, L. N. Cooper, and J. R. Schrieffer, *Phys. Rev.* **108**, 1175 (1957).

[16] F. London and H. London, *Proc. Roy. Soc. A* **149**, 71 (1935).

[17] J. E. Hirsch, *Phys. Rev. B* **69**, 214515 (2004).

[18] P. Mangin and R. Kahn, *Superconductivity* (Springer, 2017).

[19] V. Engl, *Master thesis: Planar microwave resonators on SrTiO3 substrates* (University of Stuttgart, 2019).

[20] D. M. Pozar, *Microwave Engineering* (John Wiley & Sons, Inc., 2011).

[21] R. E. Collin, *Foundations for microwave engineering* (John Wiley & Sons, 2000).

[22] W. Mathis and A. Reibiger, *Küpfmüller Theoretische Elektrotechnik* (Springer Vieweg, 2017).

[23] M. Thiemann, *Doctor thesis: Microwave investigations on superconducting Nb-doped SrTiO3* (University of Stuttgart, 2018).

[24] K. Nikolaou, *Bachelor thesis: Characteristics and coupling of superconducting multi-mode microwave resonators* (University of Stuttgart, 2020).

[25] M. Houdart, *1976 6th European Microwave Conference*, 49 (1976).

[26] R. E. Collin, *Field theory of guided waves* (John Wiley & Sons, 1991).

[27] L. Chang-Hong, *Notes on the Ellipsoidal Function* (Springer, 2017).

[28] C. Veyres and V. F. Hanna, *Int. J. Electron* **48**, 47 (1980).

[29] S. Gevorgian, L. Linner, and E. Kollberg, *IEEE Trans. Microw. Theory Tech.* **43**, 772 (1995).

[30] Y. Zhang, J. R. G. Evans, and S. Yang, *J. Chem. Eng. Data* **56**, 328 (2011).

[31] *Agilent Technologies: PNA Network Analyzer E8364C.*

[32] N. W. Ashcroft and N. D. Mermin, *Solid state physics* (Brooks/Coole Cengage Learning, 2010).

[33] E. S. Sabisky and H. J. Gerritsen, *J. Appl. Phys.* **33**, 1450 (1962).

[34] R. G. Geyer, B. Riddle, J. Krupka, and L. A. Boatner, *J. Appl. Phys.* **97**, 104111 (2005).

[35] R. A. Parker, *Phys. Rev.* **124**, 1719 (1961).

[36] L. Wendel, *Master thesis: Dielectric measurements at GHz frequencies* (University of Stuttgart, 2019).

[37] H. Wheeler, *Proc. IRE* **30**, 412 (1942).

[38] D. Hafner, M. Dressel, and M. Scheffler, *Rev. Sci. Instrum.* **85**, 014702 (2014).

[39] M. S. DiIorio, A. C. Anderson, and B. Y. Tsaur, *Phys. Rev. B* **38**, 7019 (1988).

[40] D. E. Oates, A. C. Anderson, C. C. Chin, J. S. Derov, G. Dresselhaus, and M. S. Dresselhaus, *Phys. Rev. B* **43**, 7655 (1991).

[41] L. K. Keys and L. N. Mulay, *Phys. Rev.* **154**, 453 (1967).

[42] S. Kwon, A. Fadavi Roudsari, O. W. B. Benningshof, Y.-C. Tang, H. R. Mohebbi, I. A. J. Taminiau, D. Langenberg, S. Lee, G. Nichols, D. G. Cory, and G.-X. Miao, *J. Appl. Phys.* **124**, 033903 (2018).

[43] D. Bothner, T. Gaber, M. Kemmler, D. Koelle, R. Kleiner, S. Wünsch, and M. Siegel, *Phys. Rev. B* **86**, 014517 (2012).

[44] H. Haken and H. C. Wolf, *Atom- und Quantenphysik* (Springer-Verlag Berlin Heidelberg, 2004).

[45] N. Yordanov, *Appl. Magn. Reson.* **6**, 241 (1994).

[46] M. J. Rahim, T. Lehleiter, D. Bothner, C. Krellner, D. Koelle, R. Kleiner, M. Dressel, and M. Scheffler, *J. Phys. D* **49**, 395501 (2016).

[47] B. Miksch, M. Dressel, and M. Scheffler, *Rev. Sci. Instrum.* **91**, 025106 (2020).

[48] C. C. Chin, D. E. Oates, G. Dresselhaus, and M. S. Dresselhaus, *Phys. Rev. B* **45**, 4788 (1992).

[49] J. Halbritter, *J. Appl. Phys.* **68**, 6315 (1990).

[50] B. Abdo, E. Segev, O. Shtempluck, and E. Buks, *Phys. Rev. B* **73**, 134513 (2006).

[51] M. A. Golosovsky, H. J. Snortland, and M. R. Beasley, *Phys. Rev. B* **51**, 6462 (1995).

[52] I. Kovacic, *Nonlinear Oscillations: Exact Solutions and their Approximations*, Englisch, 1 Online-Ressource(X, 273 p. 123 illus., 105 illus. in color.), Cham, 2020.

[53] G. E. Ponchak, J. Papapolymerou, and M. M. Tentzeris, *IEEE Trans. Microw. Theory Tech.* **53**, 713 (2005).

[54] Z. Chen, A. Megrant, J. Kelly, R. Barends, J. Bochmann, Y. Chen, B. Chiaro, A. Dunsworth, E. Jeffrey, J. Y. Mutus, P. J. J. O'Malley, C. Neill, P. Roushan, D. Sank, A. Vainsencher, J. Wenner, T. C. White, A. N. Cleland, and J. M. Martinis, *Appl. Phys. Lett.* **104**, 052602 (2014).